ISSN 0021-3438 (Print)
ISSN 2412-8783 (Online)

IZVESTIYA

NON-FERROUS METALLURGY

Vol. 31, No. 4, 2025

Scientific and Technical Journal
Founded in 1958
4 Issues per year

ИЗВЕСТИЯ ВУЗОВ

ЦВЕТНАЯ МЕТАЛЛУРГИЯ

Том 31, № 4, 2025

Научно-технический журнал
Основан в 1958 г.
Выходит 4 раза в год

ISSN 0021-3438 (Print)
ISSN 2412-8783 (Online)

IZVESTIYA NON-FERROUS METALLURGY

Vol. 31, No. 4
2025

Scientific and Technical Journal Founded in 1958 4 Issues per year http://cvmet.misis.ru

Journal is included into the List of the peer-reviewed scientific publications recommended by the Highest Attestation Commission of the Ministry of Education and Science of the Russian Federation for publishing the results of doctoral and candidate dissertations

Abstracting/Indexing: Russian Science Citation Index (RSCI), Chemical Abstracts (Online), INIS, OCLC ArticleFirst, Ulrich's Periodicals Directory, VINITI Database (Abstract Journal)

Founder

National University of Science and Technology "MISIS"
Address: 1 Bld, 4 Leninskiy Prosp., Moscow 119049, Russia
http://www.misis.ru

Editorial Staff

Address: NUST MISIS, 1 Bld, 4 Leninskiy Prosp., Moscow 119049, Russia
Phone: +7 (495) 638-45-35
E-mail: izv.vuz@misis.ru

Certificate of registration No. 015842 (13.03.1997)
Re-registration PI No. ФС77-79229 (25.09.2020)

Subscription: Ural-Press Agency

Leading Editor – A.A. Kudinova
Executive Editor – O.V. Sosnina
Layout Designer – E.A. Legkaya

Signed print 22.12.2025. Format 60×90 1/8.
Offset paper No. 1. Digital printing. Quires 9,5
Order 23808. Free price

Printed in the printing house of the MISIS Publish House
1 Bld, 4 Leninskiy Prosp., Moscow 119049, Russia. Phone/fax: +7 (499) 236-76-17

ISSN 0021-3438 (Print)
ISSN 2412-8783 (Online)

ИЗВЕСТИЯ ВУЗОВ
ЦВЕТНАЯ МЕТАЛЛУРГИЯ

Том 31, № 4
2025

Научно-технический журнал Основан в 1958 г. Выходит 4 раза в год http://cvmet.misis.ru

Журнал включен в Перечень рецензируемых научных изданий, рекомендованных ВАК Минобрнауки РФ для публикации результатов диссертаций на соискание ученых степеней

Журнал включен в базы данных: Russian Science Citation Index (RSCI), Chemical Abstracts (Online), INIS, OCLC ArticleFirst, Ulrich's Periodicals Directory, РИНЦ, БД/РЖ ВИНИТИ

Учредитель

ФГАОУ ВО Национальный исследовательский технологический университет «МИСИС»
Адрес: 119049, г. Москва, Ленинский пр-т, 4, стр. 1
http://www.misis.ru

Редакция журнала

Адрес: 119049, г. Москва, Ленинский пр-т, 4, стр. 1, НИТУ МИСИС
Тел.: +7 (495) 638-45-35
E-mail: izv.vuz@misis.ru

Свидетельство о регистрации № 015842 от 13.03.1997 г.
Перерегистрация ПИ № ФС77-79229 от 25.09.2020 г.

Подписка: Агентство «Урал-пресс»

Ведущий редактор – А.А. Кудинова
Выпускающий редактор – О.В. Соснина
Дизайн и верстка – Е.А. Легкая

Подписано в печать 22.12.2025. Формат 60×90 1/8.
Бум. офсетная № 1. Печать цифровая. Усл. печ. л. 9,5
Заказ 23808. Цена свободная

Отпечатано в типографии Издательского Дома МИСИС
119049, г. Москва, Ленинский пр-т, 4, стр. 1. Тел./факс: +7 (499) 236-76-17

CONTENTS

СОДЕРЖАНИЕ

Mineral Processing of NonFerrous Metals

Обогащение руд цветных металлов

Metallurgy of NonFerrous Metals

Металлургия цветных металлов

Pressure Treatment of Metals

Обработка металлов давлением

Physical Metallurgy and Heat Treatment

Металловедение и термическая обработка

UDC 622.765
https://doi.org/10.17073/0021-3438-2025-4-5-17

Research article
Научная статья

Effect of metal-containing modifier compositions with sodium sulfide on the selective flotation of copper and zinc sulfides

Htet Zaw Oo, Kyaw Zay Ya, B.E. Goryachev

National University of Science and Technology "MISIS"
1 Bld, 4 Leninskiy Prosp., Moscow 119049, Russia

✉ Htet Zaw Oo (htetzawoo68099@gmail.com)

Abstract: The most efficient selective reagent modes for the flotation of a copper–zinc pyrite ore from one of the Ural deposits have been developed, based on the use of compositions of metal-containing reagent modifiers in combination with sodium sulfide. The study analyzed the most effective conditions for separating copper and zinc minerals from pyrite during the bulk flotation of copper–zinc ore, as well as the conditions for improving the selective separation of the bulk copper–zinc concentrate. The influence of reagent–modifier compositions introduced into the bulk flotation cycle on the process parameters of selective flotation of the bulk concentrate was evaluated. The results of fractional analysis of the floatability of copper, zinc, and iron minerals were presented, taking into account the flotation kinetics and the distribution of these minerals in the floated concentrate by fractions: poorly floatable, moderately floatable, and easily floatable. The reagent–modifier compositions used not only depressed pyrite flotation but also ensured efficient separation of copper and zinc minerals into individual concentrates. It was found that the most effective selectivity in flotation separation of copper and zinc minerals was achieved by introducing a composition of ferrous sulfate and sodium sulfide into the bulk copper–zinc flotation circuit in equal proportions (50 and 50 g/t). As a result, a copper–pyrite concentrate containing 12 wt. % Cu with a copper recovery of 74.45 % and a zinc concentrate containing 5 wt. % Zn with a zinc recovery of 73.68 % from the ore were obtained. Analysis of flotation kinetics showed that the introduction of this reagent mixture contributed to the highest flotation rate of copper, ensuring a maximum copper recovery to the froth (copper–pyrite) product of 86.74 %.

Key words: copper-zinc ores, recovery, flotation, sodium sulfide, flotation kinetics, separation, selectivity, modifiers, sulfides.

For citation: Htet Zaw Oo, Kyaw Zay Ya, Goryachev B.E. Effect of metal-containing modifier compositions with sodium sulfide on the selective flotation of copper and zinc sulfides. *Izvestiya. Non-Ferrous Metallurgy.* 2025;31(4):5–17.
https://doi.org/10.17073/0021-3438-2025-4-5-17

Оценка влияния композиции металлосодержащих модификаторов с сернистым натрием на селективность флотационного разделения сульфидов меди и цинка

Хтет Зо У, Чжо Зай Яа, Б.Е. Горячев

Национальный исследовательский технологический университет «МИСИС»
Россия, 119049, г. Москва, Ленинский пр-т, 4, стр. 1

✉ Хтет Зо У (htetzawoo68099@gmail.com)

Аннотация: Разработаны наилучшие селективные реагентные режимы для флотации медно-цинковой колчеданной руды одного из месторождений Урала, основанные на применении композиций металлосодержащих реагентов-модификаторов в сочетании с сернистым натрием. Проанализированы наиболее эффективные условия флотации минералов меди и цинка от пирита в коллективном цикле флотации медно-цинковой руды, а также условия для повышения селективного разделения коллективного медно-цинкового концентрата. Оценено влияние композиций реагентов-модификаторов, вводимых в коллективный цикл флотации, на технологические показатели селективной флотации коллективного концентрата. Приведены результаты фракционного анализа флотируемости минералов меди, цинка и железа с учетом кинетики флотации и распределения этих минералов во флотируемый концентрат по фракциям: труднофлотируемой, среднефлотируемой и легкофлотируемой. Используемые композиции реагентов-модификаторов не только подавляли флотацию пирита, но и обеспечивали эффективное разделение минералов меди и цинка в отдельные концентраты. Установлено, что наиболее эффективное влияние на селективность флотационного разделения минералов меди и цинка оказывает дозирование композиции железного купороса и сульфида натрия в коллективную медно-цинковую флотацию в равных долях (50 и 50 г/т). В результате применения данной композиции реагентов получены медно-пиритный концентрат с содержанием меди 12 % при извлечении меди 74,45 % и цинковый концентрат с содержанием цинка 5 % при извлечении 73,68 % от руды. Анализ кинетики флотации показал, что введение указанной смеси реагентов способствует наилучшей скорости флотации меди, обеспечивая максимальное извлечение меди в пенный (медно-пиритный) продукт на уровне 86,74 %.

Ключевые слова: медно-цинковые руды, извлечение, флотация, сернистый натрий, кинетика флотации, разделение, селективность, модификаторы, сульфиды.

Для цитирования: Хтет Зо У, Чжо Зай Яа, Горячев Б.Е. Оценка влияния композиции металлосодержащих модификаторов с сернистым натрием на селективность флотационного разделения сульфидов меди и цинка. *Известия вузов. Цветная металлургия*. 2025;31(4):5–17. https://doi.org/10.17073/0021-3438-2025-4-5-17

Introduction

Copper—zinc pyrite ores from the Ural deposits are predominantly pyrite-type and rank among the most challenging to process [1]. This is due to the high pyrite content (85—90 wt. %) and fine, irregular intergrowth of sulfide minerals with each other and with gangue minerals [2; 3].

Flotation is the most efficient process for separating minerals from finely disseminated non-ferrous metal ores such as copper—zinc pyrite ores [4—7]. The processing of large volumes of refractory raw materials requires the development and implementation of new methods and technologies [8]. The use of selective reagent modes and optimization of pulp conditioning can increase the contrast of surface properties of minerals with similar technological characteristics [9].

At present, the most common scheme at concentrator plants is the bulk—selective flotation circuit, in which copper and zinc minerals are recovered from the bulk copper—zinc concentrate while pyrite flotation is suppressed [10; 11]. This technology enables high-quality recovery of metals from finely disseminated and refractory ores, followed by the production of concentrates for various applications, and significantly enhances the selectivity of mineral separation [12; 13].

Despite significant advances in the mineral processing industry, the selective flotation of non-ferrous metal sulfide ores — particularly copper—zinc pyrite ores — remains an urgent challenge [10]. It can be addressed by improving existing technologies through modifications to process flowcharts, optimizing reagent application modes and broadening the range of reagents used in the flotation circuit [10]. One of the key approaches to improving the efficiency of processing copper—zinc ores is the development of new reagent systems, including compositions of metal-containing reagent modifiers [14].

Previous studies [15—17] have demonstrated the positive effect of metal-containing reagent—modifier compositions on the results of bulk flotation of copper—zinc ore. However, their role in the selective flotation of bulk copper—zinc concentrate has not been investigated. The aim of this study is to examine the effect of metal-containing modifier compositions combined with sodium sulfide, introduced into the bulk flotation circuit, on the efficiency of selective flotation of this concentrate.

Materials and methods

Research objects

Samples of copper—zinc pyrite ore from a Ural deposit were used as the test material. The average contents of copper, zinc, and iron in the run-of-mine ore were 0.65 ± 0.02, 1.30 ± 0.08 и 38.48 ± 1.52 wt. %, respectively [15]. The following reagents were used in the experiments: potassium butyl xanthate (PBX) as

Table 1. **Quantitative *X*-ray diffraction (XRD) phase analysis of the raw ore (powder)**

Таблица 1. Рентгенографический фазовый анализ исходной руды (порошка)

Mineral	Ideal formula	Content, wt. %
Pyrite	FeS_2	61
Chalcopyrite	$CuFeS_2$	3
Sphalerite	ZnS	5
Tetrahedrite	$(Cu,Fe,Zn,Ag)_{24}(Sb,As)_8S_{26}$	0.5
Quartz	SiO_2	21
Calcite	$Ca(CO_3)$	3
Barite	$BaSO_4$	2
Chlorite	$(Mg,Fe)_{4.75}Al_{1.25}(Si_{2.75}Al_{+.25}O_{10})(OH)_8$	2
Illite	$KAl_2(AlSi_3O_{10})\cdot(OH)_2$	1
	Σ	**98.5**

Table 2. **Mineralogical analysis of the raw ore (polished section)**

Таблица 2. Минералогический анализ исходной руды (полированный шлиф)

Mineral	Mineral content in analyzed samples, wt. %										Mean	Confidence interval
	1	*2*	*3*	*4*	*5*	*6*	*7*	*8*	*9*	*10*		
Pyrite	84	75	91	77	92	75	74	73	81	96	81.80	±5.27
Quartz	15	20	6	16	5	22	20	23	14.5	2	14.35	±4.67
Sphalerite	–	–	–	3	–	–	–	2.5	–	–	2.75	±0.72
Chalcopyrite	–	–	1.5	0.5	1.5	1.5	3	1	2	1	1.50	±0.57
Fahlore	–	–	–	–	1	–	1.5	–	1.5	0.5	1.13	±0.40
Carbonate	–	3	1	2	–	–	1.5	–	1	0.5	1.50	±0.63
Others	1	2	0.5	1.5	0.5	1.5	–	0.5	–	–	1.07	±0.44

the collector, pine oil as the frother, lime (CaO) as the pH regulator, and the modifier reagents ferrous sulfate ($FeSO_4 \cdot 7H_2O$), copper sulfate ($CuSO_4 \cdot 5H_2O$), zinc sulfate ($ZnSO_4 \cdot 7H_2O$), and sodium sulfide ($Na_2S \cdot 9H_2O$).

Quantitative *X*-ray diffraction (XRD) and reflected-light ore microscopy of the raw ore sample were performed using a Tongda TD-3700 *X*-ray diffractometer and an Olympus BX51 optical microscope. The results are summarized in Tables 1 and 2.

Procedure for bulk flotation of copper–zinc ore

Ore preparation was carried out as follows: the initial ore was crushed in a jaw crusher (DSh 80×150) to a particle size of 3 mm. After averaging and quartering, 1 kg ore samples were taken from the crushed material. These samples were ground in a laboratory ball mill (MShL-7) to a fineness of 80 % passing –0.074 mm, after which the ground material was subjected to bulk flotation.

The flotation tests were conducted in mechanical flotation machines (Mekhanobr and FL-137) with cell volumes of 0.5 L and 3.0 L. Under laboratory conditions, flotation experiments were carried out according to a process flowsheet that included Flotation *I* (copper head flotation) and Flotation *II* (copper—zinc flotation) [15]. The flowsheet of the bulk flotation of copper—zinc ore and the production of the bulk copper—zinc concentrate is shown in Fig. 1.

In Flotation *I*, only the collector and frother were used, and the flotation process was carried out for 2 min. The tailings from Flotation I served as the feed for Flotation *II*, in which lime, modifier reagents, potassium butyl xanthate, and pine oil were added [15]. The total consumption of modifier reagents in all tests was 100 g/t. Flotation *II* was then performed for 8 min. The concentrates obtained from Flotation *I* and Flotation *II* were combined to produce the bulk copper—zinc concentrate.

Procedure for selective flotation of the bulk concentrate

The process of selective flotation of the bulk copper—zinc concentrate included the following stages: desorption of the collector from the surface of sulfide minerals in a sodium sulfide medium to achieve strong depression of sphalerite; thickening and washing of the concentrate to remove excess alkalinity; regrinding of the coarse bulk copper—zinc concentrate to 92—95 % passing –0.044 mm; and primary copper—pyrite flotation [18]. The flowsheet of the selective flotation process for the bulk copper—zinc concentrate is shown in Fig. 2.

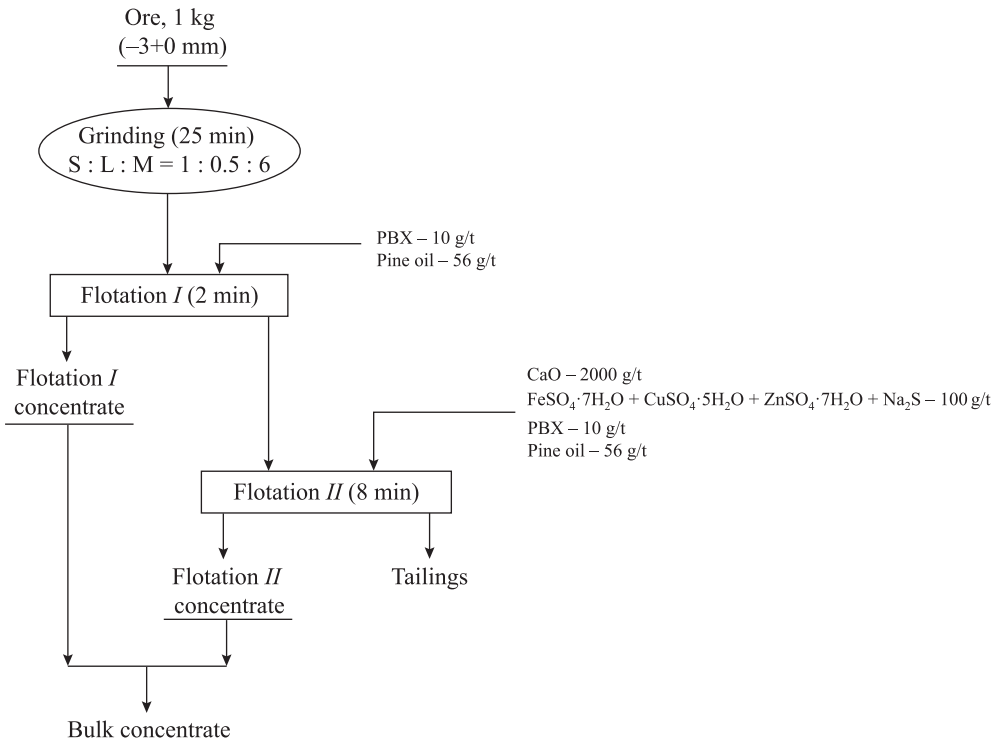

Fig. 1. Flowsheet for producing the bulk copper–zinc concentrate

Рис. 1. Схема получения коллективного медно-цинкового концентрата

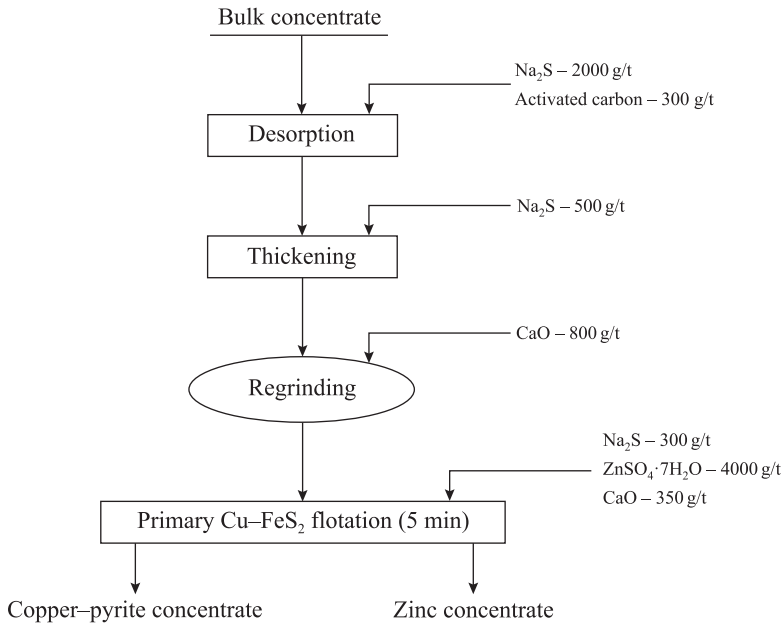

Fig. 2. Flowsheet of the selective flotation of the bulk copper–zinc concentrate

Рис. 2. Схема селекции коллективного медно-цинкового концентрата

According to the selective flotation flowsheet (Fig. 2), the bulk concentrate was first subjected to desorption using sodium sulfide (2000 g/t) and activated carbon (300 g/t). After desorption, the pulp was thickened to a solids content of 60 % with the addition of sodium sulfide (500 g/t) and reground to 95 % passing –0.044 mm with lime addition (800 g/t) [19]. The reground product was then subjected to primary copper—pyrite flotation.

In practice, separation of copper and zinc minerals is most often carried out using a scheme based on sphalerite depression [20—22]. In the primary copper—pyrite flotation process, sphalerite depression was achieved through the use of sodium sulfide (300 g/t) and zinc sulfate (4000 g/t). This operation was conducted under alkaline conditions maintained by the addition of lime (350 g/t), ensuring a pH of 8.5—9.0. Upon completion of the flotation tests, the products were dried, and the copper, zinc, and iron contents were analyzed using an ElvaX *X*-ray fluorescence spectrometer.

Results and discussion

Effect of reagent–modifier compositions on the efficiency of selective flotation of the bulk concentrate

The results of selective flotation of the bulk copper—zinc concentrate with the addition of reagent—modifier compositions in Flotation *II* are presented in Figs. 3 and 4.

According to the data in Fig. 3, the use of the studied reagent—modifier compositions in Flotation *II* has a significant effect on the process performance of the selective flotation of the bulk concentrate. The compositions of ferrous and copper sulfates ($0.5FeSO_4$ + + $0.5CuSO_4$) and ferrous sulfate with sodium sulfide ($0.5FeSO_4 + 0.5Na_2S$) provided the best results for copper recovery into the concentrate (Fig. 3, *a*). In the first case, the copper—pyrite concentrate contained 13 % Cu with a copper recovery of 69.87 %, and in the second — 12 % Cu with a recovery of 75.45 %. Compared with the baseline test without modifiers (in which the copper content was 11.32 % and the recovery was 55.72 %), the use of these reagent—modifier mixtures increased copper recovery by 14.15 % and 19.73 %, respectively.

Notably, when using the $0.5FeSO_4 + 0.5Na_2S$ mixture, copper loss with the scavenger product was the lowest, amounting to 11.54 %. Nevertheless, the highest copper content in the copper—pyrite concentrate (13.32 %) was achieved when introducing the $0.25CuSO_4 + 0.75Na_2S$ mixture into Flotation *II*, while the zinc content in this concentrate remained at 2.29 % (Fig. 3, *b*).

As shown in Fig. 4, a similar trend was observed in the zinc (scavenger) concentrate, where the selectivity of copper and zinc separation increased. It was established that introducing into Flotation *II* the mixtures of ferrous and zinc sulfates ($0.5FeSO_4$ + $0.5ZnSO_4$)

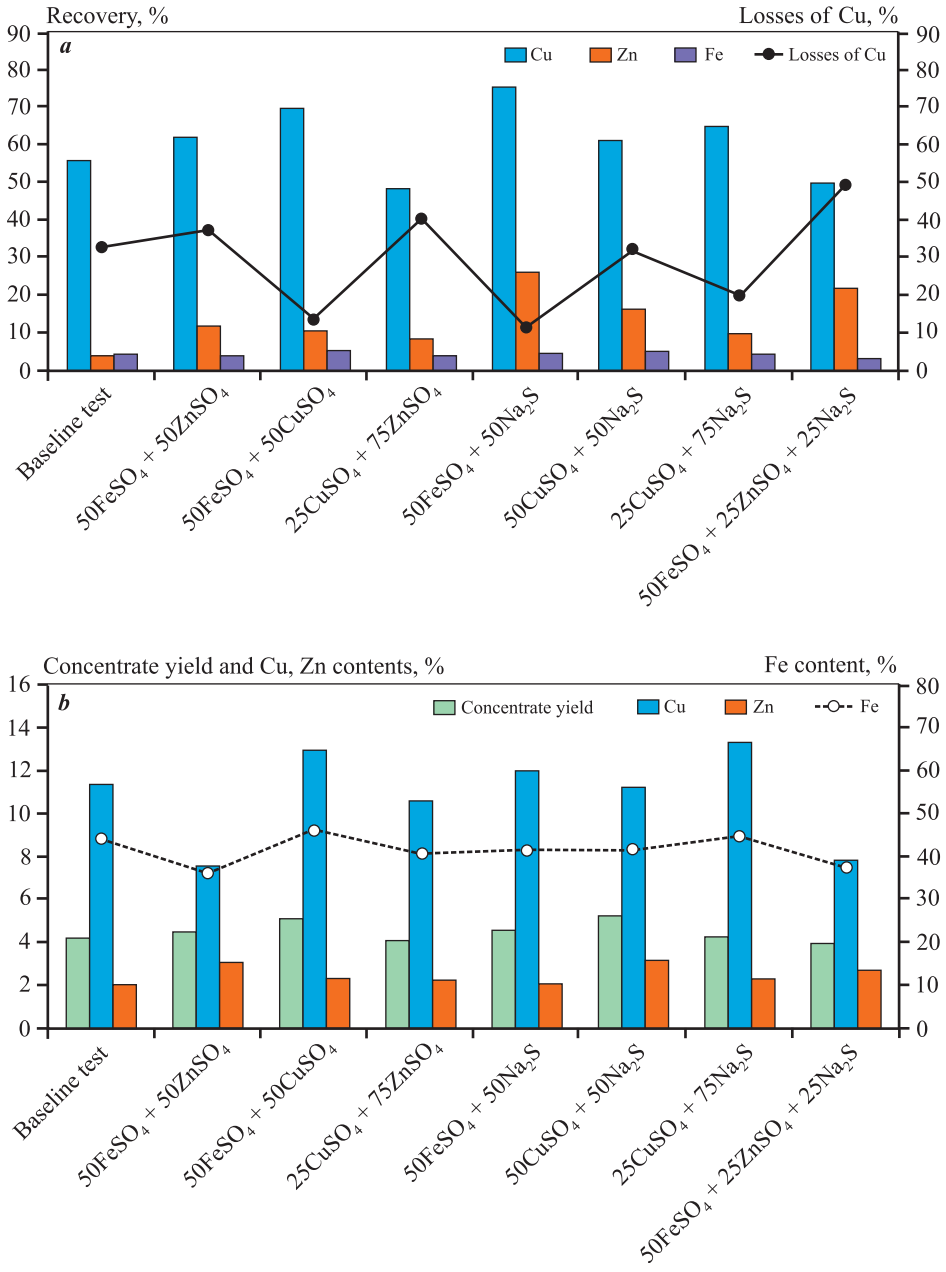

Fig. 3. Recovery of copper, zinc, and iron into the copper–pyrite concentrate and copper losses with the scavenger product (***a***), as well as the concentrate yield and copper, zinc, and iron contents (***b***) depending on the reagent–modifier compositions introduced into Flotation *II*

Рис. 3. *И*звлечение меди, цинка и железа в медно-пиритный концентрат и потери меди с камерным продуктом (***a***), а также выход концентрата и содержание меди, цинка и железа в нем (***b***) при расходе композиций модификаторов во флотацию *II*

and ferrous sulfate, zinc sulfate, and sodium sulfide ($0.5FeSO_4$ + $0.25ZnSO_4$ + $0.25Na_2S$) ensured the highest zinc recovery into the concentrate (Fig. 4, *a*): 78.86 % and 77.93 %, respectively. This corresponds to an increase in zinc recovery by 49.67 % and 48.71 % compared with the baseline mode without modifiers (29.19 %).

It is noteworthy that when using the mixture of ferrous and copper sulfates ($0.5FeSO_4$ + $0.5CuSO_4$), the obtained concentrate demonstrated the highest zinc content (Fig. 4, *b*): 8.3 % Zn, while the copper content remained at 1.72 %. This increased the zinc grade of the obtained zinc concentrate by 4.83 % compared with the baseline test without modifiers (3.47 %).

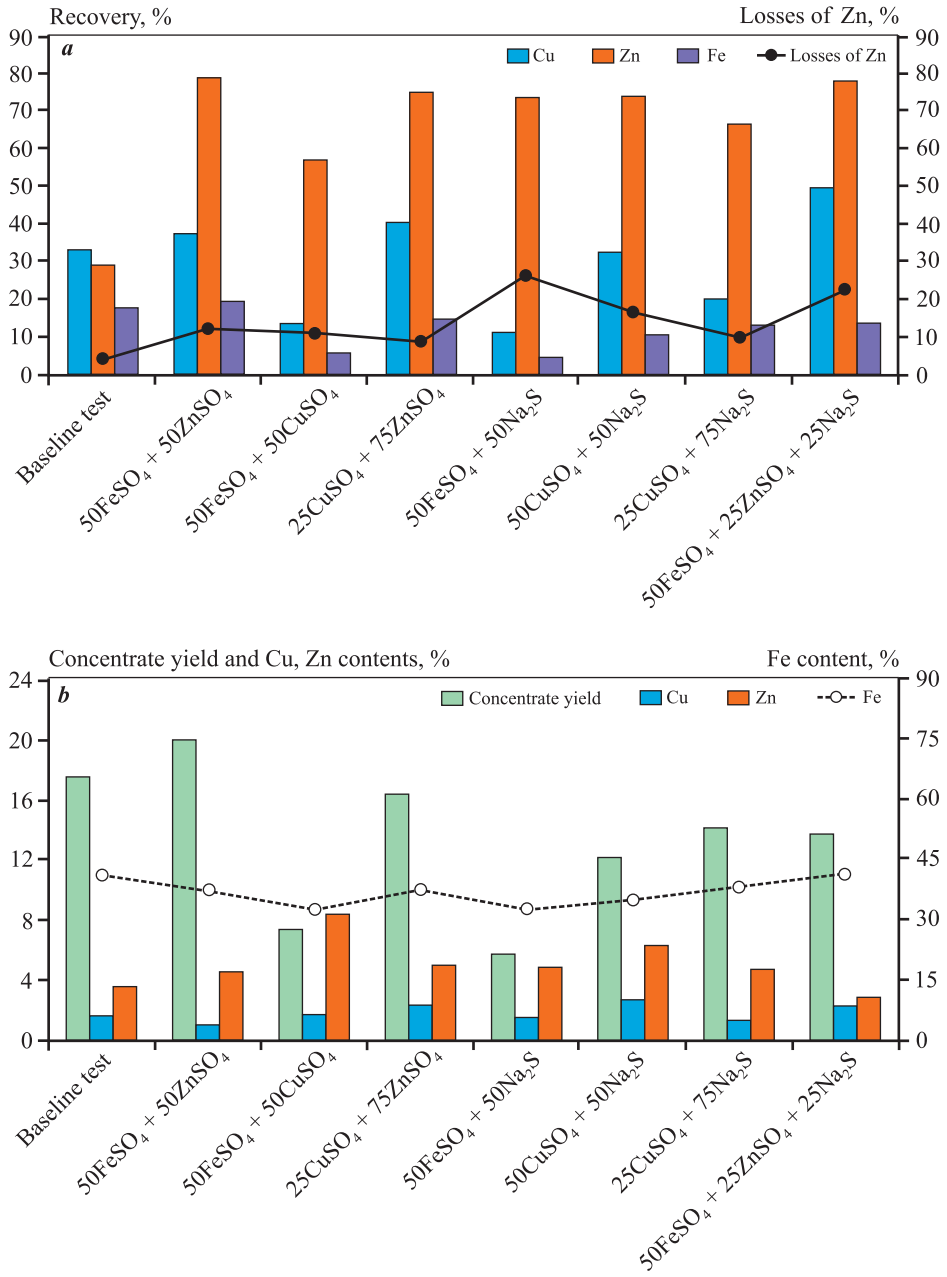

Fig. 4. Recovery of copper, zinc, and iron into the zinc concentrate and zinc losses with the froth product (***a***), as well as the concentrate yield and copper, zinc, and iron contents (***b***) depending on the reagent–modifier compositions introduced into Flotation *II*

Рис. 4. Извлечение меди, цинка и железа в цинковый концентрат и потери цинка с пенным продуктом (***a***), а также выход концентрата и содержание меди, цинка и железа в нем (***b***) при расходе композиций модификаторов во флотацию *II*

Kinetics of selective flotation of the bulk concentrate and fractional analysis of the floatability of copper, zinc, and iron minerals

The study of the kinetics of selective flotation of the bulk concentrate involved the fractional collection of the froth product at flotation time intervals of 0.21 min (corresponding to three scrapes of the froth layer), 0.43 min (six scrapes), 0.64 min (nine scrapes), 1, 2, and 5 min. During the investigation of the flotation kinetics of the bulk concentrate, the distribution of materials was analyzed according to fractions differing in the floatability of the respective minerals in the froth product of the main copper—pyrite flotation. Using the Spectr software developed by Prof. D.V. Shekhirev, the floatability

spectra of copper and zinc minerals in the concentrate were evaluated [15; 23; 24].

Fractional analysis of selective flotation involved partitioning the floated material into six fractions according to floatability, each defined by a specific range of flotation rate constants (K, min^{-1}) and described by the equation proposed by K.F. Beloglazov: 1st fraction, $0 < K < 0.0001$; 2nd, $0.0001 < K < 0.001$; 3rd, $0.001 < K < 0.01$; 4th, $0.1 < K < 1$; 5th, $1 < K < 10$; and 6th, $10 < K < 100$ [15; 25—28].

Fig. 5 presents the results of copper flotation kinetics into the copper—pyrite product when reagent—modifier compositions were introduced into Flotation *II*.

As seen in Fig. 5, *a*, the introduction of reagent—modifier compositions into Flotation *II* resulted in a substantial increase in the copper flotation rate compared with the baseline test without their use. The highest copper flotation rates were obtained with the reagent mixtures containing combinations of ferrous and copper sulfates ($0.5FeSO_4 + 0.5CuSO_4$) and ferrous sulfate with sodium sulfide ($0.5FeSO_4 + 0.5Na_2S$). At the early stages of flotation (0.21 min), copper recovery in these variants reached 32.39—32.98 %, which is more than seven times higher than that of the control test (4.3 %). After 2 min of flotation, copper recovery increased to 80.46 % in the presence of these reagents, while in the baseline test it was only 22.98 %. The maximum copper recovery into the froth product (86.74 %) was achieved using the $0.5FeSO_4 + 0.5Na_2S$ mixture at $\tau = 5$ min.

The results of fractional analysis (Fig. 5, *b*) showed that copper minerals were distributed among the 1st (poorly floatable), 3rd and 4th (moderately floatable), and 5th (easily floatable) fractions. In the control test, the proportions of poorly, moderately, and easily floatable fractions were 0.61, 0.35, and 0.04 rel. units, respectively. The most pronounced effect on the floatability of copper minerals was observed with the compositions $0.5FeSO_4 + 0.5CuSO_4$ and $0.5FeSO_4 + 0.5Na_2S$. In the first case, the proportion of poorly floatable fractions decreased to 0.098, moderately floatable to 0.301, while the easily floatable fraction increased to 0.601 rel. units. In the second case, the poorly floatable fraction decreased further to 0.009, the moderately floatable fraction increased to 0.481, and the easily floatable fraction reached 0.51 rel. units. Under these conditions, copper recovery into the copper—pyrite concentrate reached its maximum.

Fig. 6 shows the results of zinc flotation kinetics into the copper—pyrite product when reagent—modifier compositions were introduced into Flotation *II*.

The analysis of the data in Fig. 6, *a* indicates that the addition of reagent—modifier compositions to Flotation *II* caused a slight increase in the zinc flotation rate compared with the baseline test. The mixtures $0.5FeSO_4 + 0.5CuSO_4$ and $0.5FeSO_4 + 0.5Na_2S$ provided the highest zinc flotation rates, with zinc recoveries of 29.98 % and 26.32 % into the froth product after 5 min, exceeding the control value (12.59 %). The least influence on the zinc flotation rate was observed with the $0.5FeSO_4 + 0.5ZnSO_4$ mixture, giving only 15.46 % zinc recovery. Thus, despite the suppression of sphalerite

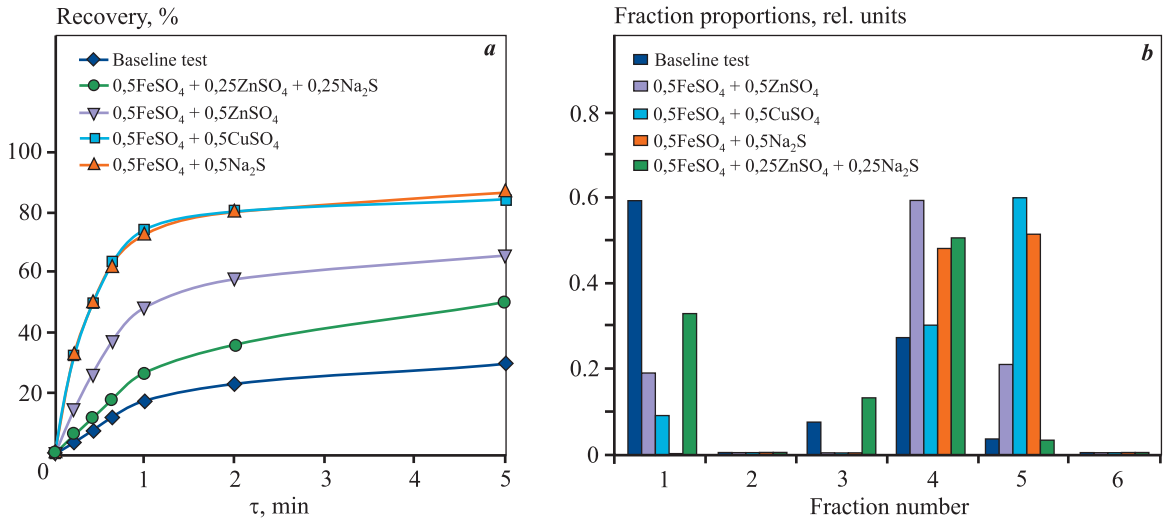

Fig. 5. Kinetics of copper flotation into the copper-pyrite product (***a***) and its distribution by fractions (***b***) upon addition of reagent–modifier compositions into Flotation *II*

Рис. 5. Кинетика флотации меди в медно-пиритный продукт (***a***) и ее распределение по фракциям (***b***) при дозировании композиций реагентов-модификаторов во флотацию *II*

flotation in the lime medium when sodium sulfide and zinc sulfate were used, these reagent—modifier mixtures slightly accelerated zinc flotation.

According to Fig. 6, *b*, zinc minerals were distributed among the 1st and 2nd (poorly floatable), 3rd and 4th (moderately floatable), and 5th (easily floatable) fractions. In the baseline test without modifiers, the proportions of poorly, moderately, and easily floatable fractions were 0.742, 0.257, and 0.001 rel. units, respectively. When the $0.5FeSO_4 + 0.5CuSO_4$ mixture was used, the easily floatable fraction amounted to only 0.012 rel. units. The introduction of $0.5FeSO_4 + 0.5Na_2S$ and $0.5FeSO_4 + 0.25ZnSO_4 + 0.25Na_2S$ mixtures into Flotation *II* considerably reduced the proportion of poorly floatable fractions to 0.42 and 0.38 rel. units, respectively. The proportion of moderately floatable fractions increased to 0.58 and 0.62 rel. units, while easily floatable fractions were entirely absent. This explains the influence of these reagent—modifier mixtures on the poorly floatable fractions of zinc minerals into the copper—pyrite concentrate.

Fig. 7 presents the results of iron flotation kinetics into the copper—pyrite product when reagent—modifier compositions were introduced into Flotation *II*.

The kinetic curves of iron flotation (Fig. 7, *a*) demonstrate a notable acceleration of the process upon addition of reagent—modifier compositions to Flotation *II* compared with the baseline test without them. The highest iron flotation rate was obtained with the $0.5FeSO_4 + 0.5Na_2S$ composition, yielding 50.88 % recovery after 5 min of flotation. A similar trend was observed with the $0.5FeSO_4 + 0.5CuSO_4$ mixture, where iron reco-

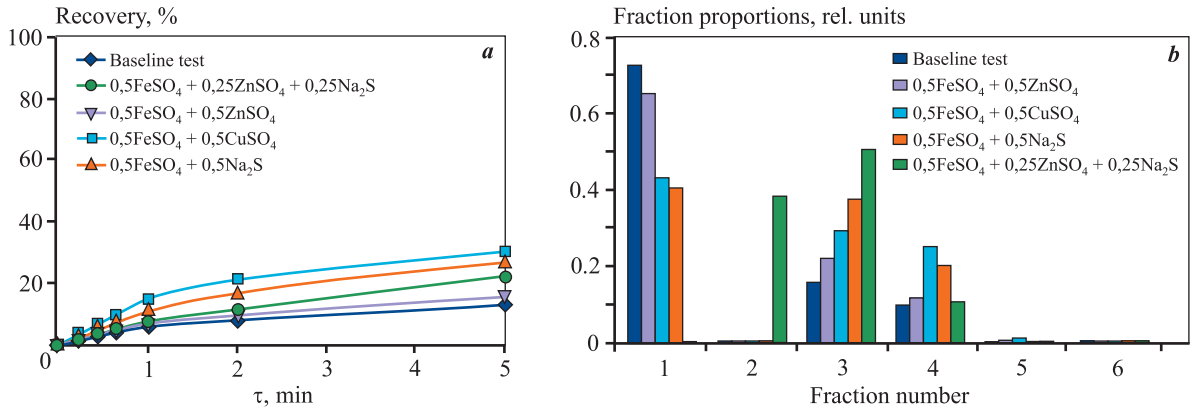

Fig. 6. Kinetics of zinc flotation into the copper-pyrite product (***a***) and its distribution by fractions (***b***) upon addition of reagent–modifier compositions into Flotation *II*

Рис. 6. Кинетика флотации цинка в медно-пиритный продукт (***a***) и его распределение по фракциям (***b***) при дозировании композиций реагентов-модификаторов во флотацию *II*

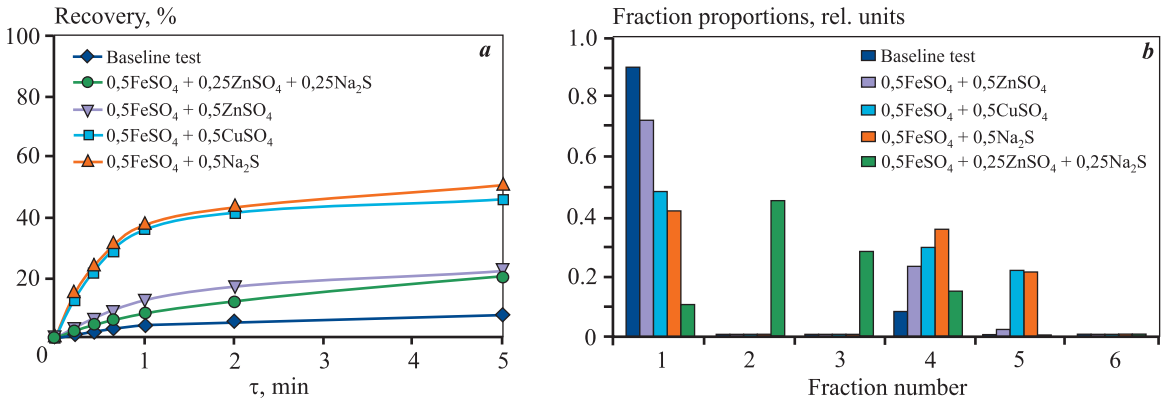

Fig. 7. Kinetics of iron flotation into the copper-pyrite product (***a***) and its distribution by fractions (***b***) when upon addition of reagent–modifier compositions into Flotation *II*

Рис. 7. Кинетика флотации железа в медно-пиритный продукт (***a***) и его распределение по фракциям (***b***) при добавлении композиций реагентов-модификаторов во флотацию *II*

very reached 46.06 % over the same period. The smallest increase in iron flotation rate was observed when using $0.5FeSO_4 + 0.5ZnSO_4$ and $0.5FeSO_4 + 0.25ZnSO_4 + 0.25Na_2S$.

From the data in Fig. 7, *b*, it can be seen that in all experimental variants the proportion of poorly floatable fractions was high, especially in the baseline test (0.912 rel. units). However, upon addition of $0.5FeSO_4 + 0.5Na_2S$ and $0.5FeSO_4 + 0.5CuSO_4$, this proportion decreased significantly to 0.428 and 0.48 rel. units, respectively. At the same time, the proportion of easily floatable fractions was the highest, reaching 0.221 and 0.211 rel. units. The most pronounced transfer of iron minerals into the moderately floatable fractions (3 and 4) was observed when the $0.5FeSO_4 + 0.5Na_2S$ composition was used, whereas with $0.5FeSO_4 + 0.5ZnSO_4$, the share of these fractions increased, but a high proportion of poorly floatable ones remained.

Thus, the analysis of selective flotation kinetics demonstrated that the introduction of reagent—modifier compositions into Flotation *II* allows for evaluating the floatability of copper, zinc, and iron minerals into the froth (copper—pyrite) product, which is critical for improving process selectivity. In this case, copper minerals are mainly represented by moderately and easily floatable fractions, sphalerite by poorly and moderately floatable fractions, and pyrite by poorly, moderately, and partially easily floatable fractions.

Conclusions

1. A selective reagent mode was developed for the bulk—selective flotation of a copper—zinc pyrite ore from a Ural deposit, based on applying compositions of metal-containing reagent modifiers with sodium sulfide in the bulk flotation circuit.

2. Analysis of the flotation results for the copper—zinc pyrite ore identified an optimal combination of modifier reagents — ferrous sulfate, copper sulfate, and zinc sulfate with sodium sulfide — which not only reduced pyrite recovery to the bulk concentrate but also increased the selectivity of separating copper and zinc minerals into individual concentrates.

3. Based on the flotation tests, among the reagent—modifier compositions studied, the combination of ferrous sulfate and sodium sulfide in an equal ratio ($0.5FeSO_4 + 0.5Na_2S$) markedly enhanced the selectivity of separating copper and zinc minerals, increasing copper recovery to the froth (copper—pyrite) product while minimizing losses to the scavenger (zinc) product.

4. Using the proposed reagent composition yielded a copper—pyrite concentrate assaying 12 % Cu at a copper recovery of 75.45 %, as well as a zinc concentrate assaying 4.76 % Zn at a zinc recovery of 73.68 %. The mixture $0.5FeSO_4 + 0.5CuSO_4$ also produced positive selective-flotation results; however, copper recovery in this case was lower than with the former reagent mixture.

5. Kinetic analysis showed that introducing the $0.5FeSO_4 + 0.5Na_2S$ mixture in Flotation *II* had a pronounced effect on the copper flotation rate, ensuring a maximum copper recovery of 86.74 % to the froth product. Under these conditions, the share of poorly floatable fractions decreased to 0.009 rel. units, the moderately floatable fractions increased to 0.481, and the easily floatable fractions rose to 0.51. Sphalerite was virtually absent from the easily floatable fractions when this modifier composition was used.

6. The studies on the effect of sodium-sulfide-containing reagent—modifier compositions applied in the bulk flotation circuit of copper—zinc ores on the selectivity of copper and zinc sulfide separation support the feasibility of using an equal-dose mixture of ferrous sulfate and sodium sulfide (50 g/t + 50 g/t) in analogous flotation processes at concentrators treating copper—zinc pyrite ores from the same deposit.

References

1. Chanturia V.A., Shadrunova I.V. Technology of enrichment of copper and copper-zinc ores of the Urals. Moscow: Nauka, 2016, 386 p. (In Russ.)
Чантурия В.А., Шадрунова И.В. Технология обогащения медных и медно-цинковых руд Урала. М.: Наука, 2016, 386 с.
2. Kyaw Z.Y., Tiagalieva Z.A., Htet Z.O., Phyo K.K. Improvement of reagent flotation modes of sphalerite and pyrite from deposits of copper-zinc pyrite, polymetallic copper-zinc pyrite and polymetallic ores. *IOP Conference Series: Earth and Environmental Science. XXI Conference of PhD Students and Young Scientists (CPSYS 2021)* (Wroclaw, Poland, 23—25 June 2021). 2021;942(1):1—8.
http://dx.doi.org/10.1088/1755-1315/942/1/012004
3. Herrera-Urbina R., Hanson J.S., Harris G.H., Fuerstenau D.W. Principles and practice of sulphide mineral flotation. In: P.M.J. Gray, G.J. Bowyer, J.F. Castle, D.J. Vaughan, N.A. Warner (Eds.). *Sulphide deposits — their origin and processing.* Dordrech: Springer, 1990. P. 87—101.
https://doi.org/10.1007/978-94-009-0809-3_6
4. Ndoro T.O., Witika L.K. A review of the flotation of copper minerals. *International Journal of Sciences: Basic and Applied Research (IJSBAR).* 2017;34(2):145—165.
https://www.gssrr.org/index.php/JournalOfBasicAndApplied/article/view/7590

5. Chandra A.P., Gerson A.R. A review of the fundamental studies of the copper activation mechanisms for selective flotation ofthe sulfide minerals, sphalerite and pyrite. *Advances in Colloid and Interface Science*. 2009;145(1-2): 97—110. http://dx.doi.org/10.1016/j.cis.2008.09.001
6. Yang B., Tong X., Lan Z., Cui Y., Xie X. Influence of the interaction between sphalerite and pyrite on the copper activation of sphalerite. *Minerals*. 2018;8(1):16. http://dx.doi.org/10.3390/min8010016
7. Bocharov V.A., Ryskin M.Ya., Pospelov N.D. Development of technology for processing copper-zinc ores of the Urals. *Tsvetnye Metally*. 1979;(10):105—107. (In Russ.). https://doi.org/10.17580/tsm.2018.04.03
Бочаров В.А., Рыскин М.Я., Поспелов Н.Д. Развитие технологии переработки медно-цинковых руд Урала. *Цветные металлы*. 1979;(10):105—107. https://doi.org/10.17580/tsm.2018.04.03
8. Bocharov V., Ignatkina V., Kayumov A., Viduetsky M., Maltsev V. Complex processing of refractory pyrite copper, copper-zinc and polymetallic ores on the basis of flotation and combined technologies. *Progress in Materials Science and Engineering*. 2018;(12):89—96. http://dx.doi.org/10.1007/978-3-319-75340-9_12
9. Мамонов S.V., Dresvyankina T.P., Ziyatdinov S.V., Ershov A.A. Technological solutions for processing copper and copper-zinc ores of the pyrite deposit of the Urals. *Globus: geology and business*. 2020;(3):140—144. (In Russ.). https://www.vnedra.ru/globus/zhurnal-globus-62/
Мамонов С.В., Дресвянкина Т.П., Зиятдинов С.В., Ершов А.А. Технологические решения переработки медных и медно-цинковых руд колчеданного месторождения Урала. *Глобус: геология и бизнес*. 2020;(3):140—144. https://www.vnedra.ru/globus/zhurnal-globus-62/
10. Zavarukhina E.A., Orekhova N.N. Effects of additional collecting agent on selectivity of flotation of copper and zinc sulfide. *Gornyi informatsionno-analiticheskii byulleten*. 2017;(3):305—311. (In Russ.). https://giab-online.ru/catalog/11943
Заварухина Е.А., Орехова Н.Н. Влияние дополнительного собирателя на селективность флотационного разделения сульфидов меди и цинка. *Горный информационно-аналитический бюллетень*. 2017;(3):305—311. https://giab-online.ru/catalog/11943
11. Zhao Cao, Xumeng Chen, Yongjun Peng. The role of sodium sulfide in the flotation of pyrite depressed in chalcopyrite flotation. *Minerals Engineering*. 2018;119: 93—98. http://dx.doi.org/10.1016/j.mineng.2018.01.029
12. Yufan Mu, Yongjun Peng, Lauten R.A. The depression of pyrite in selective flotation by different reagent systems — A literature review. *Minerals Engineering*. 2016;(96): 143—156. http://dx.doi.org/10.1016/j.mineng.2016.06.018
13. Aikawa K., Ito M., Orii N., Jeon S., Park I., Haga K., Kamiya T., Takahashi T., Sunada K., Sakakibara T., Ono T., Magwaneng R.S., Hiroyoshi N. Flotation of copper ores with high Cu/Zn ratio: Effects of pyrite on Cu/Zn separation and an efficient method to enhance sphalerite depression. *Minerals*. 2022;12(9):1103. http://dx.doi.org/10.3390/min12091103
14. Goryachev B.E., Naing Lin Oo, Nikolaev A.A., Polyakova Yu.N. Features of the influence of copper, zinc, and iron cations on the flotation capacity of pyrite from one of the copper-zinc deposits in the Urals. *Tsvetnye Metally*. 2015;(1):12—18. (In Russ.). https://www.rudmet.ru/journal/1381/article/23748/
Горячев Б.Е., Наинг Лин У, Николаев А.А., Полякова Ю.Н. Особенности влияния катионов меди, цинка и железа на флотируемость пирита одного из медно-цинковых месторождений Урала. *Цветные металлы*. 2015;(1):12—18. https://www.rudmet.ru/journal/1381/article/23748/
15. Htet Zaw Oo, Kyaw Zay Ya, Goryachev B.E. Effect of iron, zinc sulfate and sodium sulfide compositions on flotation of copper-zinc pyrite ores. *Gornyi informatsionno-analiticheskii byulleten*. 2023;(12):139—151. (In Russ.). https://giab-online.ru/files/Data/2023/12/12_2023_139-151.pdf
Хтет Зо У, Чжо Зай Яа, Горячев Б.Е. Действие композиций из железного, цинкового купоросов и сернистого натрия на флотацию медно-цинковых колчеданных руд. *Горный информационно-аналитический бюллетень*. 2023;(12):139—151. https://giab-online.ru/files/Data/2023/12/12_2023_139-151.pdf
16. Htet Zaw Oo, Kyaw Zay Ya, Goryachev B.E. Role of simplex experimental planning in enhancing the prediction and optimization of multicomponent system compositions of reagent-modifiers in the flotation of copper-zinc ores. *Problems of subsurface use*. 2024;(3):87—98. (In Russ.). https://trud.igduran.ru/index.php/psu/article/view/642
Хтет Зо У, Чжо Зай Яа, Горячев Б.Е. Роль симплексного планирования эксперимента в совершенствовании прогнозирования и оптимизации составов многокомпонентных систем реагентов-модификаторов при флотации медно-цинковых руд. *Проблемы недропользования*. 2024;(3):87—98. https://trud.igduran.ru/index.php/psu/article/view/642
17. Htet Zaw Oo, Kyaw Zay Ya, Goryachev B. E. Modeling and optimization of compositions of three-component modifier mixtures by simplex planning method to analyze their effect on the flotation of copper-zinc pyrite ores. *Gornyi informatsionno-analiticheskii byulleten*. 2024;(8):141—152. (In Russ.). https://giab-online.ru/files/Data/2024/8/08_2024_141-152.pdf

Хтет Зо У, Чжо Зай Яа, Горячев Б.Е. Моделирование и оптимизация составов трехкомпонентных смесей модификаторов методом симплексного планирования для анализа их влияния на флотацию медно-цинковых колчеданных руд. *Горный информационно-аналитический бюллетень*. 2024;(8):141—152. https://giab-online.ru/files/Data/2024/8/08_2024_141-152.pdf

18. Bocharov V.A., Agafonova G.S., Khersonskaya I.I., Lapshina G.A., Khersonskii M.I., Kas'yanova E.F., Serebryannikov B.L., Ivanov N.F., Morozov B.A., Karbovskaya A.V. Method of flotation separation of sulfide copper-zinc-pyritic concentrates, that have zinc sulfides activated by copper and calcium cations: Patent 2054971 (RF). 1996. (In Russ.).
https://www.elibrary.ru/item.asp?id=38031592
Бочаров В.А., Агафонова Г.С., Херсонская И.И., Лапшина Г.А., Херсонский М.И., Касьянова Е.Ф., Серебрянников Б.Л., Иванов Н.Ф., Морозов Б.А., Карбовская А.В. Способ флотационного разделения сульфидных медно-цинково-пиритных концентратов, содержащих активированные катионами меди и кальция сульфиды цинка: Патент 2054971 (РФ). 1996. https://www.elibrary.ru/item.asp?id=38031592
19. Kokorin A.M., Luchkov N.V., Smirnov A.O. Selective extraction method of copper minerals to concentrates at enrichment of copper-zinc pyrite-containing ores: Patent 242570 (RF). 2011. (In Russ.).
https://www.elibrary.ru/item.asp?id=37475002
Кокорин А.М., Лучков Н.В., Смирнов А.О. Способ селективного выделения медных минералов в концентраты при обогащении медно-цинковых пиротинсодержащих руд: Патент 242570 (РФ). 2011. https://www.elibrary.ru/item.asp?id=37475002
20. Zimbovsky I.G. Modern reagents-collectors for flotation of copper-zinc sulphide ores. *Gornyi informatsionno-analiticheskii byulleten*. 2013;(5):117—122. (In Russ.).
https://giab-online.ru/catalog/11943
Зимбовский И.Г. Современные реагенты-собиратели для флотации медно-цинковых сульфидных руд. *Горный информационно-аналитический бюллетень*. 2013;(5):117—122.
https://giab-online.ru/catalog/11943
21. Mamonov S.V., Volkova S.V., Chinova N.B., Khisamova A.S., Goraichuk P.K. Improving the technology of enrichment of copper-zinc ore from the pyrite deposit of the Ural type. *Minerals and Mining Engineering*. 2023;(3):86—96. (In Russ.).
https://doi.org/10.21440/0536-1028-2023-3-86-96
Мамонов С.В., Волкова С.В., Чинова Н.Б., Хисамова А.С., Горайчук П.К. Совершенствование технологии обогащения медно-цинковой руды колчеданного месторождения Уральского типа. *Известия высших учебных заведений. Горный журнал*. 2023;(3):86—96. https://doi.org/10.21440/0536-1028-2023-3-86-96
22. Zimin A.V., Arustamyan M.A., Kalinin E.P., Solov'yova L.M., Nemchinova L.A. Classification of technological schemes for flotation enrichment of pyrite copper and copper-zinc ores. *Mining Journal*. 2012;(11):28—33. (In Russ.).
https://www.rudmet.ru/journal/964/article/15148/
Зимин А.В., Арустамян М.А., Калинин Е.П., Соловьева Л.М., Немчинова Л.А. Классификация технологических схем флотационного обогащения колчеданных медных и медно-цинковых руд. *Горный журнал*. 2012;(11):28—33.
https://www.rudmet.ru/journal/964/article/15148/
23. Shekhirev D.V. Method for calculating material distribution by floatability. *Obogashchenie Rud*. 2022;(4):27—34. (In Russ.).
https://doi.org/10.17580/or.2022.04.05
Шехирев Д.В. Методика расчета распределения материала по флотируемости. *Обогащение руд*. 2022;(4):27—34. https://doi.org/10.17580/or.2022.04.05
24. Li Y., Zhao W., Gui X., Zhang X. Flotation kinetics and separation selectivity of coal size fractions. *Physicochemical Problems of Mineral Processing*. 2013;49(2):387—395.
http://dx.doi.org/10.5277/ppmp130201
25. Goryachev B.E., Nikolaev A.A., Ils'ina E.Yu. Analysis of flotation kinetics of particles with the controllable hydrophobic behavior. *Journal of Mining Science*. 2010;46:72—77.
https://doi.org/10.1007/s10913-010-0010-0
26. Goryachev B.E., Nikolaev A.A. Principles of kinetic "ion" modeling of adsorptive collector layer at the surface of nonferrous heavy metal sulfides. *Journal of Mining Science*. 2013;49:499—506.
https://doi.org/10.1134/S1062739149030180
27. Saroj K.S., Nikkam S., Atul K.V. Performance evaluation of basic flotation kinetic models using advanced statistical techniques. *International Journal of Coal Preparation and Utilization*. 2019;39(2):65—87.
http://dx.doi.org/10.1080/19392699.2017.1302436
28. Xiangning Bu, Liang Ge, Yale Peng, Cao Ni. Kinetics of flotation. Order of process, rate constant distribution and ultimate recovery. *Journal of Physicochemical Problems of Mineral Processing*. 2017;53(1):342—365.
http://dx.doi.org/10.5277/ppmp170128

Information about the authors

Htet Zaw Oo – Postgraduate Student of the Department of Mineral Processing, National University of Science and Technology "MISIS" (NUST MISIS).
https://orcid.org/0000-0003-2040-2552
E-mail: htetzawoo68099@gmail.com

Kyaw Zay Ya – Cand. Sci. (Eng.), Intern-Doctoral Student of the Department of Mineral Processing, NUST MISIS.
https://orcid.org/0000-0003-4364-9574
E-mail: kokyawgyi49@gmail.com

Boris E. Goryachev – Dr. Sci. (Eng.), Professor of the Department of Mineral Processing, NUST MISIS.
https://orcid.org/0000-0002-5164-5920
E-mail: beg@misis.ru

Информация об авторах

Хтет Зо У – аспирант кафедры обогащения полезных ископаемых (ОПИ), НИТУ МИСИС.
https://orcid.org/0000-0003-2040-2552
E-mail: htetzawoo68099@gmail.com

Чжо Зай Яа – к.т.н., стажер-докторант кафедры ОПИ, НИТУ МИСИС.
https://orcid.org/0000-0003-4364-9574
E-mail: kokyawgyi49@gmail.com

Борис Евгеньевич Горячев – д.т.н, профессор кафедры ОПИ, НИТУ МИСИС.
https://orcid.org/0000-0002-5164-5920
E-mail: beg@misis.ru

Contribution of the authors

Htet Zaw Oo – literature review and analysis, preparation of ore samples for research, performance of flotation experiments, analysis of experimental results, and writing of the manuscript.

Kyaw Zay Ya – literature review and analysis, evaluation of experimental data, participation in the discussion of results, and performance of theoretical calculations.

B.E. Goryachev – formulation of the study concept, definition of research objectives, discussion of experimental methods and obtained results, performance of calculations, and writing of the manuscript.

Вклад авторов

Хтет Зо У – сбор и анализ литературы, подготовка пробы руды для исследований, проведение экспериментов по флотации, анализ результатов экспериментов, написание статьи.

Чжо Зай Яа – сбор и анализ литературы, анализ экспериментальных данных, участие в обсуждении результатов, проведение теоретических расчетов.

Б.Е. Горячев – формулировка концепции работы, определение цели работы, обсуждение методики экспериментов и полученных результатов, выполнение расчетов, написание статьи.

The article was submitted 02.09.2024, revised 10.03.2025, accepted for publication 12.03.2025

Статья поступила в редакцию 02.09.2024, доработана 10.03.2025, подписана в печать 12.03.2025

METALLURGY OF NON-FERROUS METALS / МЕТАЛЛУРГИЯ ЦВЕТНЫХ МЕТАЛЛОВ

UDC 66.061.352
https://doi.org/10.17073/0021-3438-2025-4-18-29

Research article
Научная статья

Technology for recycling still residues from dehalogenation to produce commercial zinc compounds

V.A. Dorozhko, K.G. Chukreev, M.A. Afonin

St. Petersburg State Institute of Technology
24-26/49 Moskovskiy Prosp., St. Petersburg 190013, Russia

✉ Vladimir A. Dorozhko (dorozhko.ti@gmail.com)

Abstract: The study describes a method for recycling the still residue from the synthesis of hexafluoro-1,3-butadiene (HFBD) to produce zinc phosphate in the form of $Zn_3(PO_4)_2 \cdot 2H_2O$, which is used as a component in anti-corrosion pigment materials. The still residue ("heavy liquid") is preliminarily subjected to deep vacuum distillation (residual pressure 30 Pa, final temperature 160 °C) to recover volatile solvents-namely, isopropanol and dimethylformamide (DMF). The remaining residue is a concentrated solution of $ZnCl_2$ (about 70 wt. %) containing approximately 10 g/dm^3 of iron in the form of Fe(II) and Fe(III), as well as colored organic impurities of unidentified composition. According to the proposed process, the vacuum distillation residue is diluted with water at a ratio of 1 : 2, filtered to remove suspended solids, acidified to pH 2 by the addition of concentrated HCl, and treated oxidatively with H_2O_2 at 70 °C. Fe(III) is removed by extraction with a 30 % solution of Cyanex 272 in an aliphatic diluent, and the colored impurities are removed by adsorption onto BAU-1 grade activated carbon. An alternative method for removing Fe(III) and part of the colored impurities involves precipitating zinc in the form of $(ZnOH)_2CO_3$ using a 10 % Na_2CO_3 solution. Final clarification is also carried out using BAU-1 activated carbon. The purified, clear $ZnCl_2$ solution is then subjected to a two-step precipitation process to obtain zinc phosphate. The resulting precipitate is filtered, thoroughly washed with water, dried, and ground. The study showed that after drying at 100–105 °C, the resulting powder corresponds to the composition $Zn_3(PO_4)_2 \cdot 2H_2O$. The content of regulated impurities falls within acceptable limits, and the properties of the material meet the requirements for pigment-grade substances. A comparison of the obtained zinc phosphate with a commercially available sample of pigment-grade zinc phosphate was conducted. It was established that the proposed technology yields 580 g of zinc phosphate dihydrate per 1 kg of initial raw material.

Key words: waste, hexafluoro-1,3-butadiene, heavy liquid, zinc chloride, zinc phosphate, refining.

Acknowledgements: This study was supported by the Russian Science Foundation (Project No. 21-79-30029) and the Ministry of Science and Higher Education of the Russian Federation (State Assignment 0785.00.X6019).

For citation: Dorozhko V.A., Chukreev K.G., Afonin M.A. Technology for recycling still residues from dehalogenation to produce commercial zinc compounds. *Izvestiya. Non-Ferrous Metallurgy.* 2025;31(4):18–29. https://doi.org/10.17073/0021-3438-2025-4-18-29

Технология утилизации кубовых остатков дегалогенирования с получением товарных соединений цинка

В.А. Дорожко, К.Г. Чукреев, М.А. Афонин

Санкт-Петербургский государственный технологический институт (технический университет)
Россия, 190013, г. Санкт-Петербург, Московский пр-т, 24-26/49

✉ Владимир Александрович Дорожко (dorozhko.ti@gmail.com)

Аннотация: В работе описан способ утилизации кубового остатка синтеза гексафтор-1,3-бутадиена (ГФБД) с получением фосфата цинка в форме $Zn_3(PO_4)_2 \cdot 2H_2O$, применяемого в качестве компонента антикоррозионных пигментных материалов. Кубовый

остаток («тяжелая жидкость») предложено предварительно подвергнуть глубокой вакуумной дистилляции (остаточное давление 30 Па, температура окончания процесса 160 °С) для извлечения летучих растворителей, изопропанола и диметилформамида (ДМФА). Остаток представляет собой концентрированный раствор $ZnCl_2$ (около 70 мас. %), содержит около 10 г/дм^3 железа в форме Fe(II) и Fe(III), а также окрашенные органические примеси неустановленного состава. По разработанной технологии остаток вакуумной дистилляции предложено разбавить водой в соотношении 1 : 2, отфильтровать от взвешенных частиц, скорректировать pH до 2 введением концентрированной HCl, провести окислительную обработку H_2O_2 при температуре 70 °С. Железо (III) из раствора предложено отделять экстракцией 30 %-ным раствором Cyanex 272 в алифатическом разбавителе, а окрашенные примеси – сорбцией на активном угле марки БАУ-1. Альтернативным способом удаления Fe(III) и части других окрашенных примесей является осаждение цинка в форме $(ZnOH)_2CO_3$ обработкой 10 %-ным раствором Na_2CO_3. Окончательное осветление раствора также происходит на активном угле марки БАУ-1. Очищенный прозрачный раствор $ZnCl_2$ подается на двухступенчатое осаждение фосфата цинка, полученный осадок фильтруется, тщательно промывается водой, высушивается и измельчается. В ходе исследования установлено, что после высушивания при температуре 100–105 °С полученный порошок отвечает составу $Zn_3(PO_4)_2 \cdot 2H_2O$, содержание посторонних регламентируемых примесей находится в рамках допуска, а свойства материала удовлетворяют требованиям, предъявляемым к материалу пигментного класса. Проведено сравнение характеристик полученного фосфата цинка и коммерчески доступного образца пигментного фосфата цинка. Определено, что с использованием предложенной технологии из 1 кг исходного сырья может быть получено 580 г двуводного фосфата цинка.

Ключевые слова: отходы, гексафтор-1,3-бутадиен (ГФБД), «тяжелая жидкость», хлористый цинк, фосфат цинка, рафинирование.

Благодарности: Исследование выполнено при финансовой поддержке Российского научного фонда (проект №21-79-30029) и Министерства науки и высшего образования Российской Федерации (госзадание 0785.00.Х6019).

Для цитирования: Дорожко В.А., Чукреев К.Г., Афонин М.А. Технология утилизации кубовых остатков дегалогенирования с получением товарных соединений цинка. *Известия вузов. Цветная металлургия.* 2025;31(4):18–29.
https://doi.org/10.17073/0021-3438-2025-4-18-29

Introduction

A current research trend in the production of high-demand chemical compounds involves the recycling of accumulated and newly generated technogenic waste. The domestic paint and coatings industry has a demand for zinc-based pigments such as zinc white (zinc oxide), zinc chromate (zinc yellow), lithopone, and anti-corrosion formulations based on zinc—calcium medium or double phosphate. This entire group of zinc-containing pigments can be produced through the processing of a wide range of industrial waste materials.

The authors of [1] examined the synthesis of zinc—calcium mixed phosphate in chloride systems by precipitation with ammonium hydrogen phosphate. Studies [2—4] describe the synthesis and properties of anti-corrosion pigments based on zinc phosphate with benzotriazole (BTA) additives, while [5] demonstrates that changing the molar ratio of $ZnCl_2$/KOH influences the formation of $KZn_2H(PO_4)_2$ and $KZnPO_4$ phases. It was found that $KZn_2H(PO_4)_2$ exhibits better inhibiting properties in a 3.5 % NaCl solution compared to $KZnPO_4$. In [6], zinc phosphate with a Zn/P ratio of approximately 1.5 was synthesized and characterized, with potential applications in the cosmetics industry. A method for synthesizing crystalline α-$Zn_3(PO_4)_2 \cdot 4H_2O$ was proposed in [7], where the morphology was controlled by adjusting the pH of the reaction medium.

Papers [8; 9] describe the synthesis and application of rose-like sheet zinc phosphate (SZP), as well as three-dimensional flower-like pigments based on micro- and nanoscale zinc phosphate (FZP) and ammonium—zinc phosphate (FNZP), used as anti-corrosion fillers in waterborne epoxy-modified acrylic resin. In [10], a comparative study was carried out between unmodified calcium zinc phosphate nanopigments (UCZP) and their methyltriethoxysilane-modified counterparts (MCZP). The potential use of dispersed hot-dip galvanizing waste as a component of zinc-rich coatings was explored in [11], while [12] examined the synthesis of zinc-containing pigment compounds from spent electroplating solutions. Patent [13] proposes a method for processing such solutions to obtain commercial-grade compounds. In [14], pigment-grade zinc oxide was obtained via alkaline treatment of solid galvanic sludge from the zinc-coating line at Signal-Nedvizhimost LLC (Russia). The feasibility of using electroplating sludge as a raw material for the production of inorganic pigments, including zinc-based ones, was further investigated in [15; 16].

In [17], the catalytic properties of zinc and iron phosphates in methanol conversion were investigated, with particular attention to the hydrothermal synthesis of a mixed phosphate in the R—$ZnO(Fe_2O_3)$—P_2O_5—H_2O system (where R is an organic or inorganic base).

Novel core—shell nanostructures of zinc phosphate/hydroxyapatite nanorods (ZPh/HPA_{NRs}) were synthesized and characterized as a modified form of hydroxyapatite with enhanced adsorption capacity for Ni^{2+} and Co^{2+} ions [18]. The application of zinc phosphate with various binders as electrode material for supercapacitors was explored in [19].

A method for producing zinc-free phosphate pigments containing strontium, calcium, and aluminum is presented in [20], along with their chemical composition, physicochemical, and anti-corrosion properties. This approach is relevant in view of environmental concerns and regulatory restrictions on the use of zinc-based anti-corrosion pigments in the European Union. The rapid and extensive release of Zn^{2+} ions from commercial lithopone pigment under solar light exposure was reported in [21], where approximately 41 % of the total Zn content was released after 24 h of simulated solar exposure.

The application of zinc phosphates as micronutrient fertilizers and feed additives in agriculture was studied in [22], while [23] examined the synthesis of ZnO nanoparticles and their use as nano-fertilizers in original form or as ferrite or zinc phosphate composites.

Russia is one of the few global producers of hexafluoro-1,3-butadiene (HFBD) and hexafluorobenzene, which are electronic gases used in plasma etching of silicon thin films during the manufacturing of microelectronic devices with 15—25 nm design standards, for creating grooves and vias. HFBD is considered one of the most ozone-safe gases for plasma etching applications. In 2016, new production facilities with an annual capacity of up to 72 tons of HFBD were commissioned in Perm, Russia.

The commercial HFBD production technology used in Russia is described in patents [24—27]. Patent [28] proposes using alternative precursors to obtain a purer product without additional purification steps.

According to [24], a method was proposed for synthesizing 1,2,3,4-tetrachlorohexafluorobutane, which serves as a precursor for the production of hexafluoro-1,3-butadiene (HFBD). The process involves the reaction of 1-iodo-1,2,2-trifluoro-1,2-dichloroethane with zinc in the presence of an organic oxygen-containing complexing agent (cat), in accordance with the following equation:

$$I-CF(Cl)-CF_2Cl+Zn \xrightarrow{\text{cat, 0–45 °C}} \xrightarrow{\text{cat, 0–45 °C}} ClF_2C-CF(Cl)-CF(Cl)-CF_2Cl+ZnI_2. \quad (1)$$

The process is carried out by introducing an organic oxygen-containing complexing agent (cat) into the mixture of starting reagents at a temperature of 0—45 °C. After completion of the reaction, 1,2,3,4-tetrachlorohexafluorobutane is isolated by rectification.

According to the method described in [25], hexafluoro-1,3-butadiene (HFBD) is synthesized by reacting 1,2,3,4-tetrachlorohexafluorobutane with granular zinc in a water—alcohol medium at 30—90 °C. The synthesis is performed by gradually dosing 1,2,3,4-tetrachlorohexafluorobutane into a reagent mixture containing metallic zinc and water, while simultaneously distilling off the target product, in accordance with the following equation:

$$ClF_2C-CF(Cl)-CF(Cl)-CF_2Cl+2Zn \xrightarrow{\text{30–90 °C, } H_2O} \xrightarrow{\text{30–90 °C, } H_2O} F_2C=CF-CF=CF_2\uparrow+2ZnCl_2. \quad (2)$$

Upon completion of dosing, the reaction mixture is heated to boiling to ensure full dechlorination.

In [29], the mechanism of Fe(III) extraction by Cyanex 272 (bis(2,2,4-trimethylpentyl)phosphinic acid) was studied using a combination of methods, including ^1H NMR spectroscopy, mass spectrometry, and others. The extraction of Fe(III) from technical-grade phosphoric acid solutions using a related cation-exchange extractant, Cyanex 572, was described in [30]. The use of cation-exchange Cyanex extractants for the removal of Fe(III) from leach solutions of nickel ores was reported in [31]. The authors of [32] noted the challenges of Fe(III) stripping and proposed strategies to improve the regeneration efficiency of cation-exchange Cyanex extractants. Previously, we studied the extraction of Fe(III) from HCl solutions using 1-undecanol [33].

The application of cation-exchange extractants, including Cyanex 272, for the purification of zinc-containing solutions was discussed in [34]. The use of liquid—liquid extraction with Aliquat 336 to recover non-ferrous metals, including Zn(II), from process solutions generated during electronic waste recycling was described in [35]. In [36], the authors proposed a polyethylene glycol—sodium sulfate system (PEG-1500—Na_2SO_4) as an extractant for processing Zn-containing solutions.

The aim of the present study was to develop an efficient process scheme for recycling the still residue from the dehalogenation of 1,2,3,4-tetrachloroperfluorobutane, with the recovery of zinc orthophosphate as the target product.

1. Processing technology

The figure shows a flow diagram of the process used to treat the feedstock — the still residue from vacuum distillation of dehalognation waste.

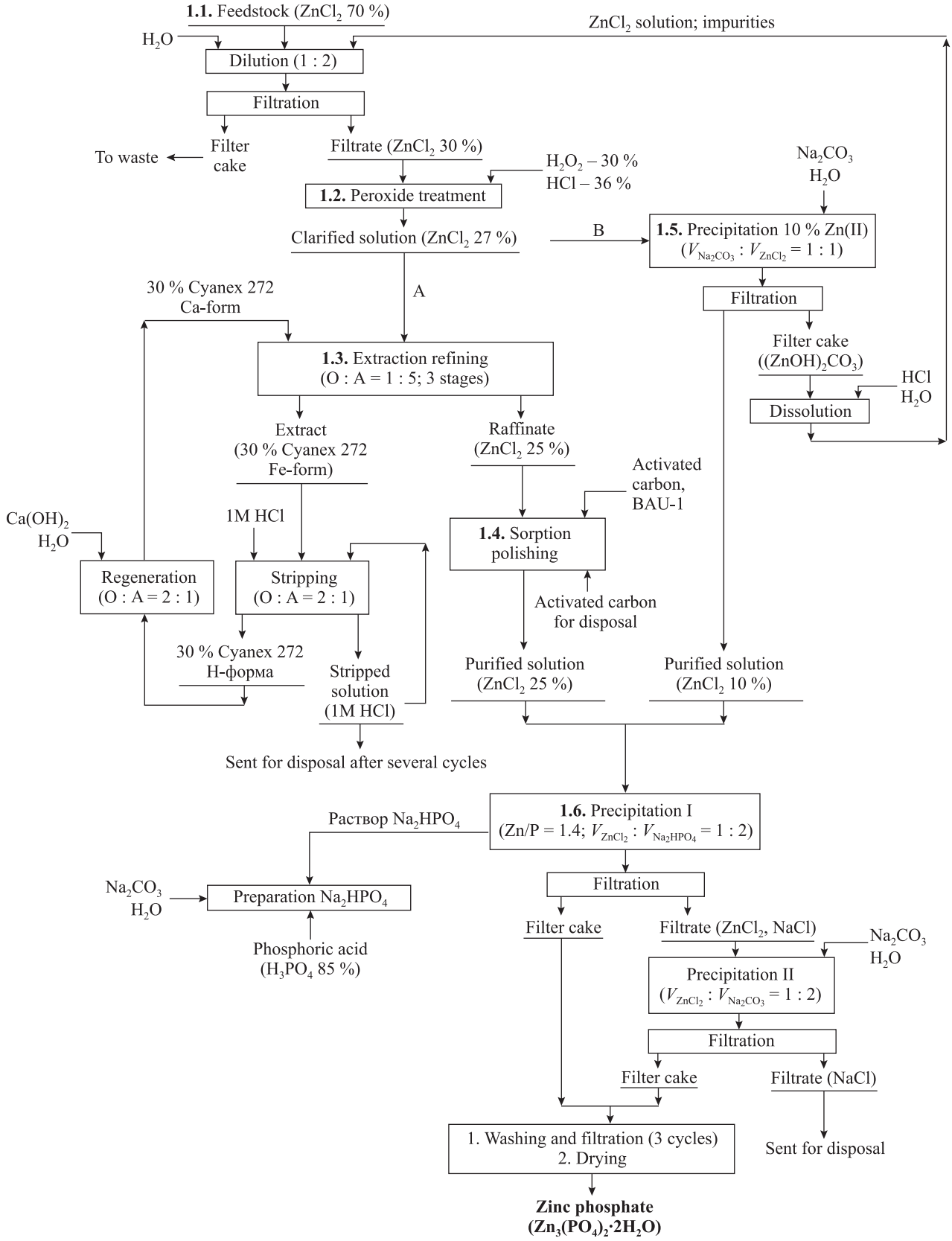

Flow diagram of the processing of the still residue from deep vacuum distillation of “heavy liquid” to produce commercial-grade zinc phosphate

Схема переработки кубового остатка глубокой вакуумной дистиляции «тяжелой жидкости» с получением товарного фосфата цинка

1.1. Feedstock

The so-called "heavy liquid" represents a combined discharge of liquid waste generated at all stages of HFBD production, as well as from the synthesis of precursor compounds. The synthesis of 1000 kg of hexafluoro-1,3-butadiene (HFBD) yields approximately 120 kg of waste ("heavy liquid"), consisting of the following: products of partial dehalogenation of 1,2,3,4-tetrachlorohexafluorobutane (TCHFBD); products of partial reduction of HFBD by zinc; chlorinated hydrocarbons; zinc chloride ($ZnCl_2$) in solution in either isopropanol (IPA) or dimethylformamide (DMF). Zinc chloride is also formed via the chlorine conversion of ZnI_2, which is produced during the synthesis of 1,2,3,4-tetrachlorohexafluorobutane [24].

To recover isopropanol, the "heavy liquid" undergoes deep vacuum distillation in a Formeco unit (Italy) at a residual pressure of approximately 30 Pa and up to a final temperature of 160 °C. The resulting feedstock is a viscous, opaque, syrup-like oily liquid with an ether-like odor, containing suspended impurities.

The density of the solutions was measured using ~5 mL pycnometers on an analytical balance with a precision of ±0.0001 g. The density measurement accuracy was ±0.001 g/cm^3.

The Fe(III) concentration was determined by the thiocyanate spectrophotometric method according to [37], using a calibration curve. Fe(II) in the samples was oxidized to Fe(III) by adding an excess of potassium peroxodisulfate.

The Zn(II) concentration was determined by direct complexometric titration using eriochrome black T as an indicator in accordance with [38]. The concentration was found to be 9.0 ± 0.1 mol/dm^3.

The key parameters of the initial feedstock are listed below:

$ZnCl_2$ concentration, g/dm^3..... 1340 ± 15
Total iron content, g/dm^3 .....5.8 ± 0.1
Feedstock density, g/cm^3.....1.910 ± 0.001

1.2. Peroxide treatment

Preliminary experiments showed that the initial feedstock contained Fe(II) and Fe(III) compounds as colored impurities, as well as unidentified organic contaminants. The feedstock was diluted with water at a volume ratio of 1 : 2. The resulting solution was filtered through a pre-coated sand layer using a Büchner funnel. Exposure to concentrated zinc chloride solutions leads to the dissolution of paper and fabric, causing traditional filter membranes to fail rapidly.

To oxidize iron into the Fe(III) state and to promote the oxidative degradation of organic impurities, the filtrate was sequentially treated with concentrated HCl and H_2O_2 as follows: 100 mL of the filtrate was placed in a beaker and heated in a water bath for 30 min. Then, every 10 min, 1 cm^3 of H_2O_2 and 1 cm^3 of concentrated HCl were alternately added to the hot solution under stirring, for a total of four additions. Each addition of H_2O_2 and HCl caused the solution to foam, followed by clarification, indicating the oxidation of organic impurities and the decomposition of colored Fe(III) complexes. The oxidation process was carried out for 1.5 h, and by the end of the treatment, the pH of the solution had decreased to 2.

1.3. Solvent extraction of iron (III)

Cyanex 272 (bis(2,2,4-trimethylpentyl)phosphinic acid), a commercial weakly acidic organophosphorus extractant, was selected as the extractant. Its selection was based on its low acidity, which facilitates the stripping of Fe(III) — a highly extractable ion with strong affinity for cation-exchange extractants. A 30 % solution of Cyanex 272 in a mixture of Isopar-L and tributyl phosphate (in a volume ratio of 9 : 1) was used as the diluent. The Cyanex 272 concentration, determined by potentiometric titration, was 0.73 ± 0.01 mol/dm^3. The extractant was first converted into the Ca-form (30 %) by mixing with dilute water containing slaked lime, and then into the Zn-form by contacting with a zinc chloride solution.

To extract Fe(III), the filtered and oxidized solution was treated with three portions of the extractant at an extractant-to-aqueous phase volume ratio of 1 : 5.

The residual Fe(III) concentration in the aqueous phase, determined by spectrophotometry, was approximately 40 mg/dm^3.

1.4. Sorption polishing of the raffinate

Following extraction, a yellowish transparent raffinate was obtained. To remove the residual yellow tint, sorption polishing was applied. Prior to that, the effectiveness of several sorbents — Purolite MN200, Purolite XDA1, and BAU-1 activated carbon—was assessed. For the test, 15 g of each sorbent was added to 50 cm^3 of raffinate.

During static sorption treatment, BAU-1 activated carbon demonstrated the best performance: the solution became clear and colorless, with no visible yellow tint. The solutions treated with resins retained a noticeable yellow coloration. Based on these results, BAU-1 acti-

vated carbon was selected as the sorbent for the sorption polishing stage.

A volume of 160 cm^3 of raffinate was transferred to a beaker and 15 g of activated carbon was added. The sorption process was carried out under periodic stirring for 2 days. During this time, the original zinc chloride solution became fully decolorized. The zinc concentration, determined by titrimetric analysis, was found to be 3.6 ± 0.1 mol/dm^3.

1.5. Clarification of the peroxide-treated solution via zinc carbonate precipitation

To remove Fe(III) from the zinc chloride solution, it was proposed to co-precipitate 10 % of the zinc in the form of zinc hydroxycarbonate, $(ZnOH)_2CO_3$. This method allows the extraction stage for Fe(III) removal to be omitted, while the peroxide oxidation step can be carried out using a lower amount of peroxide — just enough to oxidize Fe(II) to Fe(III). As a result of co-precipitation of Fe(III) and adsorbed organic impurities on amorphous zinc hydroxide, the solution can be clarified more effectively.

Zinc precipitation with sodium carbonate occurs in the form of zinc hydroxycarbonate according to the following reaction:

$$2ZnCl_2 + 2Na_2CO_3 + 2H_2O \rightarrow$$
$$\rightarrow (ZnOH)_2CO_3\downarrow + 4NaCl + CO_2\uparrow. \quad (3)$$

To precipitate 10 % of the zinc from the initial solution, a weighed portion of sodium carbonate was dissolved in an equal volume of water and slowly added to the zinc chloride solution under vigorous stirring over 30 min. The resulting suspension was then filtered through a “blue ribbon” filter to obtain a clear, colorless filtrate. The resulting contaminated filter cake can be dissolved in hydrochloric acid and reintroduced into the main solution during its dilution.

1.6. Precipitation of zinc phosphate

According to the standard procedure [39], sodium hydrogen phosphate is used for the precipitation of zinc orthophosphate. The precipitation occurs according to the following reaction:

$$3ZnCl_2 + 4Na_2HPO_4 + 4H_2O \rightarrow$$
$$\rightarrow Zn_3(PO_4)_2\cdot 4H_2O\downarrow + 2NaH_2PO_4 + 6NaCl. \quad (4)$$

The purified zinc chloride solution and the sodium hydrogen phosphate solution were mixed so that the molar ratio Zn : P was maintained at 1.4.

Sodium hydrogen phosphate (Na_2HPO_4) was prepared by mixing solutions of sodium carbonate and orthophosphoric acid in stoichiometric amounts according to the reaction:

$$Na_2CO_3 + H_3PO_4 \rightarrow$$
$$\rightarrow Na_2HPO_4 + H_2O + CO_2\uparrow. \quad (5)$$

The weights of the reagents were calculated based on the Zn(II) concentration in the feed solution, which ranged from 3 to 4 M.

To prepare the sodium hydrogen phosphate solution, 26.7 g of sodium carbonate was dissolved in 100 cm^3 of water and added to an 85 % orthophosphoric acid solution (29.0 g) previously dissolved in 250 cm^3 of water. After neutralization, the prepared sodium hydrogen phosphate solution was used to precipitate zinc orthophosphate by adding it to 150 mL of the purified zinc chloride solution, in accordance with reaction (4). Thus, the volume ratio Zn^{2+}/HPO_4^{2-} was approximately 1 : 2. During precipitation, a flocculent precipitate formed. After stirring the reaction mixture for 10 min, the zinc phosphate precipitate was filtered through a Büchner funnel using a “blue ribbon” filter, and the filtrate was returned to the reactor for further precipitation of zinc phosphate. The precipitate was washed twice by repulping with water at a solid-to-liquid ratio of 1 : 10, followed by an additional washing step directly on the filter using heated water (also at a 1 : 10 ratio). The resulting zinc orthophosphate was then dried at 100 °C and subsequently calcined at 250 °C.

Since, as indicated by reaction (6), half of the sodium hydrogen phosphate is converted to sodium dihydrogen phosphate, incomplete precipitation of zinc occurs. The solution becomes increasingly acidic, and equilibrium is established at pH = 2. To ensure complete precipitation of zinc as zinc phosphate and full consumption of the orthophosphoric acid, it was proposed to carry out an additional precipitation step by neutralizing the excess acidity with sodium carbonate.

To prepare the sodium carbonate solution for the additional precipitation, 11.8 g of sodium carbonate was dissolved in 100 cm^3 of water. The resulting solution was added to the mother liquor to precipitate the remaining zinc phosphate according to the following reaction:

$$3ZnCl_2 + 2NaH_2PO_4 + 2Na_2CO_3 + 2H_2O \rightarrow$$
$$\rightarrow Zn_3(PO_4)_2\cdot 4H_2O\downarrow + 6NaCl + 2CO_2\uparrow. \quad (6)$$

The procedure for precipitating zinc phosphate from the mother liquor was analogous to that described pre-

Table 1. **Gravimetric determination of precipitate moisture content**

Таблица 1. Результаты измерения влажности осадков

Stage	m_{100}, g	m_{250}, g	m_{H_2O}, g	ω_{H_2O}, %
Primary precipitation	32.9	30.0	2.9	8.8
Additional precipitation	27.1	24.9	2.2	8.1

viously. Upon addition of the sodium carbonate solution, gas evolution, foaming, and the formation of a white flocculent precipitate were observed. The reaction mixture was stirred for 10—15 min. The precipitate was filtered and dried following the same method as for the initial precipitation.

The masses of the precipitates obtained after the precipitation and additional precipitation steps were determined after drying at 100 °C (m_{100}) and 250 °C (m_{250}). The mass loss upon drying at 250 °C and the water content were calculated using the following formulas:

$$\Delta m_{H_2O} = m_{100} - m_{250}, \quad (7)$$

$$\omega_{H_2O} = \frac{m_{H_2O}}{m_{100}} \cdot 100\ \%. \quad (8)$$

The moisture content of the obtained precipitates, determined gravimetrically, is presented in Table 1. The loss of moisture upon heating from 100 °C to 250 °C corresponds to the behavior of zinc phosphate in the form of $Zn_3(PO_4)_2 \cdot 2H_2O$ after drying at 100 °C. Thus, both anhydrous and dihydrate forms of zinc phosphate can be obtained, both of which are highly sought after for use in the production of pigment materials.

2. Characterization of the synthesized zinc phosphate

2.1. Oil absorption of pigments

One of the key characteristics of technical pigment materials is their oil absorption. According to GOST 21119.8-75, oil absorption of the first kind is defined as the amount of oil (in grams) required to produce 100 g of a homogeneous pigment paste. It is determined as follows: a sample of the pigment is gradually mixed with linseed oil, grinding the mixture until a uniform paste is obtained. The amount of oil consumed in the test is then recorded and rounded to the nearest whole number [34].

In our case, 1.44 g of oil was used to wet approximately 5 g of the pigment sample. The oil absorption was calculated using the formula:

$$X = \frac{0.93V}{m} \cdot 100, \quad (9)$$

where V is the volume of linseed oil used during testing (cm^3); m is the mass of the pigment sample (g); and 0.93 is the density of linseed oil (g/cm^3).

As a result, the oil absorption of the obtained pigment was 29 g_{oil}/100 $g_{pigment}$.

2.2. Elemental analysis of zinc phosphate

The elemental composition of the zinc phosphate samples was determined using an *X*-ray fluorescence analyzer integrated into the VEGA 3 SBH scanning electron microscope (TESCAN, Czech Republic) at the Engineering Center of the St. Petersburg State Institute of Technology (Technical University). Samples dried at 250 °C and prepared as a white powder were used for the analysis.

The results are presented in Table 2, based on which the contents of the main compounds in the pigment were calculated:

Zinc compounds (as Zn), wt. % 50.6

Phosphorus compounds (as PO_4), wt. % 49.1

Table 3 presents the specification values for a commercial-grade pigment sample used in paints (Neo-PZ, manufactured by PS Akvilon LLC), along with the properties of the zinc phosphate pigment obtained in this study after drying at 100 °C, corresponding to the composition $Zn_3(PO_4)_2 \cdot 2H_2O$.

The test results confirm that the synthesized zinc phosphate dihydrate meets all standard requirements for zinc phosphate pigment materials.

3. Results

A method has been proposed for processing the hazardous waste currently accumulating, enabling the

Table 2. **Elemental composition of zinc phosphate samples**

Таблица 2. Элементный состав образцов фосфата цинка

Sample	Content, wt. % (at. %)			
	O	P	Cl	Zn
Precipitate	35.55 (64.61)	13.56 (12.73)	0.08 (0.06)	50.62 (22.51)
Mother liquor	36.69 (64.38)	13.17 (11.72)	0.06 (0.05)	47.07 (19.85)

Table 3. **Test results of the zinc phosphate pigment for use in Neo-PZ paints (PS Akvilon LLC)**

Таблица 3. Результаты испытаний цинкофосфатного пигмента для красок Neo-PZ предприятия ООО «ПС Аквилон»

Sample	Zinc compounds (as Zn), wt. %	Phosphorus compounds (as PO_4), wt.%	pH of aqueous suspension	Δm_{600}, %	Particle size (residue on No. 0045 sieve), wt. %	Appearance
Specification for Neo-PZ	40–47	40–47	7–9	8–16	≤0.5	White powder
Test results for synthesized pigment	43.2	45.5	8.1	10.2	Trace	Complies

recovery of valuable solvents—isopropanol and dimethylformamide (DMF) — which are presently not produced in Russia. At the same time, the large-scale recovery of these solvents is not feasible without addressing the problem of utilizing the still residue. The processing technology for the still residue, developed within the scope of this study, comprises the following stages.

1. Dilution of the still residue from the vacuum distillation of the heavy liquid with water and subsequent filtration ($V_{feedstock}$ = 50 cm^3, V_{H_2O} = 100 mL).

2. Treatment of the filtrate with a 31 % hydrogen peroxide solution and a 36 % hydrochloric acid solution under heating to 80 °C ($V_{H_2O_2}$ = 4 mL, V_{HCl} = 4 mL).

3.1. Solvent extraction of Fe(III) using a 0.8 M solution of Cyanex 272 (3×20 mL, organic phase to aqueous phase ratio O : A = 1 : 5); followed by sorption purification of the raffinate ($m_{BAU\text{-}1}$ = 15 g).

3.2. Alternatively to Stage 3.1, precipitation of $(ZnOH)_2CO_3$ and organic impurities by treatment with a sodium carbonate solution (V_{H_2O} = 100 mL, $m_{Na_2CO_3}$ = = 4.24 g).

4. Precipitation of zinc phosphate by treatment with Na_2HPO_4 ($m_{Na_2CO_3}$ = 26.7 g, $m_{H_3PO_4}$ = 29.0 g, V_{H_2O} = = 350 mL), followed by additional treatment with a sodium carbonate solution ($m_{Na_2CO_3}$ = 11.8 g, V_{H_2O} = = 100 mL).

The amount of $Zn_3(PO_4)_2 \cdot 2H_2O$ that can be obtained from 1 kg of initial feedstock is approximately 580 g.

In addition to zinc phosphate, the developed technology also allows the production of $ZnCO_3$, ZnO, and a refined concentrated $ZnCl_2$ solution ($ZnCl_2$ concentration > 50 %).

Conclusion

A technological scheme has been developed for producing pigment-grade zinc phosphate from zinc chloride contaminated with impurities, a waste by-product of the dehalogenation process. The concentrations of iron and zinc chloride in the initial feedstock were determined.

Experimental results showed that treating the diluted feedstock with hydrogen peroxide in the presence of hydrochloric acid under heating promotes the decomposition of colored organic impurities, which impede the separation of iron and the complete

decolorization of the solution. Both solvent extraction and precipitation methods for achieving complete decolorization of the zinc chloride solution were proposed. As a result of the two-stage precipitation process, zinc orthophosphate was obtained as the final product. The pigment's oil absorption was determined experimentally, and its elemental composition was established.

Comparison of the synthesized product's characteristics with those of the commercial Neo-PZ zinc phosphate pigment (PS Akvilon LLC) confirmed that the properties of the synthesized material fully meet the standards for pigment-grade zinc phosphate.

References

1. Antraptseva N., Filkin I. The investigation of the conditions for obtaining double zinc-calcium phosphate. *Sworld Journal*. 2021;7(3):12—15. https://doi.org/10.30888/2410-6615.2020-07-03-073
2. Bhanvase B.A., Kutbuddin Y., Borse R.N., Selokar N.R., Pinjari D.V., Gogate P.R., Sonawane S.H., Pandit A.B. Ultrasound assisted synthesis of calcium zinc phosphate pigment and its application in nanocontainer for active anticorrosion coatings. *Chemical Engineering Journal*. 2013;231:345—354. https://doi.org/10.1016/j.cej.2013.07.030
3. Miao M., Yuan X.Yu., Wang X.G., Lu Y., Liu J.K. One step self-heating synthesis and their excellent anticorrosion performance of zinc phosphate/benzotriazole composite pigments. *Dyes and Pigments*. 2017;141:74—82. https://doi.org/10.1016/j.dyepig.2017.01.060
4. Askari F., Ghasemi E., Ramezanzadeh B., Mahdavian M. Synthesis and characterization of the fourth generation of zinc phosphate pigment in the presence of benzotriazole. *Dyes and Pigments*. 2016;124:18—26. https://doi.org/10.1016/j.dyepig.2015.08.020
5. Askari F., Ghasemi E., Ramezanzadeh B., Mahdavian M. Effects of KOH : $ZnCl_2$ mole ratio on the phase formation, morphological and inhibitive properties of potassium zinc phosphate (PZP) pigments. *Journal of Alloys and Compounds*. 2015;631:138—145. https://doi.org/10.1016/j.jallcom.2014.12.160
6. Onoda H., Haruki M., Toyama T. Preparation and powder properties of zinc phosphates with additives. *Ceramics International*. 2014;40(2):3433—3438. https://doi.org/10.1016/j.ceramint.2013.09.088
7. Zhou X., Bai H., Ma H., Li H., Yuan W., Du H., Zhang P., Xin H. Synthesis of zinc phosphate and zinc ammonium phosphate nanostructures with different morphologies through pH control. *Materials Characterization*. 2015;108:22—28. https://doi.org/10.1016/j.matchar.2015.08.012
8. Chen Y., Wang J., Wen S., Zhang J., Yu X., Mao Y. Synthesis of rose-like sheet zinc phosphate by the induction-calcination method and its application as a corrosion inhibitor in coatings. *International Journal of Electrochemical Science*. 2021;16(4):210—246. https://doi.org/10.20964/2021.04.63
9. Zhang Y., Li X., Yang D., Cai H., Ma Z., Zhang Y., Cui S., Wu Z. Incorporation of NH_4^+ in flower-like zinc phosphate pigment to enhance the corrosion resistance of waterborne epoxy. *Materials Letters*. 2024;358:135—157. https://doi.org/10.1016/j.matlet.2023.135850
10. Haddadi S.A., Alibakhshi E., Motlagh A.L., Ramazani A., Ghaderi M., Ramezanzadeh B., Mahdavian M., Arjmand M. Synthesis of methyltriethoxysilane-modified calcium zinc phosphate nanopigments toward epoxy nanocomposite coatings: Exploring rheological, mechanical, and anti-corrosion properties. *Progress in Organic Coatings*. 2022;171:107—115. https://doi.org/10.1016/j.porgcoat.2022.107055
11. Urbanovich N.I., Baranovsky K.E., Rosenberg E.V., Bendik T.I., Karpenkin A.A. Analysis of the corrosion properties of zinc-containing coatings based on dispersed hot-dip galvanizing waste. *Lit'e i metallurgiya*. 2020;(4):106—112. (In Russ.). https://doi.org/10.21122/1683-6065-2020-4-106-112
Урбанович Н.И., Барановский К.Э., Розенберг Е.В., Бендик Т.И., Карпенкин А.А. Анализ коррозионных свойств цинксодержащих покрытий на базе дисперсного отхода горячего цинкования. *Литье и металлургия*. 2020;(4):106—112. https://doi.org/10.21122/1683-6065-2020-4-106-112
12. Syrchina N.V., Ashikhmina T.Ya., Kantor G.Ya. Obtaining inorganic pigments from electroplating waste. *Teoreticheskie problemy ekologii*. 2021;(1):22—29. (In Russ.). https://doi.org/10.25750/1995-4301-2021-1-022-029
Сырчина Н.В., Ашихмина Т.Я., Кантор Г.Я. Получение неорганических пигментов из отходов гальванических производств. *Теоретические проблемы экологии*. 2021;(1):22—29. https://doi.org/10.25750/1995-4301-2021-1-022-029
13. Barkhatov V.I., Dobrovolsky I.P., Kapkaev Yu.Sh., Golovachev I.V. A method for processing spent acidic solutions of galvanic industries: Patent 2690328 (RF). 2018. (In Russ.).
Бархатов В.И., Добровольский И.П., Капкаев Ю.Ш., Головачев И.В. Способ переработки отработанных кислых растворов гальванических производств: Патент 2690328 (РФ). 2019.

14. Olshanskaya L.N., Lazareva E.N., Voloshkina Yu.V. Galvanic sludge — as a source of secondary resources for the production of industrial goods. *Promyshlennye protsessy i tekhnologii*. 2023;3(1(8)):7—14. (In Russ.).
https://doi.org/10.37816/2713-0789-2023-3-1(8)-7-14
Ольшанская Л.Н., Лазарева Е.Н., Волошкина Ю.В. Гальваношламы — как источник вторичных ресурсов для получения промышленных товаров. *Промышленные процессы и технологии*. 2023;3(1(8)):7—14.
https://doi.org/10.37816/2713-0789-2023-3-1(8)-7-14
15. Becker J., Selbach I.C., Souza J.D., Brehm F.A. Viability for the production of inorganic pigments from galvanic sludge. *International Journal of Research in Advanced Engineering and Technology*. 2019;5(3):98—103.
https://doi.org/10.6084/m9.figshare.12317375
16. Marcus M.I., Vlad M., Deák G., Moncea A., Panait A.M., Movileanu G. Thermal stability of inorganic pigments synthesized from galvanic sludge. *Revista de Chimie*. 2020;71(8):13—20.
https://doi.org/10.37358/RC.20.8.8274
17. Tagiyev D.B., Aliyev A.M., Mamedov N.D., Fatullayeva S.S. Hydrothermal synthesis of zeolite-like iron and zinc phosphates and its application in the methanol conversion. *Studies in Surface Science and Catalysis*. 2004;154(A):1049—1055.
https://doi.org/10.1016/S0167-2991(04)80923-6
18. Sayed I.R., Farhan A.M., Al Hammadi A.A., El-Sayed M.I., Abd El-Gaied I.M., El-Sherbeeny A.M., Al Zoubi W., Gun Ko.Y., Abukhadra M.R. Synthesis of novel nanoporous zinc phosphate/hydroxyapatite nano-rods (ZPh/HPANRs) core/shell for enhanced adsorption of Ni^{2+} and Co^{2+} ions: Characterization and application. *Journal of Molecular Liquids*. 2022;360:119—127.
https://doi.org/10.1016/j.molliq.2022.119527
19. Fazal A., Iqbal M.J., Raza M.A., Almutairi B.S., Iqbal M.Z., Subhani T., Riaz S., Naseem S. Binder-free hydrothermal approach to fabricate high-performance zinc phosphate electrode for energy storage applications. *Ceramics International*. 2024;50(2A):2742—2753.
https://doi.org/10.1016/j.ceramint.2023.10.336
20. Przywecka K., Grzmil B., Kowalczyk K., Sreńscek-Nazzal J. Studies on preparation of phosphate pigments for application in composite protective coatings. *Progress in Organic Coatings*. 2018;119:44—49.
https://doi.org/10.1016/j.porgcoat.2018.02.009
21. Gao H., Yang S., Mao D., Long M., Qu X. Significant zinc release from widely-used commercial lithopone pigments under solar irradiation. *Environmental Pollution*. 2022;292(A):118—131.
https://doi.org/10.1016/j.envpol.2021.118352
22. Kirpichnikov N.A., Bizhan S.P. The influence of long-term use of fertilizers during liming using zinc on the productivity of field crop rotation and the content of phosphates in soddy-podzolic soil. *Agrokhimicheskii vestnik*. 2021;(2):23—26. (In Russ.).
https://doi.org/10.24412/1029-2551-2021-2-004
Кирпичников Н.А., Бижан С.П. Влияние длительного применения удобрений при известковании с использованием цинка на продуктивность полевого севооборота и содержание фосфатов в дерново-подзолистой почве. *Агрохимический вестник*. 2021;(2):23—26.
https://doi.org/10.24412/1029-2551-2021-2-004
23. Javad S., Singh A., Kousar N., Arifeen F., Nawaz K., Azhar L. Chapter 13 — Zinc-based nanofertilizers: synthesis and toxicity assessments. In: *Nanofertilizer Synthesis*. 2024. P. 213—232.
https://doi.org/10.1016/B978-0-443-13535-4.00018-3
24. Bildinov I.K., Zabolotskikh A.V., Podsevalov P.V. Method for producing 1,2,3,4-tetrachlorohexafluorobutane: Patent 2246477 (RF). 2005. (In Russ.).
Бильдинов И.К., Заболотских А.В., Подсевалов П.В. Способ получения 1,2,3,4-тетрахлоргексафторбутана: Патент 2246477 (РФ). 2005.
25. Bildinov I.K., Zabolotskikh A.V., Podsevalov P.V. Method for producing hexafluorobutadiene: Patent 2272017 (RF). 2005. (In Russ.).
Бильдинов И.К., Заболотских А.В., Подсевалов П.В. Способ получения гексафторбутадиена: Патент 2272017 (РФ). 2005.
26. Malyshev O.R. Method for producing hexafluorobutadiene: Patent 2340588 (RF). 2008. (In Russ.).
Малышев О.Р. Способ получения гексафторбутадиена: Патент 2340588 (РФ). 2008.
27. Perevozchikov V.V., Podsevalov P.V. Method for producing hexafluorobutadiene: Patent 2359951 (RF). 2009. (In Russ.).
Перевозчиков В.В., Подсевалов П.В. Способ получения гексафторбутадиена: Патент 2359951 (РФ). 2009.
28. Takakhasi K., Okhhigasi Y., Iyota D. Method for producing hexafluorobutadiene: Patent 2754857 (RF). 2021. (In Russ.).
Такахаси К., Оххигаси Ю., Ийота Д. Способ получения гексафторбутадиена: Патент 2754857 (РФ). 2021.
29. Carson I., Love J.B., Morrison C.A., Tasker P.A., Moser M., Fischmann A.J., Jakovljevic B., Soderstrom M.D. Co-extraction of iron and sulfate by bis (2,4,4-trimethylpentyl) phosphinic acid, CYANEX® 272. *Solvent Extraction and Ion Exchange*. 2020;38(3):328—339.
https://doi.org/10.1080/07366299.2020.1720123

30. Pavón S., Haneklaus N., Meerbach K., Bertau M. Iron (III) removal and rare earth element recovery from a synthetic wet phosphoric acid solution using solvent extraction. *Minerals Engineering.* 2022;182:107569. https://doi.org/10.1016/j.mineng.2022.107569
31. Guimarães A.S., Silva M.F., Resende G.PS., Santos I.D., Mansur M.B. Solvent extraction of metals from a Brazilian nickel lateritic liquor with D2EHPA and Cyanex 272. *Brazilian Journal of Chemical Engineering.* 2023;40(2):599—606. https://doi.org/10.1007/s43153-022-00252-4
32. Tran T.T., Iqbal M., Lee M.S. Comparison of the extraction and stripping behavior of iron (III) from weak acidic solution between ionic liquids and commercial extractants. *Korean Journal of Metals and Materials.* 2019;57(12):787—794. https://doi.org/10.3365/KJMM.2019.57.12.787
33. Chukreev C.G., Dorozhko V.A., Afonin M.A. Mathematical model of extraction of $FeCl_3$ and HCl in the $FeCl_3$—HCl—H_2O—Undecan-1-ol system. *Zhurnal obshchei khimii.* 2022;92(1):155—164. (In Russ.). https://doi.org/10.31857/S0044460X22010176
Чукреев К.Г., Дорожко В.А., Афонин М.А. Математическая модель экстракции $FeCl_3$ и HCl в системе $FeCl_3$—HCl—H_2O—ундекан-1-ол. *Журнал общей химии.* 2022;92(1):155—164. https://doi.org/10.31857/S0044460X22010176
34. Liu W., Zhang J., Xu Z., Liang J., Zhu Z. Study on the extraction and separation of zinc, cobalt, and nickel using ionquest 801, Cyanex 272, and their mixtures. *Metals.* 2021;11(3):401—413. https://doi.org/10.3390/met11030401
35. Fedorova M.I., Zakhodyaeva Yu.A., Voshkin A.A. Interfacial distribution of Fe(III) and Zn(II) in chloride systems with Aliquat 336 in polypropylene glycol 425. *Teoreticheskie osnovy khimicheskoi tekhnologii.* 2020;54(3):304—308. (In Russ.). https://doi.org/10.31857/S0040357120030021
Федорова М.И., Заходяева Ю.А., Вошкин А.А. Межфазное распределение Fe(III) и Zn(II) в хлоридных системах с Aliquat 336 в полипропиленгликоле 425. *Теоретические основы химической технологии.* 2020;54(3):304—308. https://doi.org/10.31857/S0040357120030021
36. Tangalychev R.D., Berezin N.B., Mezhevich Zh.V., Buzov S.V., Kozmin M.D. Study of the extraction of Zn(II) compounds from aqueous two-phase systems by liquid-liquid extraction. *Butlerovskie soobshcheniya.* 2021;67(7):88—93. (In Russ.). https://doi.org/10.37952/ROI-jbc-01/21-67-7-88
Тангалычев Р.Д., Березин Н.Б., Межевич Ж.В., Бузов С.В., Козьмин М.Д. Исследование извлечения соединений Zn(II) из водных двухфазных систем методом жидкостной экстракции. *Бутлеровские сообщения.* 2021;67(7):88—93. https://doi.org/10.37952/ROI-jbc-01/21-67-7-88
37. Novikov Yu.V., Lastochkina K.O., Boldina Z.N. Methods for studying the water quality of reservoirs. Moscow: Medicine, 1990. 175 p. (In Russ.).
Новиков Ю.В., Ласточкина К.О., Болдина З.Н. Методы исследования качества воды водоемов. М.: Медицина, 1990. 175 с.
38. Shwarzenbach G., Flashka G. Complexometric titration. Moscow: Khimiya, 1970. 230 p. (In Russ.).
Шварценбах Г., Флашка Г. Комплексонометрическое титрование. М.: Химия, 1970. 230 с.
39. Karyakin Yu.V., Angelov I.I. Pure chemicals. Moscow: Khimiya, 1974. 408 p. (In Russ.).
Карякин Ю.В., Ангелов И.И. Чистые химические вещества. М.: Химия, 1974. 408 с.

Information about the authors

Vladimir A. Dorozhko – Engineer, World-Class Laboratory, St. Petersburg State Institute of Technology (SPbSIT).
https://orcid.org/0000-0003-2582-069X
E-mail: dorozhko.ti@gmail.com

Kirill G. Chukreev – Postgraduate Student of the Department of General Chemical Technology and Catalysis, SPbSIT.
https://orcid.org/0000-0001-7678-353X
E-mail: kirya.chukreev@mail.ru

Mikhail A. Afonin – Cand. Sci. (Chem.), Associate Professor of the Department of Technology of Rare Elements and Nanomaterials Based on them, SPbSIT.
https://orcid.org/0000-0001-7993-9528
E-mail: afonin18111956@yandex.ru

Информация об авторах

Владимир Александрович Дорожко – инженер лаборатории мирового уровня, Санкт-Петербургский государственный технологический институт (технический университет) (СПбГТИ(ТУ)).
https://orcid.org/0000-0003-2582-069X
E-mail: dorozhko.ti@gmail.com

Кирилл Георгиевич Чукреев – аспирант кафедры общей химической технологии и катализа, СПбГТИ(ТУ).
https://orcid.org/0000-0001-7678-353X
E-mail: kirya.chukreev@mail.ru

Михаил Александрович Афонин – к.х.н., доцент кафедры технологии редких элементов и наноматериалов на их основе, СПбГТИ(ТУ).
https://orcid.org/0000-0001-7993-9528
E-mail: afonin18111956@yandex.ru

Contribution of the authors

V.A. Dorozhko – determined the purpose of the study, developed the processing technology, and wrote the manuscript.

K.G. Chukreev – conducted laboratory research and participated in the discussion of the results.

M.A. Afonin – provided scientific consulting and participated in the discussion of the results.

Вклад авторов

В.А. Дорожко – определение цели работы, разработка технологии, написание текста статьи.

К.Г. Чукреев – лабораторные исследования, участие в обсуждении результатов.

М.А. Афонин – консультации по научной части работы, участие в обсуждении результатов.

The article was submitted 17.08.2024, revised 06.01.2025, accepted for publication 09.01.2025

Статья поступила в редакцию 17.08.2024, доработана 06.01.2025, подписана в печать 09.01.2025

UDC 621.365.2 : 669.2/8
https://doi.org/10.17073/0021-3438-2025-4-30-36

Research article
Научная статья

Thermodynamic premises of fire refining of blister copper considering the interaction parameters of the melt

S.I. Kholod[1,3], **V.P. Zhukov**[2], **S.V. Mamyachenkov**[3], **V.V. Rogachev**[3]

[1] **Technical University of the Ural Mining and Metallurgical Company**
3 Uspenskiy Prosp., Verkhnyaya Pyshma, Sverdlovsk Region 624091, Russia

[2] **JSC "Uralmekhanobr"**
87 Khokhryakova Str., Ekaterinburg 620063, Russia

[3] **Ural Federal University n.a. the First President of Russia B.N. Yeltsin**
19 Mira Str., Ekaterinburg 620002, Russia

✉ Sergey I. Kholod (hsi503@yandex.ru)

Abstract: The process of fire refining of copper is based on the removal of impurities that have a high affinity for oxygen through their oxidation by gaseous oxygen. Since the main component of blister copper is copper itself, according to the law of mass action and its affinity for oxygen, during air blowing the metal primarily reacts with the oxygen in the blast. The resulting copper (I) oxide is transported from the zone of direct contact with gaseous oxygen into the region of lower oxygen concentration, where the oxidation of impurities (Me_i) occurs. In practice, the actual copper melt deviates from ideal behavior; therefore, it is necessary to consider the activities of the components and the interaction parameters of the system when evaluating the thermodynamic premises of fire refining. It is known that the oxygen activity in copper melts depends on the oxygen affinity of the impurities. Impurities with a high affinity for oxygen (e.g., Al, Si, Mn) significantly reduce the oxygen activity, whereas those with a lower affinity (e.g., Zn, Fe, Sn, Co, Pb) only partially decrease it. Thermodynamic calculations were performed to estimate the final concentration of impurities in the copper melt and to theoretically evaluate the influence of impurities on oxygen activity in blister and anode copper. The calculations showed that fire refining of copper by air blowing under a weighted ideal slag has thermodynamic limitations. The final impurity concentration depends on both the oxygen activity in the melt and the activity of the impurity oxide in the slag. A decrease in the impurity oxide activity in the slag enhances refining efficiency by shifting the oxidation reaction equilibrium toward the reaction products. The theoretical effect of impurities on the oxygen activity in copper is substantiated for two melts differing in chemical compositin.

Keywords: oxidation, blister copper, anode copper, oxygen activity, activity coefficient, weighted ideal slag.

For citation: Kholod S.I., Zhukov V.P., Mamyachenkov S.V., Rogachev V.V. Thermodynamic premises of fire refining of blister copper considering the interaction parameters of the melt. *Izvestiya. Non-Ferrous Metallurgy*. 2025;31(4):30–36.
https://doi.org/10.17073/0021-3438-2025-4-30-36

Термодинамические предпосылки огневого рафинирования черновой меди с учетом параметров взаимодействия расплава

С.И. Холод[1,3], В.П. Жуков[2], С.В. Мамяченков[3], В.В. Рогачев[3]

[1] **Технический университет Уральской горно-металлургической компании**
Россия, 624091, Свердловская обл., г. Верхняя Пышма, Успенский пр-т, 3

[2] **АО «Уралмеханобр»**
Россия, 620063, г. Екатеринбург, ул. Хохрякова, 87

[3] **Уральский федеральный университет имени первого Президента России Б.Н. Ельцина**
Россия, 620002, г. Екатеринбург, ул. Мира, 19

✉ Сергей Иванович Холод (hsi503@yandex.ru)

Аннотация: В основе огневого рафинирования меди лежит процесс удаления примесей, обладающих повышенным сродством к кислороду, за счет их окисления кислородом газовой фазы. Поскольку основным компонентом черновой меди является медь, то, согласно закону действующих масс и сродства к кислороду, при продувке расплава воздухом она преимущественно вступает во взаимодействие с кислородом дутья. Образовавшийся оксид меди (I) в результате перемешивания потоками воздуха перемещается из зоны непосредственного контакта с газообразным кислородом в зону низких концентраций кислорода, в которой осуществляется протекание реакции окисления примесей (Me_i) [1]. На практике реальный расплав меди отличается от идеального, поэтому для оценки термодинамических предпосылок огневого рафинирования меди целесообразно учитывать активности компонентов и параметры взаимодействия системы. Известно, что активность кислорода в медных расплавах зависит от сродства примесей к кислороду. Примеси, обладающие высоким сродством к кислороду (например, Al, Si, Mn), достаточно хорошо снижают активность кислорода. Примеси, обладающие меньшим сродством к кислороду (например, Zn, Fe, Sn, Co, Pb), частично снижают его активность. Для оценки термодинамической возможности окисления примесей (Me_i) в расплаве меди, с учетом параметров взаимодействия расплава, проведены расчеты конечной концентрации примесей в расплаве меди и теоретическая оценка влияния примесей на активность кислорода в расплаве черновой и анодной меди. Расчеты показали, что возможность огневого рафинирования меди путем продувки расплава воздухом под средневзвешенным идеальным шлаком имеет термодинамические ограничения, при этом конечная концентрация примеси зависит от активности кислорода в расплаве и от активности оксида примеси в шлаке. С уменьшением активности оксида примеси в шлаке улучшается рафинирование за счет сдвига равновесия реакции окисления примеси в сторону продуктов взаимодействия. Теоретически обосновано влияние примесей на активность кислорода в меди для двух различных по химическому составу расплавов.

Ключевые слова: окисление, черновая медь, анодная медь, активность кислорода, коэффициент активности, средневзвешенный идеальный шлак.

Для цитирования: Холод С.И., Жуков В.П., Мамяченков С.В., Рогачев В.В. Термодинамические предпосылки огневого рафинирования черновой меди с учетом параметров взаимодействия расплава. *Известия вузов. Цветная металлургия*. 2025;31(4):30–36.
https://doi.org/10.17073/0021-3438-2025-4-30-36

Introduction

The fire refining technology of copper is based on the partial oxidation of the melt with free oxygen from the gas phase and the formation of oxides of impurities (Me_xO_y) that are only partially soluble in liquid copper. These oxides, due to their lower density, form a slag layer on the surface of the melt. The oxidation reactions of copper and impurities occur in a system consisting of a liquid phase of impurity solution, condensed oxide phases, and the gas phase of volatile compounds. The oxygen content during the oxidation stage is between 0.4—0.8 %, which ensures the transfer of copper (I) oxide (Cu_2O) into the liquid copper and facilitates the oxidation of impurities (Me_i). The actual copper melt deviates from the ideal, and thus it is appropriate to consider the thermodynamic aspects of the process, including the activities of the components and the system's interaction parameters, when evaluating the potential technological possibilities of fire refining.

Problem statement

It is known that fire refining of copper is carried out by blowing the melt with air at temperatures ranging from 1150 to 1170 °C. According to the law of mass action, due to the high concentration of copper in the melt, the oxidation reaction of copper predominates:

$$4[Cu] + \{O_2\} = 2(Cu_2O). \quad (1)$$

The formed copper (I) oxide moves from the zone of direct contact with gaseous oxygen into the depth of the melt, where the oxygen concentration is low, and the direction of reaction (1) changes to the opposite, with Cu_2O dissolving in the copper melt, thereby increasing the oxygen concentration:

$$(Cu_2O) = 2[Cu] + [O], \quad (2)$$

This facilitates the direct oxidation of impurities with dissolved oxygen:

$$[Me] + [O] = (MeO). \quad (3)$$

Additionally, Cu_2O acts as a condensed oxidant for impurities according to the reaction:

$$[Me] + (Cu_2O) = (MeO) + 2[Cu]. \quad (4)$$

According to the Cu—Cu_2O phase diagram, the solubility of Cu_2O in copper increases with temperature. At temperatures above 1200 °C, copper (I) oxide transitions into the slag, while copper (II) oxide (CuO) does not form due to the dissociation pressure exceeding the partial oxygen pressure in the air.

Thus, the primary condition for fire refining of copper is maintaining the oxygen concentration in copper higher than the equilibrium concentration for impurity oxidation reactions [2—18].

It is known that the potential for oxidation and removal of impurities under primary slag is determined by the Gibbs free energy of the oxidation reactions [1]. The reduction of the Gibbs free energy for the main oxidation reactions of impurities indicates the degree to which their affinity for oxygen changes, their ability to oxidize, and their removal from the melt.

To prevent over-oxidation of copper and its conversion into copper (I) oxide in the slag, it is necessary to limit the oxygen saturation of the copper melt to 12 % Cu_2O.

Assuming that the metallic and oxide phases in reaction (3) are in equilibrium, the following expression holds for each impurity present in these phases:

$$x[Me] + y[O] = (Me_xO_y). \quad (5)$$

Considering the deviation of the properties of the real copper solution from the ideal, the equilibrium constant for reaction (5) is determined by the formula:

$$K_{Me} = \frac{a_{(Me_xO_y)}}{a^x_{[Me]}\, a^y_{[O]}} = \frac{N_{(Me_xO_y)}\gamma_{(Me_xO_y)}}{[Me]^x [O]^y \gamma^x_{Me}\, \gamma^y_O}, \quad (6)$$

where $N_{(Me_xO_y)}$ is the molar fraction of the impurity oxide in the slag; $[Me]^x$ and $[O]^y$ represent the molar fractions of the impurity and oxygen in the melt, respectively; $\gamma_{(Me_xO_y)}$ is the activity coefficient for the impurity in the slag; γ^x_{Me} and γ^y_O are the activity coefficients for the impurity and oxygen in the melt.

Based on the reduction of the Gibbs free energy for the main oxidation reactions of the impurities and its relationship with the equilibrium constant

$$\Delta G^0 = -RT \ln K_{Me} \quad (7)$$

the final concentration of the impurity in the copper melt (mole fraction) can be estimated by converting equation (6) as follows [3]:

$$[Me]^x = \frac{N_{(Me_xO_y)}\gamma_{(Me_xO_y)}}{K_{Me}[O]^y \gamma^x_{Me}\, \gamma^y_O}. \quad (8)$$

It is known that the oxygen activity in copper melts depends on the impurity's affinity for oxygen. Impurities with a high affinity for oxygen (e.g., Al, Si, Mn) significantly reduce the oxygen activity, while impurities with a lower affinity (e.g., Zn, Fe, Sn, Co, Pb) only partially reduce it.

Copper melt with low impurity concentrations is considered diluted. In this case, a 1 % ideal diluted solution of the *i*-th impurity in copper is assumed to be the standard state. The oxygen activity in the copper melt with *n* impurities is described by the following expression:

$$\lg(a_{[O]}) = \lg[\%\,O] + \sum_{j=1}^{n} e^j_{[O]}[\%\,j], \quad (9)$$

where $e^j_{[O]}$ is the interaction parameter between oxygen and the *j*-th impurity of the first order.

The objective of this work is to evaluate the thermodynamic feasibility of oxidizing impurities (Me_i) in copper melt, considering the interaction parameters of the melt, and to theoretically assess the impact of impurities on the oxygen activity in the copper melt.

Methodology

To evaluate the thermodynamic feasibility of oxidizing impurities (Me_i) in copper melt, considering the interaction parameters of the melt, calculations were

performed to estimate the final impurity concentration in copper at a temperature of 1150 °C, characteristic for the oxidation stage of refining. The following steps were taken:

The real weighted composition of blister copper was used as input data (wt. %):

Cu	98.86	S	0.16
Ag	0.076	Pb	0.0658
Sb	0.147	Zn	0.041
As	0.128	Sn	0.058
Ni	0.2	Fe	0.047
Bi	0.0012		

It is known from the practice of fire refining that the oxygen concentration in the melt is maintained at an elevated level due to continuous blowing of air into the melt, which fluctuates between 0.4 and 0.8 wt. %.

At the initial stage of oxidation, a substantial amount of oxygen is introduced into the melt, so an average oxygen concentration of 0.6 wt. % was assumed.

The oxidation process of impurities is determined by their affinity for oxygen; therefore, the composition of the slag phase changes during smelting proportionally to the oxidation rate of the *i*-th impurity. Accordingly, to evaluate the thermodynamic feasibility of impurity oxidation, a weighted ideal slag composition was selected, wt. %: ~70 Cu_2O, 29 SiO_2, ~1 Me_xO_y, under the assumption that the activity of the impurity oxide in the slag equals its molar fraction:

$$a_{Me_xO_y} = N_{Me_xO_y}. \quad (10)$$

The equilibrium constant and Gibbs free energy for the oxidation reaction of the *i*-th impurity (5) were calculated using the thermodynamic software package HSC Chemistry 9.

To determine the final impurity concentration from equation (8), the molar fraction of the *i*-th impurity oxide was calculated based on the condition of the weighted ideal slag composition.

Since the activity coefficient of the *i*-th impurity is affected by all components of the melt, the activity coefficients of the impurity and oxygen in the melt were calculated using the following formulas [19—25]:

$$\ln\gamma_{[Me]} = \ln\gamma^{\infty}_{[Me]} + N_{[Me]}\varepsilon^{Me}_{[Me]} + \sum_{j=1}^{n} N_{[j]}\varepsilon^{j}_{[Me]}, \quad (11)$$

$$\ln\gamma_{[O]} = \ln\gamma^{\infty}_{[O]} + N_{[O]}\varepsilon^{O}_{[O]} + \sum_{j=1}^{n} N_{[O]}\varepsilon^{j}_{[O]}, \quad (12)$$

where $\gamma^{\infty}_{[Me]}$, $\gamma^{\infty}_{[O]}$ are the activity coefficients of the impurity and oxygen in an infinitely dilute copper solution; $\varepsilon^{Me}_{[Me]}$, $\varepsilon^{j}_{[Me]}$, $\varepsilon^{O}_{[O]}$, $\varepsilon^{j}_{[O]}$ are the interaction parameters between identical and dissimilar components of the melt.

The interaction parameters of the *i*-th impurity and oxygen ($\varepsilon^{O}_{[Me]}$ and $\varepsilon^{Me}_{[O]}$) in the temperature range 1100—1200 °C for the Cu—Me_i—O system are given below [1]:

Ag	−0.2	Pb	−6.15
Sb	−1.3962	Zn	−2.52
As	3.3	Sn	−0.35
Ni	−5.9625	Fe	−239.92
Bi	−2.408	O	−7.7
S	−0.081		

At t = 1150 °C, the maximum oxygen solubility in liquid copper is 3.01 at. % (0.79 wt. %):

$$\lg[\%O]_{max} = -\frac{9260}{t} + 7.15. \quad (13)$$

To calculate the final impurity concentration, the chemical compositions of blister copper (see data above) and the ideal slag were expressed in molar fractions. The activity coefficients of the components were calculated using equations (11) and (12). Based on these assumptions, and using equation (8), the following final impurity concentrations were obtained (converted to wt. %):

Sb	0.08	Pb	0.09
As	0.27	Zn	0.0009
Ni	0.11	Sn	0.0087
Bi	0.0043	Fe	0.0068

The calculated results were compared with practical data for anode copper, which has the following chemical composition (wt. %):

Sb	0.14	Pb	0.13
As	0.11	Zn	0.003
Ni	0.17	Sn	0.0052
Bi	0.0011	Fe	0.0012

To theoretically evaluate the influence of impurities on the oxygen activity in the melt, data on the chemical composition of blister and anode copper, as well as the assumptions used in the thermodynamic assessment of impurity oxidation (Me_i), were applied. The evaluation of impurity influence was carried out in the following sequence:

The molar interaction parameters (see above) were recalculated to mass-based parameters using the equation:

$$e_i^j = \frac{1}{100}\frac{1}{\ln 10}\left(\frac{A_{r\mathrm{Me}}}{A_{ri}}\varepsilon_i^j + \frac{A_{ri} - A_{r\mathrm{Me}}}{A_{ri}}\right), \qquad (14)$$

where $A_{r\mathrm{Me}}$ is the atomic mass of copper (g/mol); A_{ri} is the atomic mass of the i-th impurity (g/mol); ε_j^i is the molar interaction parameter.

Mass-based interaction parameters in the Cu—Me_i—O system:

Ag 0,00125	S..... −0,226
Sb..... 0,000083	Pb..... −0,00544
As..... 0,0129	Zn ..... −0,01
Ni..... −0,0257	Sn..... −0,001162
Bi 0,000075	Fe..... −0,58

An average oxygen concentration in the melt of 0.6 wt. % was assumed.

Using expression (9), the oxygen activity in the copper melt was calculated. For blister copper, the oxygen activity was $a_{[O]}$ = 0.515 %, and for anode copper — $a_{[O]}$ = 0.59 %.

Results

The calculation results, ordered by the impurity values, show good convergence with the practice of fire refining of copper. The residual concentration of impurities in copper decreases with an increase in their affinity for oxygen, a reduction in the impurity oxide activity in the slag, and an increase in the oxygen activity in the copper melt. The calculations of the residual concentration of impurities such as As, Sb, Pb, and Ni showed values that differed from the practical data of anode copper. This discrepancy is explained by the following: first, the oxidation of copper during refining does not reach the saturation limits, so the copper oxide activity in the slag is not equal to 1; second, the activity of impurities in the slag is much lower than that of the pure impurity in the melt; finally, impurity solutions in metals are not ideal. Overall, the calculations indicate that the maximum impurity content in copper melt depends on the refining temperature, the oxygen saturation of the melt, and the slag phase composition.

The calculation of oxygen activity in copper for two melts with different chemical compositions revealed a significant difference in the extent to which impurity concentrations affect it. Overall, impurities reduced the oxygen activity in the blister copper melt by 14.2 %. This indicates that, at such impurity concentrations, they do not have a major impact on the physicochemical properties of the melt; however, they do considerably decrease the activity of dissolved oxygen. In anode copper, the reduction in oxygen activity was 1.6 %.

Analysis of the chemical compositions of blister and anode copper presented above shows that impurities with a higher affinity for oxygen exert a greater influence on oxygen activity. Theoretical calculations of the effect of impurities on oxygen concentration in copper melt should be taken into account at the stage of impurity oxidation, particularly at its initial stage, in order to optimize the air-blowing rate.

Conclusion

Considering the activity coefficients of impurities and the selected weighted ideal slag composition, the thermodynamic possibilities of oxidizing impurities (Me_i) in copper melt were assessed by calculating the final impurity concentrations at a temperature of 1150°C, characteristic for the oxidation stage of refining. It was shown that fire refining of copper by blowing the melt with air under a weighted ideal slag has thermodynamic limitations, with the final impurity concentration depending on the oxygen activity in the melt and the impurity oxide activity in the slag. As the impurity oxide activity in the slag decreases, the refining process improves due to the shift in the equilibrium of the oxidation reaction towards the interaction products.

The theoretical assessment of the impact of impurities on the oxygen activity in copper for two melts with different chemical compositions was also justified.

References

1. Zhukov V.P., Skopov G.V., Kholod S.I., Bulatov K.V. Pyrometallurgy of copper. Moscow: IP Ar Media, 2023. Book 2. 324 p. (In Russ.).
   Жуков В.П., Скопов Г.В., Холод С.И., Булатов К.В. Пирометаллургия меди. М.: Ай Пи Ар Медиа, 2023. Кн. 2. 324 с.
2. Davenport W.G., King M., Schlesinger M., Biswas A.K. Extractive metallurgy of copper. 4th ed. Oxford: Elsever Sci. Ltd., 2002. 432 p.
3. Kozhanov V.A., Savenkov Yu.D., Shpakovsky V.A., Shutov I.V. Thermodynamic prerequisites for precision fire refining of copper from scrap and waste. In: *Scientific works of Donetsk National Technical University.* Donetsk: DNTU, 2012. P. 494–499. https://uas.su/conferences/2010/50let/55/00055.php,30.04.2025
   Кожанов В.А., Савенков Ю.Д., Шпаковский В.А., Шутов И.В Термодинамические предпосылки

прецизионного огневого рафинирования меди из лома и отходов. В сб.: *Научные труды Донецкого национального технического университета*. Донецк: ДНТУ, 2012. С. 494—499. https://uas.su/conferences/2010/50let/55/00055.php,30.04.2025

4. Biswas A.K., Davenport W.G. Extractive metallurgy of copper. Oxford: Pergamon Press., 1996.
5. Gerlach J., Herfort P. The rate of oxyden uptake by molten copper. *Metall.* 1968;22(11):1068—1090.
6. Gerlach J., Schneider N., Wuth W. Oxyden absorption during blowing of molten Cu. *Metall.* 1972;25(11):1246—1251.
7. Frohne O., Rottmann G., Wuth W. Processing speeds in the pyrometallurgical refining of Cu by the top-blowing process. *Metall*. 1973;27(11):1112—1117.
8. Zhukov V.P., Mastyugin S.A., Khydyakov I.F. Absorption of oxyden by molten copper during top blowing with steam — air mixtures. *Soviet Journal of Non-Ferrous Metals.* 1986;14(5):371—375
9. Aglitsky V.A. Copper refining. Moscow: Metallurgiya, 1971. 184 p. (In Russ.).
   Аглицкий В.А. Рафинирование меди. М.: Металлургия, 1971. 184 с.
10. Safarov D.D. Kinetics of oxidation of copper-based alloys by a gas phase of variable composition: Diss. Cand. Sci. (Chem.). Sverdlovsk: IMET UrO RAS, 1983. (In Russ.).
    Сафаров Д.Д. Кинетика окисления сплавов на основе меди газовой фазой переменного состава: Дис. ... канд. хим. наук. Свердловск: ИМЕТ УрО РАН, 1983.
11. Belousov A.A., Pastukhov E.A., Aleshina S.N. Effect of temperature, partial pressure of oxygen on the kinetics of oxidation of liquid copper. *Melts.* 2003;(2):3—6. (In Russ.).
    Белоусов А.А., Пастухов Е.А., Алешина С.Н. Влияние температуры, парциального давления кислорода на кинетику окисления жидкой меди. *Расплавы.* 2003;(2):3—6.
12. Martin T., Utigard T. The kinetigs and mechanism of molten copper oxidation by top blowing of oxygen. *Journal of Metals*. 2005;(2):58—62.
13. Belousov V.V., Klimashin A.A. High-temperature oxidation of copper. *Uspekhii Khimii.* 2013;(3):3—6. (In Russ.).
    Белоусов В.В., Климашин А.А. Высокотемпературное окисление меди. *Успехи химии*. 2013;(3):3—6.
14. Barton R.G., Brimacombe J.K. Influence of surface tension-driven flow of the kinetics of oxygen absorption in molten copper. *Metallurgical Transactions B*. 1977;8:417—427.
15. Lyamkin S.A., Tanutrov I.N., Sviridova M.N. Kinetics of oxidation of molten copper by gas phase oxygen. *Melts.* 2013;(2):83—89. (In Russ.).
    Лямкин С.А., Танутров И.Н., Свиридова М.Н. Кинетика окисления расплавленной меди кислородом газовой фазы. *Расплавы*. 2013;(2):83—89.
16. Avetisyan A.A., Chatilyan A.A., Kharatyan S.L. Kinetic features of the initial stages of high-temperature oxidation of copper. *Chemical Journal of Armenia*. 2013;66(3):407—415. (In Russ.).
    Аветисян А.А., Чатилян А.А., Харатян С.Л. Кинетические особенности начальных стадий высокотемпературного окисления меди. *Химический журнал Армении.* 2013;66(3):407—415.
17. Kumar H., Kumagai S., Kameda T., Saito Y., Takahashi K., Hayashi H., Yoshioka T. Highly efficient recovery of high-purity Cu, PVC, and phthalate plasticizer from waste wire harnesses through PVC swelling and rod milling. *Reaction Chemistry & Engineering.* 2020;5(9):1805—1813. https://doi.org/10.1039/D0RE00303D
18. Lee B.J. Revision of thermodynamic description of Fe—Cr and Fe—Ni liquid phases. *Calphad*. 1993;17(3):251—268.
    https://doi.org/10.1016/0364-5916(93)90004-u
19. Kubaschewski O., Geider K.H., Hack K. The thermochemical properties of iron-nickel alloys. *Zeitschrift für Metallkunde*. 1977;68(5):337—341.
20. Conard B.R., McAneney T.B., Sridhar R. Thermodynamics of iron-nickel alloys by mass-spectrometry. *Metallurgical and Materials Transactions*. 1978;9:463—468.
21. Fernandez Guillermet A. Assesment of the thermodynamic properties of the Ni—Co system. *Zeitschrift für Metallkunde*. 1987;78(9):639—640.
22. Jakob K.T., Fitzner K. This estimation of the thermodynamic properties of ternary alloys from binary data using the shortest distance composition path. *Thermochim. Acta.* 1977;18(2):197—206.
    https://doi.org/10.1016/0040-6031(77)80019-1
23. Fujita Y., Pagador R.U., Hino M., Azakami T. Thermodynamic investigation on molten Cu—Ni—Fe alloys by the double knudsen cell-mass spectrometer system. *Journal of the Japan Institute of Metals and Materials.* 1997;61(7):619—624.
    https://doi.org/10.2320/jinstmet1952.61.7_619
24. Tomiska J.Z. Ternary thermodynamics by computer-aided Knudsen cell mass spectrometry: Fee solid Fe—Ni—Co alloys. *Zeitschrift für Metallkunde.* 2004;95(3):136—141. https://doi.org/10.3139/146.017926
25. Tsymbulov L.B., Kolosova E.Yu., Tsemekhman L.Sh. Determination of the activities of components in metal melts containing Cu, Ni, Co, Fe, using calculation methods. *Non-Ferrous Metals*. 2011;(3):28—36. (In Russ.).
    Цымбулов Л.Б., Колосова Е.Ю., Цемехман Л.Ш. Определение активностей компонентов в металлических расплавах, содержащих Cu, Ni, Co, Fe, с применением расчетных методов. *Цветные металлы.* 2011;(3):28—36.

Information about the authors

Sergey I. Kholod – Leading Engineer, Department of foundry and hardening technologies, Ural Federal University n.a. the First President of Russia B.N. Yeltsin (UrFU); Deputy Head of the Department of metallurgy, Technical University of the Ural Mining and Metallurgical Company.
E-mail: hsi503@yandex.ru

Vladimir P. Zhukov – Dr. Sci. (Eng.), Professor, Leading Researcher, JSC "Uralmekhanobr".
E-mail: zhukov_vp@umbr.ru

Sergey V. Mamyachenkov – Dr. Sci. (Eng.), Professor, Head of the Department of non-ferrous metallurgy, UrFU.
https://orcid.org/0000-0002-4458-3792
E-mail: s.v.mamiachenkov@urfu.ru

Vladimir V. Rogachev – Cand. Sci. (Eng.), Associate Professor, Department of metallurgy of iron and alloys, UrFU.
E-mail: v.v.rogachev@urfu.ru

Информация об авторах

Сергей Иванович Холод – вед. инженер кафедры литейного производства и упрочняющих технологий Уральского федерального университета имени первого Президента России Б.Н. Ельцина (УрФУ); зам. заведующего кафедрой металлургии Технического университета Уральской горно-металлургической компании.
E-mail: hsi503@yandex.ru

Владимир Петрович Жуков – д.т.н., профессор, вед. науч. сотрудник, АО «Уралмеханобр»

E-mail: zhukov_vp@umbr.ru

Сергей Владимирович Мамяченков – д.т.н., профессор, зав. кафедрой металлургии цветных металлов УрФУ.
https://orcid.org/0000-0002-4458-3792
E-mail: s.v.mamiachenkov@urfu.ru

Владимир Васильевич Рогачев – к.т.н., доцент кафедры металлургии железа и сплавов УрФУ.
E-mail: v.v.rogachev@urfu.ru

Contribution of the authors

V.P. Zhukov – defining the study aim, participating in the discussion of the results.

S.I. Kholod – performing calculations, writing the manuscript, participating in the discussion of the results.

S.V. Mamyachenkov – writing the manuscript, participating in the discussion of the results.

V.V. Rogachev – performing calculations, participating in the discussion of the results.

Вклад авторов

В.П. Жуков – определение цели работы, участие в обсуждении результатов.

С.И. Холод – проведение расчетов, написание статьи, участие в обсуждении результатов.

С.В. Мамяченков – написание статьи, участие в обсуждении результатов.

В.В. Рогачев – проведение расчетов, участие в обсуждении результатов.

The article was submitted 05.05.2025, revised 15.05.2025, accepted for publication 19.05.2025

Статья поступила в редакцию 05.05.2025, доработана 15.05.2025, подписана в печать 19.05.2025

UDC 621.771.8
https://doi.org/10.17073/0021-3438-2025-4-37-49

Research article
Научная статья

Finite element modeling and analysis of the technological feasibility of a new cladding scheme for aluminum-lithium alloy 1441 ingots

A.M. Pesin[1], **A.V. Razinkin**[2], **V.A. Zamaraev**[2], **D.O. Pustovoitov**[1]

[1] **Nosov Magnitogorsk State Technical University**
38 Lenin Ave., Magnitogorsk, Chelyabinsk Region 455000, Russia

[2] **PJSC "Kamensk-Uralsky Metallurgical Plant"**
5 Zavodskaya Str., Kamensk-Uralsky, Sverdlovsk Region 623405, Russia

✉ Denis O. Pustovoitov (pustovoitov_den@mail.ru)

Abstract: Using the QForm software package, a finite-element analysis was conducted to assess the technological feasibility of implementing a new cladding scheme for 360-mm-thick aluminum–lithium alloy 1441 ingots under the production conditions of PJSC "KUMP". Instead of the traditional cladding scheme, in which the cladding plates are roll-bonded to the ingot over four passes with an absolute reduction of 6 mm per pass, the cladding plates are seated in pre-machined recesses milled into the top and bottom surfaces of the ingot and roll-bonded in a single pass with an absolute reduction of 24 mm. The analysis showed that the new cladding scheme prevents extrusion of the cladding plates from the ingot surface at high reductions, enabling the use of thinner plates (10 mm instead of the conventional 15 mm). The new approach also significantly reduces the total number of passes and inter-deformation pauses during rough rolling, thereby improving the thermal condition of the workpiece before finish rolling. A reduction of three passes and three pauses (10 s each) leads to an average temperature increase of approximately 23 °C. The deformation behavior of the base metal (alloy 1441) and the cladding layer (ACpl alloy) was analyzed. The mean accumulated strain in the ingot after rolling according to the new scheme was found to be twice as high as under the traditional scheme, while the deformation distribution within the cladding layer was more uniform. The obtained results can be used to enhance and optimize hot-rolling parameters for clad sheets and strips of aluminum–lithium alloy 1441 at PJSC "KUMP".

Keywords: aluminum-lithium alloy 1441, hot rolling, cladding, deformation state, finite-element modeling, stress-strain state, temperature.

Acknowledgements: The research was supported by the Russian Science Foundation (Grant No. 23-79-30015) and co-funded under Agreement No. KK0987F-2023.

For citation: Pesin A.M., Razinkin A.V., Zamaraev V.A., Pustovoitov D.O. Finite element modeling and analysis of the technological feasibility of a new cladding scheme for aluminum-lithium alloy 1441 ingots. *Izvestiya. Non-Ferrous Metallurgy.* 2025;31(4):37–49.
https://doi.org/10.17073/0021-3438-2025-4-37-49

Конечно-элементное моделирование и анализ технологической возможности применения новой схемы плакирования слитков из алюминий-литиевого сплава 1441

А.М. Песин[1], **А.В. Разинкин**[2], **В.А. Замараев**[2], **Д.О. Пустовойтов**[1]

[1] **Магнитогорский государственный технический университет им. Г.И. Носова**
Россия, 455000, Челябинская обл., г. Магнитогорск, пр-т Ленина, 38

[2] **ПАО «Каменск-Уральский металлургический завод»**
Россия, 623405, Свердловская обл., г. Каменск-Уральский, ул. Заводская, 5

✉ Денис Олегович Пустовойтов (pustovoitov_den@mail.ru)

Аннотация: С использованием программы «QForm» проведен конечно-элементный анализ технологической возможности применения новой схемы плакирования слитков толщиной 360 мм из алюминий-литиевого сплава 1441 в условиях ПАО «КУМЗ». Взамен традиционной схемы плакирования, предусматривающей приварку планшетов к слитку за 4 прохода с абсолютными обжатиями по 6 мм, предложено укладывать планшеты в специальные углубления, предварительно выполненные фрезерованием на верхней и нижней поверхностях слитка, а приварку осуществлять за 1 проход с абсолютным обжатием 24 мм. Показано, что новая схема плакирования позволяет предотвратить выдавливание планшетов с поверхности слитка при высоких абсолютных обжатиях. Это дает возможность использовать более тонкие планшеты (толщиной 10 мм) взамен традиционных (15 мм). Установлено, что по новой схеме плакирования существенно сокращается общее количество проходов и междеформационных пауз при черновой прокатке и за счет этого улучшается тепловое состояние раската перед чистовой прокаткой. При сокращении 3 проходов и 3 междеформационных пауз среднее повышение температуры составляет ≈23 °С. Исследовано деформированное состояние основного металла (сплав 1441) и плакирующего слоя (сплав АЦпл). Показано, что средняя накопленная деформация в слитке (математическое ожидание) после прокатки по новой схеме в 2 раза выше в сравнении с традиционной схемой. При этом характер деформации плакирующего слоя при прокатке по новой схеме более равномерный. Результаты могут быть использованы для совершенствования и оптимизации технологических режимов горячей прокатки плакированных листов и полос из алюминий-литиевого сплава 1441 в условиях ПАО «КУМЗ».

Ключевые слова: алюминий-литиевый сплав 1441, горячая прокатка, плакирование, режимы деформации, моделирование методом конечных элементов, напряженно-деформированное состояние, температура.

Благодарности: Исследования выполнены за счет гранта Российского научного фонда (соглашение № 23-79-30015) и в рамках договора о софинансировании № KK0987F-2023.

Для цитирования: Песин А.М., Разинкин А.В., Замараев В.А., Пустовойтов Д.О. Конечно-элементное моделирование и анализ технологической возможности применения новой схемы плакирования слитков из алюминий-литиевого сплава 1441. *Известия вузов. Цветная металлургия.* 2025;31(4):37–49. https://doi.org/10.17073/0021-3438-2025-4-37-49

Introduction

Compared with conventional aluminum alloys such as D16 (AA2024 analogue), aluminum—lithium alloys possess a unique combination of properties, including lower density, higher stiffness, superior strength and fatigue resistance, as well as good corrosion resistance and satisfactory weldability [1—7]. The full technological cycle for manufacturing sheets and strips from aluminum—lithium alloys has been developed and industrially implemented at the Kamensk-Uralsky Metallurgical Plant Joint Stock Company (KUMZ JSC), which remains the only producer and supplier of these alloys in Russia. Aluminum—lithium alloy 1441 of the Al—Cu—Mg—Li system belongs to the second generation of Al—Li alloys; its production at KUMZ JSC began in 1990 [8]. This structural alloy is widely used in aircraft and spacecraft manufacturing [9—13].

Cladding is a distinct hot-rolling operation intended to cover ingots of aluminum alloys with a thin layer of pure aluminum (≥ 99.3 %) or the ACpl alloy to ensure additional corrosion protection [14, 15]. In the case of aluminum—lithium alloys, cladding also significantly

increases the product yield by improving edge and surface quality of sheets and strips [16].

Three main cladding types are distinguished [17]:

— technological cladding (B), aimed at creating more favorable deformation conditions during rolling of low-ductility alloys (cladding-layer thickness not exceeding 1.5 % of sheet thickness);

— normal cladding (A), providing corrosion protection (cladding-layer thickness of at least 2 % for sheets thicker than 1.9 mm, and at least 4 % for thinner sheets);

— thickened cladding (U), ensuring enhanced corrosion protection (layer thickness of at least 4 % for sheets thicker than 1.9 mm, and 8 % or more for thinner sheets).

For the production of clad sheets and strips from aluminum—lithium alloy 1441, flat ingots with cross-sections of 225×950 mm, 275×1100 mm, 300×1100 mm, 390×1360 mm are used [8]. Before rolling, both the ingot (base-metal blank) and the cladding plates (blanks of cladding metal) undergo special preparation. To remove casting defects and ensure high-quality two-sided (top and bottom) roll-bonding of the plates, the wide faces of the ingots are milled by 5—15 mm per side [17]. The mating surfaces of the ingot and plates are then degreased. The plate thickness (h_{pl}) s calculated from the ingot thickness (H_{ing}) and the required cladding-layer thickness [17]:

$$h_{pl} = H_{ing}\delta/100a + 2\delta, \quad (1)$$

where $a = 0.8$ is a coefficient accounting for the difference in deformation of the ingot and the plates in the first passes, and δ is the upper limit of cladding-layer thickness specified in the relevant standards.

Before hot rolling, the aluminum—lithium 1441 ingots with the attached cladding plates are heated to no more than 460 °C. Roll-bonding of the plates is carried out during the first four passes with an absolute reduction per pass not exceeding 6 mm in cylindrical rolls, without applying a lubricant—coolant mixture (LCM). The LCM is intentionally excluded during these first passes to prevent its penetration under the plates and the formation of sub-plate blisters. In subsequent roughing and finishing passes, rolling is performed with the application of a water—oil emulsion containing 1—2.5 % rolling oil.

According to [4], the recommended temperature range for hot rolling of aluminum—lithium alloy 1441 is 460—390 °C. However, under industrial conditions the actual range is 460—340 °C for rough rolling and 340—300 °C (or even lower) for finish rolling. The temperature drop results from heat losses during a large number of roughing passes (up to 19) and the corresponding inter-pass delays, when the workpiece cools in air. Intensifying deformation during rough rolling is limited by the roll-bonding stage, at which the absolute reduction per pass must not exceed 6 mm (≈ 1.5 % relative reduction); otherwise, extrusion of the plate material from the ingot surface occurs.

Numerous studies [18—27] have been devoted to improving the cladding process for aluminum alloys during hot rolling; nevertheless, the issue of increasing the efficiency of plate bonding to the ingot remains unresolved.

The aim of the present work is to perform finite-element modeling and analyze the technological feasibility of applying a new cladding scheme for aluminum—lithium 1441 ingots in order to reduce the number of passes and inter-pass pauses during rough rolling.

Materials and methods

Finite element modeling and analysis of the co-rolling process of the ingot (base-metal blank) with two cladding plates (blanks of cladding metal) placed on the top and bottom surfaces were carried out using the QForm 11.0.1 software package in a two-dimensional plane-strain formulation (license No. R0-U2497-170719U197, licensee — Nosov Magnitogorsk State Technical University). The ingot material was aluminum—lithium alloy 1441 (Al—1.7 Cu—0.8 Mg—1.8 Li). The initial state corresponded to the condition after single-stage homogenization annealing at 450 °C for 8 h.

Experimental data on the flow stress of alloy 1441 were obtained from hot torsion tests on a Gleeble 3800 thermomechanical simulator equipped with a Torsion module. Cylindrical specimens of total length 165 mm and diameter 14 mm were used, with a working zone length $L = 20$ mm and radius $R = 5$ mm. One specimen end was rigidly fixed, while a torque was applied to the other (rotating) end. Tests were conducted at 450, 400, 350, 300, and 250 °C with strain rates of 0.01, 1, 10, and 50 s^{-1}. The flow-stress curves of alloy 1441, described by the relationship

$$\sigma_s = f(\bar{\varepsilon}, \dot{\varepsilon}, t), \quad (2)$$

where $\bar{\varepsilon}$ is the equivalent strain; $\dot{\varepsilon}$ is the strain rate (s^{-1}); t is the temperature (°C), were approximated by a tabulated function.

The cladding layer material was aluminum alloy ACpl (97.8 %), with a chemical composition in accor-

dance with GOST 4784-2019. As an example, Fig. 1 presents the flow-stress curves of aluminum—lithium alloy 1441 and the ACpl alloy at a strain rate of 10 s^{-1} and various temperatures.

The simulation was performed under the operating conditions of the Quarto 4600 roughing mill stand of the hot-rolling facility at KUMZ JSC. According to the traditional process, roll-bonding of the cladding plates is carried out during the first four passes according to a cross-rolling scheme, where the length of the ingot becomes its width after edge-turning (rotation by 90°). Therefore, for the two-dimensional finite element model, the following initial dimensions of the ingot after milling were adopted: 360×1360 mm (thickness × length). The ingot had a rectangular shape without chamfers or corner rounding. The initial dimensions of the cladding plates were 15×1100 mm (thickness × length). The total dimensions of the ingot with the top and bottom plates placed on it were 390×1360 mm (thickness × length). Hot rolling was simulated in working rolls of 1150 mm diameter. The ingot with the plates was heated to 450 °C in a furnace. The transfer time from the heating furnace to the rolling stand was empirically taken as 8 min. The rolling speed in each roughing pass was assumed to be 1 m/s, and the inter-pass pause was 10 s.

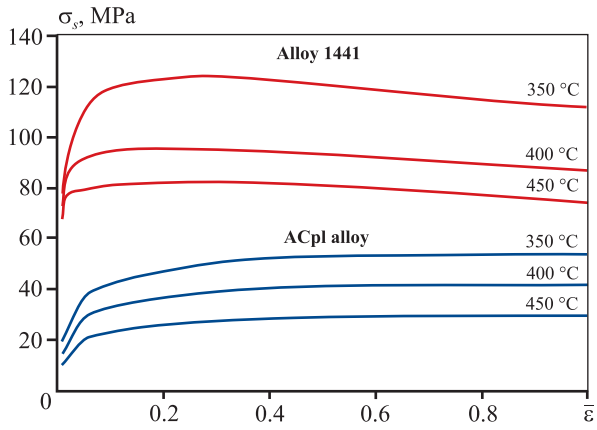

Fig. 1. Flow-stress curves of aluminum—lithium alloy 1441 and ACpl alloy at a strain rate of 10 s^{-1} and different temperatures

Рис. 1. Кривые сопротивления деформации алюминий-литиевого сплава 1441 и алюминиевого сплава АЦпл при скорости деформации 10 $с^{-1}$ и различных температурах

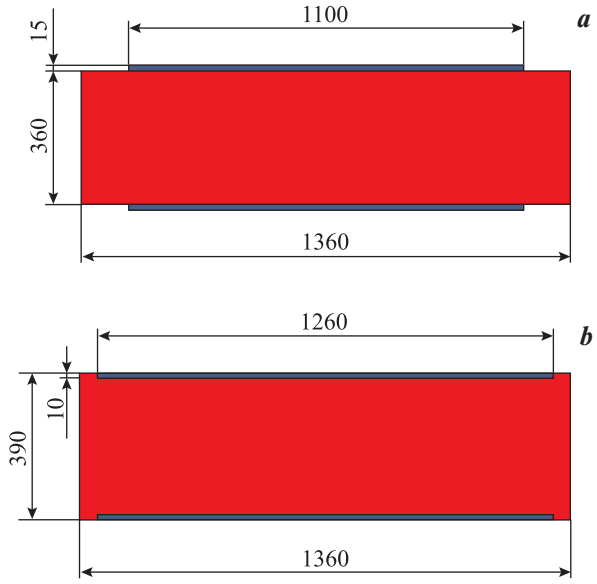

Fig. 2. Traditional (***a***) and new (***б***) schemes cladding plate placement schemes on the ingot

Рис. 2. Традиционная (***a***) и новая (***b***) схемы укладки планшетов на слиток

To describe frictional conditions at the contact with the rolls, Levanov's friction law was used:

$$\tau = mk(1 - e^{-1.25\sigma_n/\sigma_s}), \quad (3)$$

where τ is the shear friction stress (MPa); m is the friction factor; σ_n is the normal contact pressure (MPa); σ_s is the flow stress (MPa); and k is the maximum shear stress (MPa), proportional to σ_s according to the relationship $k = \sigma_s/\sqrt{3}$.

Since roll-bonding of the plates is carried out without a lubricant—coolant mixture, the friction factor at the contact between the work rolls and the workpiece was taken as $m = 0.95$.

For the contact between the aluminum—lithium alloy 1441 ingot and the ACpl alloy plates during the bonding stage, the same Levanov friction law (Eq. 3) was applied with $m = 1$.

Finite-element modeling was used to compare two cladding schemes: 1) the traditional scheme (Fig. 2, *a*), in which cladding plates are placed on the flat top and bottom faces of the ingot and roll-bonded over four passes with an absolute reduction of 6 mm per pass; and 2) the new scheme (Fig. 2, *b*), in which the plates are seated in pre-machined recesses milled into the top and bottom faces and roll-bonded in a single pass with an absolute reduction of 24 mm.

Results and discussion

During the 8-minute transfer of the ingot with cladding plates from the heating furnace, where the temperature was 450 °C, to the rolling stand, the

workpiece cooled in air. The calculated temperature field of the ingot with plates before rolling is shown in Fig. 3.

Because of the large difference in the geometric dimensions of the ingot and the plates, particular attention was paid to mesh refinement of the modeled objects. Fig. 4 shows the general view of the finite-element mesh. The maximum element sizes were as follows: global — no more than 30 mm; local — no more than 10 mm; and in the contact zone (Fig. 5) — no more than 1 mm. For the rolls along a 90° arc, the minimum number of elements was set to 180.

The temperature fields after roll-bonding the plates to the ingot for both cladding schemes are presented in Fig. 6. The mean ingot temperature (mathematical expectation) after four passes with absolute reductions of 6 mm was 399 °C (Fig. 7, *a*). After rolling in a single pass with an absolute reduction of 24 mm, the mean temperature was 422 °C (Fig. 7, *b*).

Thus, reducing three passes and, accordingly, three inter-pass pauses of 10 s each results in an average temperature increase of about 23 °C for the rough-rolled workpiece.

Although the absolute reduction per pass in the traditional scheme is quite small (only 6 mm), extrusion of the cladding plates from the ingot surface still occurs (Fig. 6, *a*). This effect arises because deformation is largely localized in the softer cladding layer (ACpl alloy) rather than penetrating into the stronger ingot core (alloy 1441).

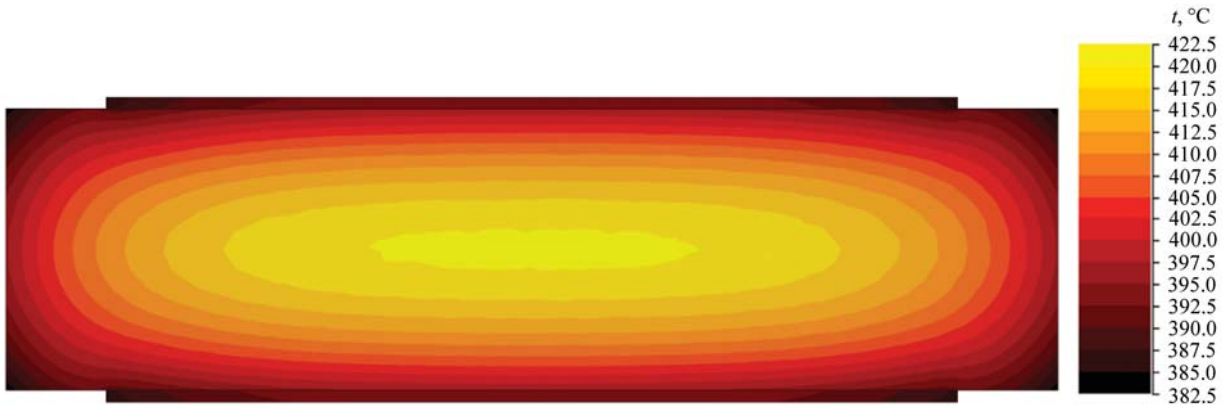

Fig. 3. Temperature field of the ingot with cladding plates before rolling

Рис. 3. Температурное поле слитка с планшетами перед началом прокатки

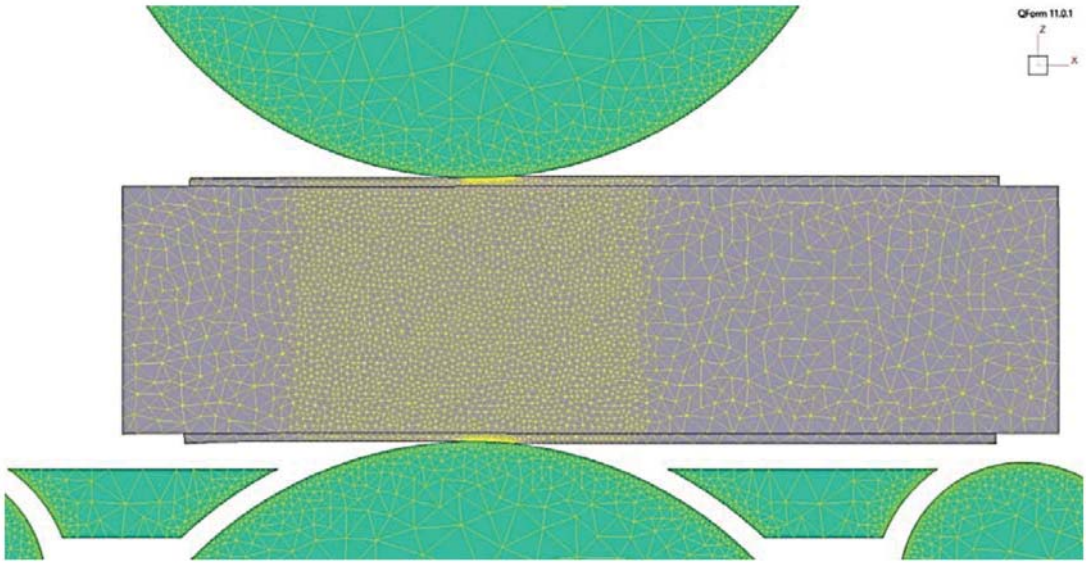

Fig. 4. General view of the finite-element mesh

Рис. 4. Общий вид сетки конечных элементов

The change in cladding-layer thickness during rolling differs significantly between the two schemes (Fig. 8). After four passes with reductions of 6 mm, the cladding-layer thickness decreases from the initial 15 mm to 8.8 mm. After rolling in a single pass with a 24 mm reduction, the thickness decreases from 10 mm to 9.3 mm. These results confirm that the new cladding scheme prevents plate extrusion from the ingot surface even under high absolute reductions, thereby allowing the use of thinner plates (10 mm instead of 15 mm).

The total initial thickness of the ingot with plates (390 mm) and the total absolute reduction (24 mm) were identical for both schemes. However, the deformation state of the base metal (alloy 1441) and the cladding layer (ACpl alloy) differed substantially (Fig. 9).

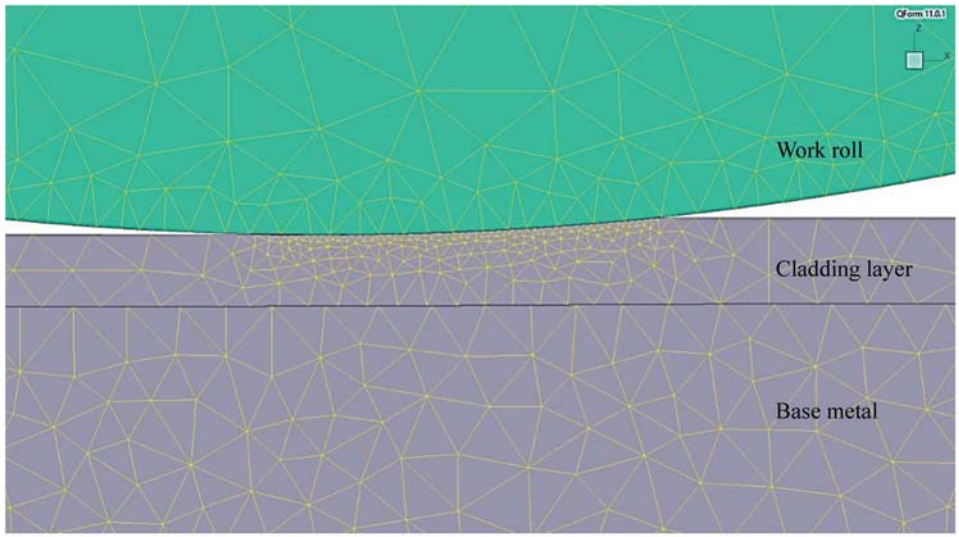

Fig. 5. Finite-element mesh in the contact zone

Рис. 5. Сетка конечных элементов в зоне контакта

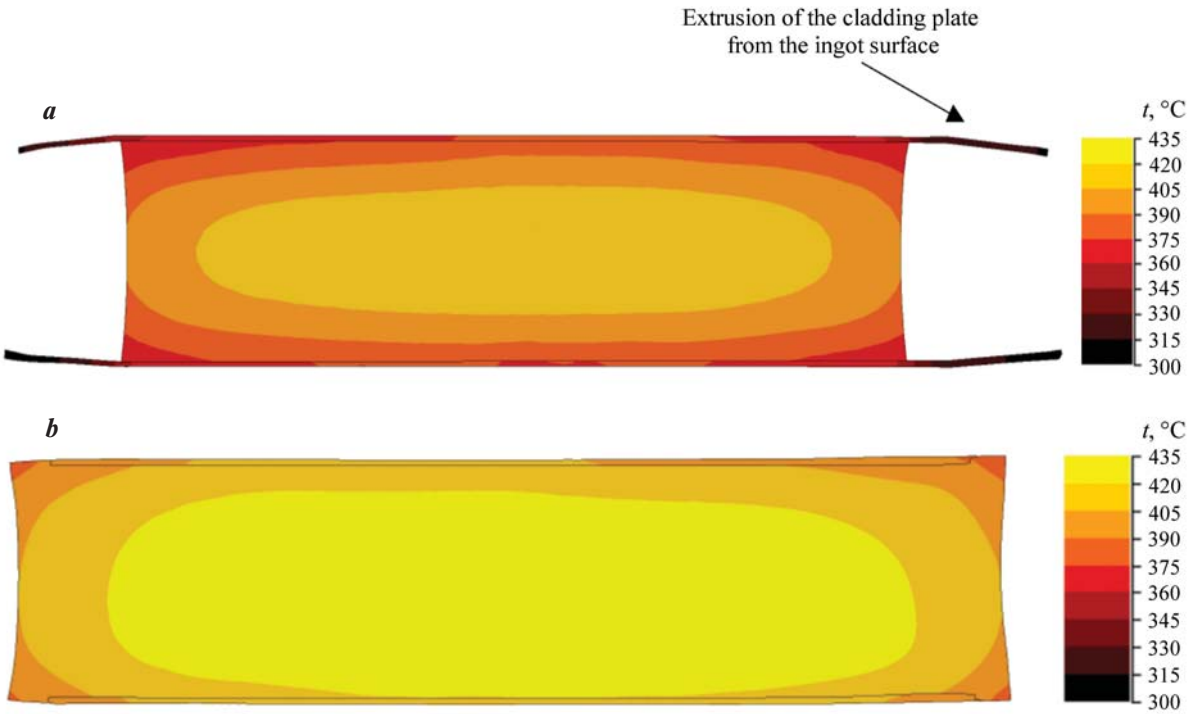

Fig. 6. emperature field after roll-bonding of cladding plates to the ingot for the traditional (***a***) and the new (***b***) schemes

Рис. 6. Температурное поле после приварки планшетов к слитку по традиционной (***a***) и новой (***b***) схемам

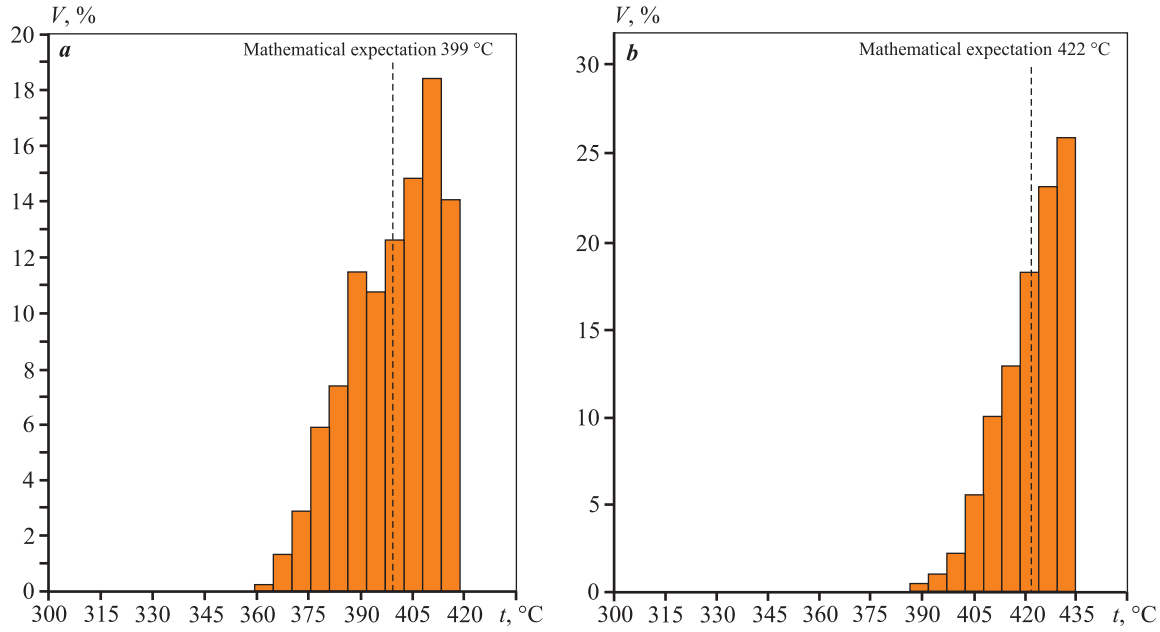

Fig. 7. Temperature distribution histograms over the ingot volume (V) after roll-bonding according to the traditional (***a***) and the new (***b***) schemes

Рис. 7. Гистограммы распределения температуры по объему (V) слитка после приварки планшетов по традиционной (***a***) и новой (***b***) схемам

The deformation state was characterized by the accumulated plastic strain ($\bar{\varepsilon}$), a dimensionless integral quantity. In QForm, the accumulated strain $\bar{\varepsilon}$ was calculated by numerical integration of the strain-rate intensity at each node [28]:

$$\bar{\varepsilon} = \sum_{n} \dot{\bar{\varepsilon}}^{n} \Delta b_n, \qquad (4)$$

where $\dot{\bar{\varepsilon}}^{n}$ is the strain-rate intensity (s^{-1}); Δb_n is the time-step increment (s), and n is the number of calculation steps.

The mean accumulated strain in the ingot (mathematical expectation) after four passes with reductions of 6 mm was 0.05 (Fig. 10, *a*). After a single-pass rolling with a 24 mm reduction, it doubled to 0.10 (Fig. 10, *b*).

In the cladding layer, on the contrary, the mean accumulated strain (mathematical expectation) after rolling according to the traditional scheme was higher — 0.98 (Fig. 11, *a*) — compared with 0.66 after rolling according to the new scheme (Fig. 11, *b*). Comparing the strain-distribution histograms in Fig. 11 shows that deformation in the cladding layer is more uniform when rolling is performed according to the new scheme.

For the Quarto 4600 roughing stand of KUMZ JSC, the energy—force parameters of both schemes

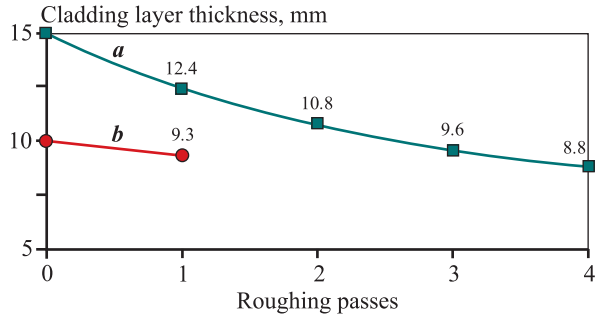

Fig. 8. Variation in cladding-layer thickness after rolling according to the traditional (***a***) and the new (***b***) schemes

Рис. 8. Изменение толщины плакирующего слоя по проходам после прокатки по традиционной (***a***) и новой (***b***) схемам

were evaluated. Because 2D modeling does not account for spread, the total strip width was assumed constant at 3300 mm. According to the simulation, in the traditional four-pass scheme (6 mm per pass), the maximum rolling forces ranged from approximately 21200 kN in the first pass to 25100 kN in the fourth (Fig. 12). For the new single-pass scheme with a 24 mm reduction, the maximum force was about 34000 kN (Fig. 12).

Importantly, the calculated rolling forces for both schemes did not exceed the permissible limit of

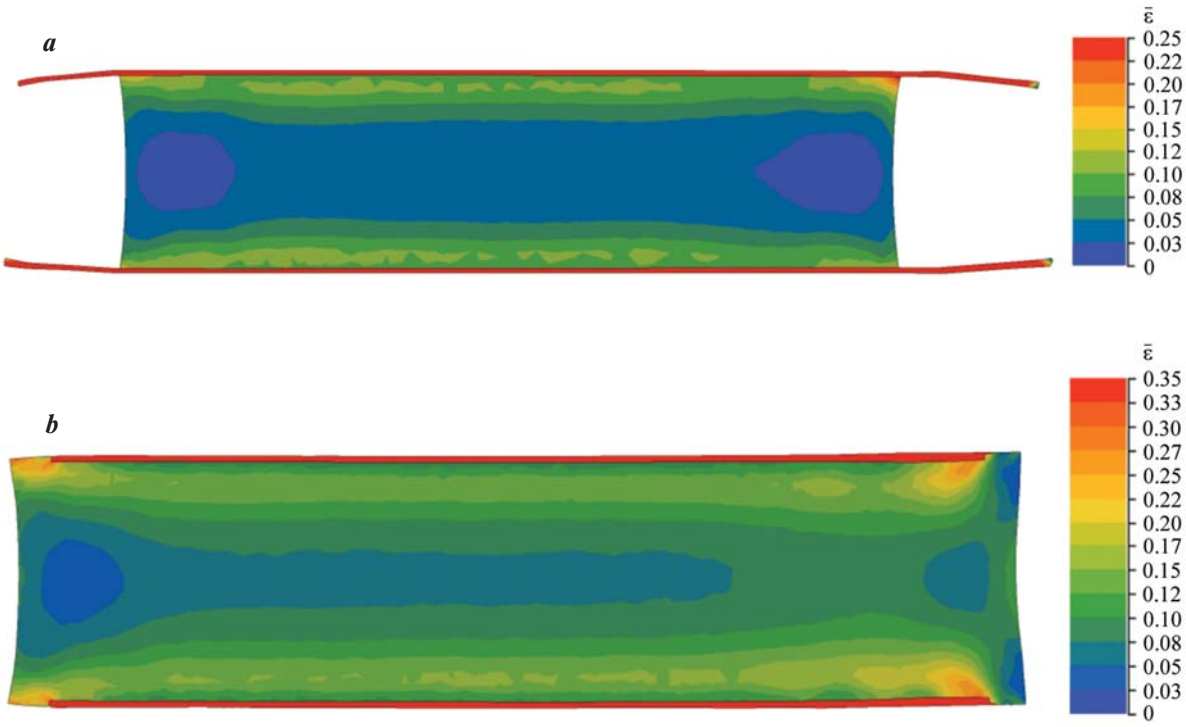

Fig. 9. Strain field after rolling according to the traditional (***a***) and the new (***b***) schemes

Рис. 9. Поле деформаций после прокатки по традиционной (***a***) и новой (***b***) схемам

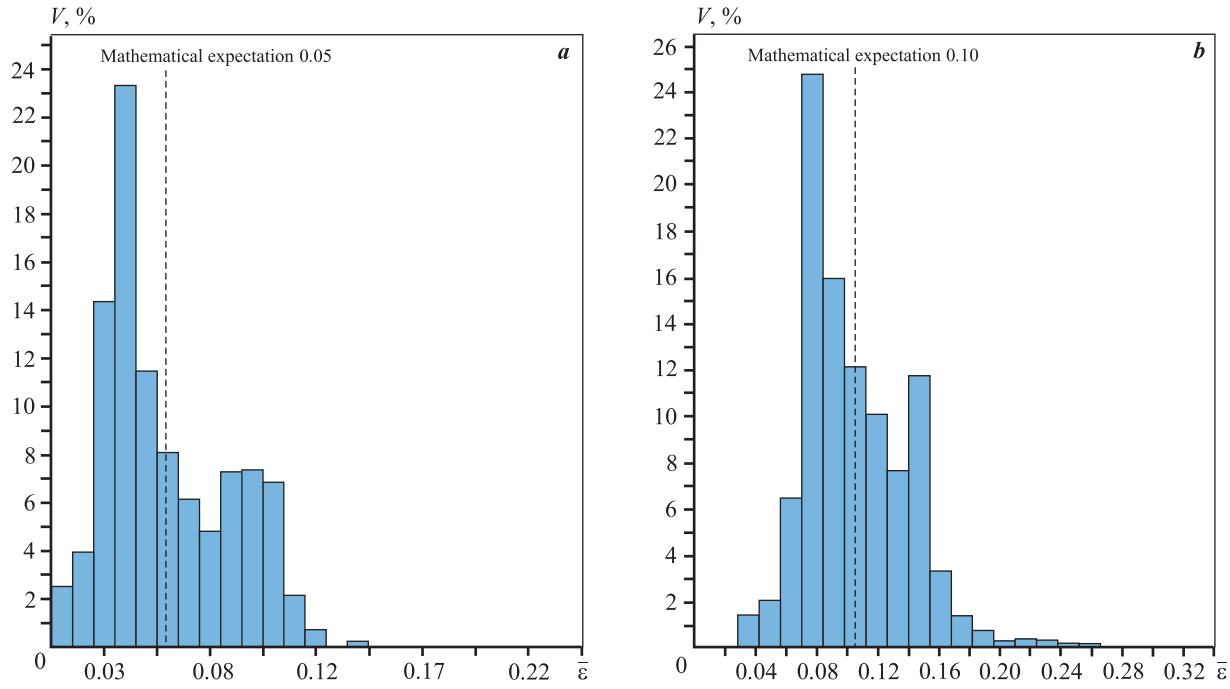

Fig. 10. Distribution histograms of accumulated strain ($\bar{\varepsilon}$) over the ingot volume (V) (base metal) after rolling according to the traditional (***a***) and the new (***b***) schemes

Рис. 10. Гистограммы распределения накопленной деформации ($\bar{\varepsilon}$) по объему (V) слитка (основного металла) после прокатки по традиционной (***a***) и новой (***b***) схемам

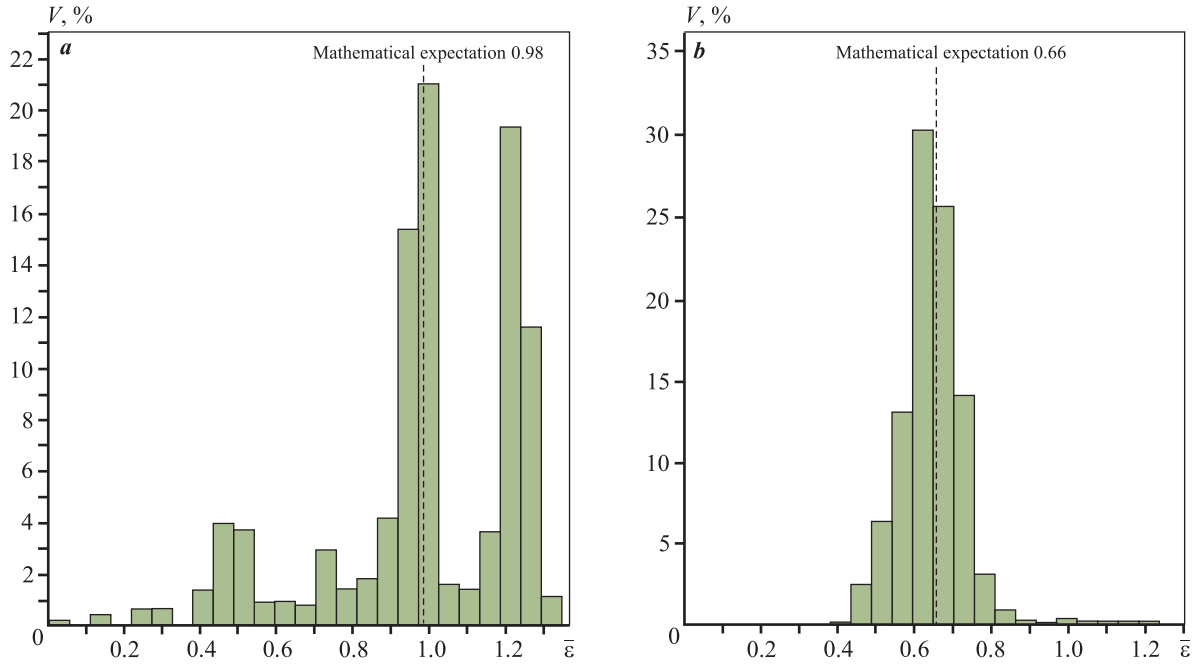

Fig. 11. Distribution histograms of accumulated strain over the cladding-layer volume (V) after rolling according to the traditional (***a***) and the new (***b***) schemes

Рис. 11. Гистограммы распределения накопленной деформации ($\bar{\varepsilon}$) по объему (V) плакирующего слоя после прокатки по традиционной (***a***) и новой (***b***) схемам

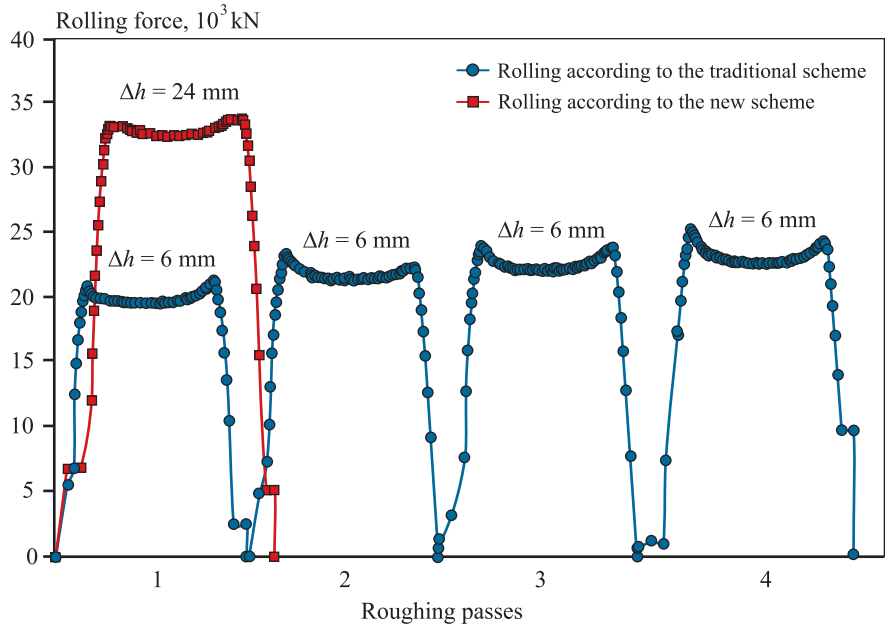

Fig. 12. Rolling forces in the traditional and new cladding schemes

Рис. 12. Усилия при прокатке по традиционной и новой схемам

80 000 kN, corresponding to the rated capacity of the Quarto 4600 roughing stand at KUMZ JSC.

Therefore, the finite-element analysis confirms the technological feasibility of the proposed cladding scheme for aluminum—lithium alloy 1441 ingots. For flat ingots of 390 × 1360 mm, implementation of the new scheme requires adjustment of the milling configuration on the wide faces (Fig. 13).

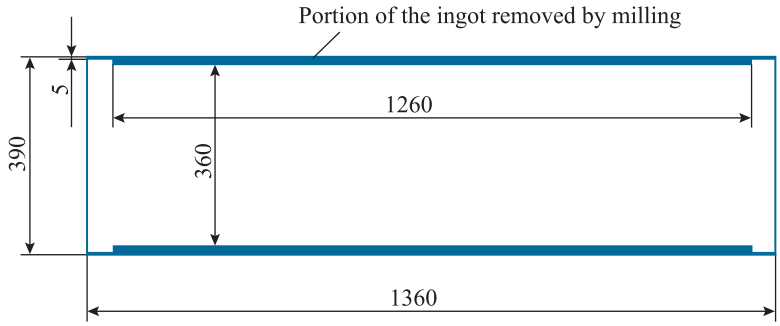

Fig. 13. Portion of the ingot surface to be removed by milling in the new cladding scheme

Рис. 13. Удаляемая фрезерованием часть слитка при реализации новой схемы плакирования

Conclusions

1. A finite-element analysis was carried out to assess the technological feasibility of implementing a new cladding scheme for aluminum—lithium alloy 1441 ingots. Instead of the traditional scheme, which involves roll-bonding of cladding plates to the ingot in four passes with absolute reductions of 6 mm per pass, the new approach proposes placing the plates into pre-machined recesses on the upper and lower surfaces of the ingot and achieving roll-bonding in a single pass with an absolute reduction of 24 mm.

2. The new cladding scheme makes it possible to significantly reduce the total number of passes and inter-pass pauses during rough rolling, thereby improving the thermal condition of the workpiece before finish rolling. It is expected that the higher temperature will reduce the likelihood of edge cracking during finish rolling. A reduction of three passes and three 10-second pauses increases the mean temperature by approximately 23 °C.

3. The proposed scheme prevents extrusion of the cladding plates from the ingot surface even at high absolute reductions. This allows the use of thinner cladding plates — 10 mm instead of the conventional 15 mm.

4. The deformation state of the base metal (alloy 1441) and the cladding layer (ACpl alloy) differs substantially between the two schemes. The mean accumulated strain in the ingot after four passes with 6 mm reductions was 0.05, while after a single-pass rolling with a 24 mm reduction it doubled to 0.10. At the same time, deformation of the cladding layer in the new scheme was more uniform.

5. The results of the finite-element modeling can be used to improve and optimize the technological parameters of hot rolling for clad sheets and strips made of aluminum—lithium alloy 1441 under the production conditions of KUMZ JSC.

References

1. Betsofen S.Ya., Antipov V.V., Knyazev M.I. Al—Cu—Li and Al—Mg—Li alloys: Phase composition, texture, and anisotropy of mechanical properties (Review). *Russian Metallurgy (Metally)*. 2016;2016:326—341. https://doi.org/10.1134/S0036029516040042
2. Rioja R.J., Liu J. The evolution of Al—Li base products for aerospace and space applications. *Metallurgical and Materials Transactions A*. 2012;43:3325—3337. https://doi.org/10.1007/s11661-012-1155-z
3. El-Aty A.A., Xu Y., Guo X., Zhang S.-H., Ma Y., Chen D. Strengthening mechanisms, deformation behavior, and anisotropic mechanical properties of Al—Li alloys: A review. *Journal of Advanced Research*. 2018;10:49—67. https://doi.org/10.1016/j.jare.2017.12.004
4. Antipov V.V., Tkachenko E.A., Zaitsev D.V., Selivanov A.A., Ovsyannikov B.V. Influence of homogenization annealing modes on the structural-phase state and mechanical properties of ingots made of aluminum-lithium alloy 1441. *Trudy VIAM*. 2019;3(75):44—52. (In Russ.). https://doi.org/10.18577/2307-6046-2019-0-3-44-52
Антипов В.В., Ткаченко Е.А., Зайцев Д.В., Селиванов А.А., Овсянников Б.В. Влияние режимов гомогенизационного отжига на структурно-фазовое состояние и механические свойства слитков из алюминий-литиевого сплава 1441. *Труды ВИАМ*. 2019;3(75):44—52. https://doi.org/10.18577/2307-6046-2019-0-3-44-52
5. Li H., Zou Z., Li J., Xu G., Zheng Z. Correlation between grain structures and tensile properties of Al—Li alloys. *Transactions of Nonferrous Metals Society of China*. 2023;33(12):3597—3611. https://doi.org/10.1016/S1003-6326(23)66357-5
6. Ovsyannikov B.V. New aluminum-lithium alloy of the Al—Cu—Mg—Li(Ag,Sc) system intended for the

production of thin sheets and profiles. *Non-Ferrous Metals*. 2014;(11):90—94. (In Russ.).
Овсянников Б.В. Новый алюминиево-литиевый сплав системы Al—Cu—Mg—Li(Ag,Sc), предназначенный для изготовления тонких листов и профилей. *Цветные металлы*. 2014;(11):90—94.

7. Kokovin P.L., Maltseva T.V., Ovsyannikov B.V. Mastering the technology of casting large-sized flat ingots from a new generation aluminum-lithium alloy. *Liteishchik Rossii*. 2023;(1):21—24. (In Russ.).
Коковин П.Л., Мальцева Т.В., Овсянников Б.В. Освоение технологии литья крупногабаритных плоских слитков из алюминиево-литиевого сплава нового поколения. *Литейщик России*. 2023;(1):21—24.
8. Ovsyannikov B.V., Komarov S.B. Development of production of deformed semi-finished products from aluminum-lithium alloys at JSC "KUMZ". *Tekhnologiya legkikh splavov*. 2014;(1):97—103. (In Russ.).
Овсянников Б.В., Комаров С.Б. Развитие производства деформированных полуфабрикатов из алюминиево-литиевых сплавов в ОАО «КУМЗ». *Технология легких сплавов*. 2014;(1):97—103.
9. Hajjioui E.A., Bouchaala K., Faqir M., Essadiqi E. A review of manufacturing processes, mechanical properties and precipitations for aluminum lithium alloys used in aeronautic applications. *Heliyon*. 2023;9(3):e12565. https://doi.org/10.1016/j.heliyon.2022.e12565
10. Duan S.Y., Huang L.K., Yang S.H., Zhou Z., Song S.J., Yang X.B., Chen Y.Z., Li Y.J., Liu G., Liu F. Uncovering the origin of enhanced strengthening in Li-added Al—Cu—Mg alloys. *Materials Science and Engineering: A*. 2021;827:142079. https://doi.org/10.1016/j.msea.2021.142079
11. Rioja R.J., Liu J. The evolution of Al—Li base products for aerospace and space applications. *Metallurgical and Materials Transactions A*. 2012;43(9):3325—3337. https://doi.org/10.1007/s11661-012-1155-z
12. First-principles insights into solute partition among various nano-phases in Al—Cu—Li—Mg alloys. *Transactions of Nonferrous Metals Society of China*. 2024:34(6): 1734—1744. https://doi.org/10.1016/S1003-6326(24)66503-9
13. Kolobnev N.I., Khokhlatova L.B., Antipov V.V. Promising aluminum-lithium alloys for aircraft structures. *Tekhnologiya legkikh splavov*. 2007;(2):35—38. (In Russ.).
Колобнев Н.И., Хохлатова Л.Б., Антипов В.В. Перспективные алюминий-литиевые сплавы для самолетных конструкций. *Технология легких сплавов*. 2007;(2):35—38.
14. Pantelakis S.G., Chamos A.N., Setsika D. Tolerable corrosion damage on aircraft aluminum structures: Local cladding patterns. *Theoretical and Applied Fracture Mechanics*. 2012;58(1):55—64. https://doi.org/10.1016/j.tafmec.2012.02.008
15. Corrosion of aluminum and aluminum alloys. Ed. D.R. Davis. Transl. Yu.I. Kuznetsov, M.Z. Lokshin. Moscow: NP «APRAL», 2016. 333 p. (In Russ.).
Коррозия алюминия и алюминиевых сплавов. Под ред. Д.Р. Дэйвиса. Пер. с англ. Ю.И. Кузнецова, М.З. Локшина. М.: НП «АПРАЛ», 2016. 333 с.
16. Razinkin A.V., Maltseva T.V., Ovsyannikov B.V., Levina A.V. Typical defects in ingots and semi-finished products made of aluminum deformable alloys. Ekaterinburg: Uralskii rabochii, 2023. 144 p. (In Russ.).
Разинкин А.В., Мальцева Т.В., Овсянников Б.В., Левина А.В. Типовые дефекты в слитках и полуфабрикатах из алюминиевых деформируемых сплавов. Екатеринбург: Уральский рабочий, 2023. 144 с.
17. Degtyarev A.V., Maltseva T.V., Glinskikh P.I., Yakovlev S.I. Technological features of production of clad sheets from hard aluminum alloys at JSC "KUMZ". *Tekhnologiya legkikh splavov*. 2024;(2):40—46 (In Russ.). https://doi.org/10.24412/0321-4664-2024-2-40-46
Дегтярев А.В., Мальцева Т.В., Глинских П.И., Яковлев С.И. Технологические особенности производства плакированных листов из твердых алюминиевых сплавов в ОАО «КУМЗ». *Технология легких сплавов*. 2024;(2):40—46. https://doi.org/10.24412/0321-4664-2024-2-40-46
18. Orlov V.K., Drozd V.G., Sarafanov M.A., Specific features of aluminum alloy plates rolling. *Proizvodstvo prokata*. 2016;(4):11—16. (In Russ.).
Орлов В.К., Дрозд В.Г., Сарафанов М.А. Особенности прокатки плит из алюминиевых сплавов. *Производство проката*. 2016;(4):11—16.
19. Yashin V.V., Beglov E.D., Aryshensky E.V., Latushkin I.A. Effect of cladding layer thickness on deformation distribution over ingot cross-section. In: *IX International congress "Non-ferrous metals and minerals-2017"* (Krasnoyarsk, 11–15 September 2017). Krasnoyarsk, 2017. P. 735–744. (In Russ.).
Яшин В.В., Беглов Э.Д., Арышенский Е.В., Латушкин И.А. Влияние толщины плакирующего слоя на распределение деформации по сечению слитка. В сб.: *IX Международный конгресс «Цветные металлы и минералы-2017»* (Красноярск, 11—15 сент. 2017). Красноярск, 2017. С. 735—744.
20. Torikai G., Yoshida Y., Asano M., Niikura A. Visualization of metal flow and adhering of aluminum alloy in three-layer clad rolling. *Procedia Manufacturing*. 2018;15: 144—151. https://doi.org/10.1016/j.promfg.2018.07.188

21. Puchkova L.M. Features of joint rolling of high layered strips of different-strength metals. *Proizvodstvo prokata*. 2014;(9):3—10. (In Russ.).
Пучкова Л.М. Особенности совместной прокатки высоких слоистых полос разнопрочных металлов. *Производство проката*. 2014;(9):3—10.
22. Khan H.A., Asim K., Akram F., Hameed A., Khan A., Mansoor B. Roll bonding processes: State-of-the-art and future perspectives. *Metals*. 2021;11(9):1344. https://doi.org/10.3390/met11091344
23. Zixuan L., Shahed R., Tao W., Han J., Shu X., Pater Z., Huang Q. Recent advances and trends in roll bonding process and bonding model: A review. *Chinese Journal of Aeronautics*. 2023;36(4):36—74. https://doi.org/10.1016/j.cja.2022.07.004
24. Kebriaei R., Vladimirov I.N., Reese S. Joining of the alloys AA1050 and AA5754 — Experimental characterization and multiscale modeling based on a cohesive zone element technique. *Journal of Materials Processing Technology*. 2014;214(10):2146—2155. https://doi.org/10.1016/j.jmatprotec.2014.03.014
25. Salikhyanov D.R. Investigation of the stress-strain state at the boundary between materials during rolling of a layered composite. *Ferrous Metals*. 2023;(9):34—39. (In Russ.). https://doi.org/10.17580/chm.2023.09.06
Салихянов Д.Р. Исследование напряженно-деформированного состояния на границе между материалами при прокатке слоистого композита. *Черные металлы*. 2023;(9):34—39.
26. Koshmin A., Zinoviev A., Cherkasov S., Ali Alhaj A.M., Tsydenov K., Churyumov A. Finite element modeling and experimental verification of a new aluminum Al—2%Cu—2%Mn alloy hot cladding by flat rolling. *Metals*. 2024;14(8):852. https://doi.org/10.3390/met14080852
27. Zinyagin A.G., Borisenko N.R., Muntin A.V., Kryuchkova M.O. Features of finite element modeling for hot rolling process of clad sheets and strips. *CIS Iron and Steel Review*. 2023;26(2):51—57. https://doi.org/10.17580/cisisr.2023.02.08
28. Vlasov A.V., Stebunov S.A., Evsyukov S.A., Biba N.V., Shitikov A.A. Finite element modeling of technological processes of forging and bulk stamping: a tutorial. Moscow: Publ. House of the Bauman MSTU, 2019. 384 p. (In Russ.).
Власов А.В., Стебунов С.А., Евсюков С.А., Биба Н.В., Шитиков А.А. Конечно-элементное моделирование технологических процессов ковки и объемной штамповки: Учеб. пос. М.: Изд-во МГТУ им. Н.Э. Баумана, 2019. 384 с.

Information about the authors

Aleksandr M. Pesin – Dr. Sci. (Eng.), Prof., Chief Researcher of the Laboratory of Mechanics of Gradient Nanomaterials n.a. A.P. Zhilyaev, Nosov Magnitogorsk State Technical University (NMSTU).
https://orcid.org/0000-0002-5443-423X
E-mail: pesin@bk.ru

Aleksandr V. Razinkin – Cand. Sci. (Eng.), Director of Production, PJSC "Kamensk-Uralsky Metallurgical Plant" (PJSC "KUMP").
https://orcid.org/0009-0006-2851-227X
E-mail: RazinkinAV@kumz.ru

Vladimir A. Zamaraev – Engineer, PJSC "KUMP".
https://orcid.org/0009-0006-6743-9212
E-mail: zamaraevva@kumw.ru

Denis O. Pustovoitov – Cand. Sci. (Eng.), Associate Professor, Leading Researcher of the Laboratory of Mechanics of Gradient Nanomaterials n.a. A.P. Zhilyaev, NMSTU.
https://orcid.org/0000-0003-0496-0976
E-mail: pustovoitov_den@mail.ru

Информация об авторах

Александр Моисеевич Песин – д.т.н., профессор, гл. науч. сотрудник лаборатории «Механика градиентных материалов им. А.П. Жиляева» Магнитогорского государственного технического университета (МГТУ) им. Г.И. Носова.
https://orcid.org/0000-0002-5443-423X
E-mail: pesin@bk.ru

Александр Викторович Разинкин – к.т.н., директор по производству ПАО «Каменск-Уральский металлургический завод» (ПАО «КУМЗ»).
https://orcid.org/0009-0006-2851-227X
E-mail: RazinkinAV@kumz.ru

Владимир Андреевич Замараев – инженер-технолог ПАО «КУМЗ».
https://orcid.org/0009-0006-6743-9212
E-mail: zamaraevva@kumw.ru

Денис Олегович Пустовойтов – к.т.н., доцент, вед. науч. сотрудник лаборатории «Механика градиентных материалов им. А.П. Жиляева» МГТУ им. Г.И. Носова.
https://orcid.org/0000-0003-0496-0976
E-mail: pustovoitov_den@mail.ru

Contribution of the authors

A.M. Pesin – proposed the new cladding scheme for aluminum–lithium alloy 1441 ingots, participated in the discussion of the results.

A.V. Razinkin – defined the aim of the study, specified the initial and boundary conditions for modeling the ingot cladding process, participated in the discussion of the results.

V.A. Zamaraev – prepared specimens and obtained experimental flow-stress data for alloy 1441, participated in the discussion of the results.

D.O. Pustovoitov – performed finite-element modeling of the ingot cladding process in QForm, participated in the discussion of the results, wrote the manuscript.

Вклад авторов

А.М. Песин – предложение новой схемы плакирования слитков из алюминий-литиевого сплава 1441, участие в обсуждении результатов.

А.В. Разинкин – определение цели работы, задание начальных и граничных условий для моделирования процесса плакирования слитков, участие в обсуждении результатов.

В.А. Замараев – приготовление образцов и получение экспериментальных данных о сопротивлении деформации сплава 1441, участие в обсуждении результатов.

Д.О. Пустовойтов – моделирование процесса плакирования слитков методом конечных элементов в программе «QForm», участие в обсуждении результатов, написание статьи.

The article was submitted 13.09.2024, revised 11.03.2025, accepted for publication 13.03.2025

Статья поступила в редакцию 13.09.2024, доработана 11.03.2025, подписана в печать 13.03.2025

UDC 621.701.12
https://doi.org/10.17073/0021-3438-2025-4-50-61

Research article
Научная статья

Influence of plasma narrow-jet cutting parameters on the weld quality during laser welding of titanium alloys

S.V. Anakhov[1], **B.N. Guzanov**[1], **N.S. Michurov**[2]

[1] **Russian State Vocational Pedagogical University**
11 Mashinostroiteley Str., Ekaterinburg 620012, Russia

[2] **Ural Institute of State Fire Service of EMERCOM**
22 Mira Str., Ekaterinburg 620062, Russia

✉ Sergey V. Anakhov (sergej.anahov@rsvpu.ru)

Abstract: The study investigates the structural and mechanical characteristics of permanent joints produced by laser welding of VT1-0/VT1-0 titanium alloys after cutting with a newly designed PMVR-5.3 narrow-jet plasma torch, which features a gas-dynamic stabilization (GDS) system with several design innovations. The improved GDS efficiency enhances cutting precision and surface quality, thereby increasing the radiation absorption coefficient, weld penetration, and overall laser-welding efficiency. Experimental results show that continuous-wave CO_2 laser welding of VT1-0/VT1-0 plates forms a narrow weld with a structure corresponding to the as-cast state of the alloy and large equiaxed grains in the central part of the weld, which decrease in size toward the root compared with those in the surface region. Although gas shielding does not completely prevent the formation of fine micropores in the weld metal, their amount is insignificant; they do not form critical clusters within the microvolumes of the weld and have no adverse effect on the strength characteristics of the welded joint. The average microhardness of the weld metal was found to be higher than that of the base metal. According to tensile and microhardness testing, the weld metal demonstrates high strength, significantly exceeding that of the titanium alloy, and exhibits a ductile fracture morphology. Under cyclic loading, fracture occurred in the base metal rather than in the weld metal, with the fraction of the final rupture zones increasing as the maximum cyclic stress rose. The findings confirm the applicability of precision narrow-jet air-plasma cutting and continuous-wave CO_2 laser welding technologies for producing VT1-0/VT1-0 welded joints with high efficiency and mechanical strength comparable to those of the base material.

Keywords: laser welding, plasma cutting, titanium alloys, weld metal, heat-affected zone, structural transformations, defects, quality, efficiency.

Acknowledgements: The work was supported by the Russian Science Foundation, grant No. 23-29-00111.

The authors thank E.B. Trushina for assistance with fractographic examination of specimen fracture surfaces after mechanical testing, and D.I. Vychuzhanin (Cand. Sci. (Eng.)), for assistance with the mechanical tests.

For citation: Anakhov S.V., Guzanov B.N., Michurov N.S. Influence of plasma narrow-jet cutting parameters on the weld quality during laser welding of titanium alloys. *Izvestiya. Non-Ferrous Metallurgy.* 2025;31(4):50–61. https://doi.org/10.17073/0021-3438-2025-4-50-61

Влияние особенностей плазменной узкоструйной резки на качество сварного шва при лазерной сварке титановых сплавов

С.В. Анахов[1], **Б.Н. Гузанов**[1], **Н.С. Мичуров**[2]

[1] **Российский государственный профессионально-педагогический университет**
Россия, 620012, г. Екатеринбург, ул. Машиностроителей, 11

[2] **Уральский институт государственной противопожарной службы МЧС России**
Россия, 620062, Екатеринбург, ул. Мира, 22

✉ Сергей Вадимович Анахов (sergej.anahov@rsvpu.ru)

Аннотация: Исследованы особенности формирования структуры и свойств неразъемных соединений при лазерной сварке титановых сплавов типа ВТ1-0/ВТ1-0, полученных после резки новым узкоструйным плазмотроном типа ПМВР-5.3, имеющим ряд конструктивных особенностей в системе газодинамической стабилизации (ГДС) плазменной дуги. Достигнутое преимущество в эффективности ГДС способствует повышению степени прецизионности и качества реза и, как следствие, увеличению коэффициента поглощения излучения, коэффициента проплавления и эффективности лазерной сварки. По результатам исследований показано, что при получении углекислотным лазером сварных соединений типа ВТ1-0/ВТ1-0 происходит формирование узкого шва со структурой, соответствующей литому состоянию сплава, и участков с крупными равноосными зернами в центральной части шва, уменьшающимися по размерам в донной части по сравнению с расположенными в поверхностной области. Защита сплава от газонасыщения в структуре сварного шва не позволяет избежать формирования мелких микропор в структуре сварного шва, однако их количество незначительно и они не создают критических скоплений в микрообъемах шва и не влияют на прочностные характеристики неразъемного соединения, при этом средние значения микротвердости материала шва выше, чем материала основы. В результате испытаний на статическое растяжение, а также определения значения микротвердости установлено, что материал сварного шва является достаточно прочным и существенно превышает прочность самого титанового сплава, а рельеф поверхности разрушения образцов соответствует вязкому разрушению. При циклических испытаниях образцов сварных соединений разрушение происходило не по шву, а по основному металлу с ростом доли зон долома в сечении образцов при увеличении значений максимального напряжения цикла. По результатам исследований можно сделать вывод о применимости технологий прецизионной узкоструйной воздушно-плазменной резки и сварки углекислотным лазером непрерывного действия для реализации процесса получения сварных соединений ВТ1-0/ВТ1-0 с высокой степенью эффективности и прочности на уровне соединяемых материалов.

Ключевые слова: лазерная сварка, плазменная резка, титановые сплавы, сварной шов, зона термического влияния, структурные превращения, дефекты, качество, эффективность.

Благодарности: Работа выполнена при поддержке гранта РНФ № 23-29-00111.

Авторы выражают благодарность Е.Б. Трушиной за помощь в проведении исследований фрактографии поверхности образцов после механического испытания и к.т.н. Д.И. Вычужанину за помощь в проведении механических испытаний.

Для цитирования: Анахов С.В., Гузанов Б.Н., Мичуров Н.С. Влияние особенностей плазменной узкоструйной резки на качество сварного шва при лазерной сварке титановых сплавов. *Известия вузов. Цветная металлургия*. 2025;31(4):50–61.
https://doi.org/10.17073/0021-3438-2025-4-50-61

Introduction

Extensive research on titanium and its alloys conducted in recent years has unequivocally demonstrated that, in terms of their physical, mechanical, chemical, and technological properties, these materials surpass most modern structural alloys, including the most common ones such as steel and aluminum. The continuous growth in their application is attributed to the fact that titanium alloys combine low density with high strength and heat resistance at moderate temperatures while maintaining excellent corrosion resistance. These ad-

vantages have made titanium a versatile structural material, particularly in high-technology industries where titanium alloys with diverse properties are often essential — or even irreplaceable — for strategic sectors such as aerospace, nuclear power, shipbuilding, and chemical engineering [1—3].

The development of welding methods capable of producing high-quality, permanent joints has significantly expanded the use of titanium and its alloys in manufacturing complex engineering components and metal structures. However, welding titanium alloys presents certain technological challenges. These are primarily associated with the high chemical reactivity of titanium with nitrogen, oxygen, and hydrogen at elevated temperatures and in the molten state. As a result, the material may lose ductility due to the formation of stable compounds with atmospheric gases, as well as develop defects such as porosity. To prevent such issues, it is essential to ensure reliable shielding of both the weld zone and the root side from atmospheric contamination and to minimize the heating time of the joint during welding [4].

A major drawback of titanium alloys is their tendency to form a coarse-grained structure during welding, both in the weld metal and in the heat-affected zone (HAZ). This structural heterogeneity leads to a decrease in the mechanical strength of the joint due to the formation of a microstructure that differs from that of the base metal [5; 6]. Since different regions within the welded joint are exposed to varying thermal cycles, grains of different sizes form, complicating the selection of welding parameters that minimize the thermal impact on the HAZ. From this perspective, laser welding is considered a promising alternative to conventional welding methods [7]. The localized and short-duration high-energy exposure of the laser beam provides the most favorable conditions for forming sound welds in titanium and its alloys [8; 9].

Technologies and research objective

While laser technologies have a number of undeniable advantages in welding processes for the fabrication of various metal structures [10; 11], certain features of beam processing must also be taken into account. Chief among them is the relatively low efficiency of the process, as the effectiveness of laser welding largely depends on the reflective properties of the metal surface. Several approaches are known to improve the absorption coefficient — and consequently, the penetration depth and overall welding efficiency. As demonstrated in [12], the absorption coefficient is affected by the material properties, as well as by the quality and method of edge preparation, which determine surface roughness and the geometry of the joint gap in butt-welded plates. Comprehensive studies evaluating the relationship between absorption coefficient and cut-edge quality have shown a significant increase in reflected radiation from rougher surfaces compared with polished ones [13—15]. Thus, it should be noted that surface roughness produced during sheet cutting in the preparation stage varies widely depending on the cutting method used.

The authors conducted comparative studies to evaluate the cut-edge quality achieved using various high-energy cutting techniques for the preparation of welded joints. The results indicated that the most favorable outcomes across all standardized parameters were obtained when using precision air—plasma cutting of metallic materials with the PMVR-5.3 plasma torch, developed by NPO Polygon LLC (Ekaterinburg, Russia) [16]. A distinctive feature of this design is the implementation of a new gas—air flow path with symmetric plasma-forming gas injection into the flow-splitting system and a gas-dynamic flow stabilizer. The stabilizer employs two swirlers (forming and stabilizing) with a variable number of swirl channels, providing efficient gas-vortex stabilization of the plasma arc. The evaluation focused on standardized quality indicators such as the presence of burrs, droplets, and temper colors, as well as oscillations (variations in the linearity of surface micro-irregularities) and deviation of the cut edge from verticality. To substantiate the visual inspection results quantitatively, surface microrelief parameters were measured using a TR-200 surface roughness tester [17]. The results are presented in Table 1.

According to geometric and surface-quality characteristics after high-energy cutting, the most favorable results for subsequent laser welding were obtained using the PMVR-5.3 plasma torch, designed as a domestic alternative to imported plasma systems of this class. Moreover, as demonstrated in [17], enhanced weld penetration and improved weld formation during laser processing were achieved when the cut-edge roughness ranged between $Ra \approx 2.0 \div 6.3$ μm, which promotes a higher absorption coefficient on the prepared surfaces. With further increases in roughness, however, the joint gap between the welded plates widens, allowing a substantial portion of the laser beam to pass through without absorption. Consequently, the absorption coefficient decreases, resulting in lower weld quality and a higher incidence of defects.

Table 1. **Comparison of average surface roughness parameters for various high-temperature cutting technologies**

Таблица 1. Сравнение средних показателей шероховатости реза при различных технологиях высокотемпературной разделки

Specimen	Cutting technology	Equipment	Cutting parameters	*Ra*	*Rz*	*Rt*
1	Air–plasma	Plasma torch YK200H (Huayuan FLG-400HD, China)	I = 175 A U = 155 B V = 1500 mm/min D_{nozzle} = 1.9 mm	3.30	4.22	34.82
2	Air–plasma	Plasma torch PMVR-5.3 (NPO Polygon LLC, Russia)	I = 175 A U = 137 B V = 1500 mm/min D_{nozzle} = 1.9 mm P = 4.5 atm	2.17	2.70	58.48
3	Gas–oxygen	Mechanized gas-cutting system Longteng (China)	P_{O_2} = 5 atm $P_{C_3H_8}$ = 0.5 atm V = 1500 mm/min	3.71	4.65	33.86
4	Laser	Trulaser 5030 Classic, CO_2 (Trumpf Group, Germany)	N = 1,7 kW f = 2 kHz V = 600 mm/min P = 0.6 bar	10.78	12.61	69.41

In view of the above, the objective of this study was to investigate the structural and mechanical characteristics of permanent joints formed during laser welding of titanium alloys, where the plates were cut using narrow-jet air—plasma cutting technology implemented with the PMVR-5.3 plasma torch.

Materials and methods

Titanium alloys are known for their tendency to undergo hardening due to the presence of alloying elements that promote the formation of nonequilibrium microstructures and reduce ductility, sometimes resulting in cold cracking [18, 19]. For this reason, commercially pure titanium VT1-0 was selected as the material for this study. During welding, this alloy forms a cast structure characteristic of pure titanium in the joint zone, allowing the assessment of weld quality without the influence of additional phase or structural transformations.

Laser welding of 3 mm-thick titanium plates, previously cut by plasma, was carried out using a continuous-wave CO_2 laser with a maximum power of 3 kW. The laser was equipped with a zinc selenide (ZnSe) focusing lens (focal length 254 mm) and produced a plane-polarized beam with a diameter of 30 mm. The welding parameters were as follows: welding speed V = = 46.6 mm/s, laser power W = 2.1 kW, and focal offset F = 0 mm. Protection of the weld pool and heat-affected zone was provided by a shielding gas mixture of carbon dioxide and air in a ratio of 1 : 7, in accordance with GOST R ISO 14175-2010[1], at a pressure of 12 Torr (1.6 kPa). Metallographic analysis was performed using an optical microscope Neophot 21 (Germany). The titanium structure and weld morphology were revealed by chemical etching, which was also used to prepare the surface for microindentation testing. The weld and adjacent zones were analyzed on specimens cut from different areas of the joint, taking into account structural features formed during solidification following high-temperature processing. Grain size was determined in accordance with GOST 21073.3-75[2]

[1] GOST R ISO 14175-2010. Welding materials. Gases and gas mixtures for fusion welding and related processes. Moscow: Standartinform, 2011. (In Russ.).

[2] GOST 21073.3-75. Non-ferrous metals. Determination of grain size by counting border crossings. Moscow: Publ. Standards, 2002. (In Russ.).

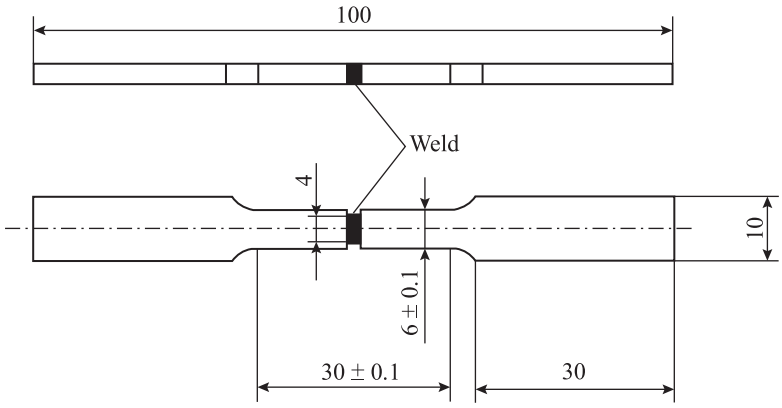

Fig. 1. Schematic representation of the specimen used for tensile testing

Рис. 1. Схематическое изображение образца для испытаний на растяжение

using the grain boundary intersection counting method. Microhardness across the weld was measured by instrumented Vickers microindentation using a Fischerscope HM 2000 XYm microhardness tester (Helmut Fischer GmbH, Germany). The tensile strength of the welded joints was evaluated using a servo-hydraulic testing machine Instron 8801 (Instron, USA) in accordance with GOST 6996-66[1]. Flat specimens of type B, designed for determining weld metal strength, were used. To ensure fracture propagation through the weld, a special notch was machined along the weld width, reducing the cross-sectional area of the specimen by 30 % (see Fig. 1).

Cyclic fatigue tests on flat specimens were performed under a sinusoidal loading cycle at a frequency of 5 Hz and a stress ratio (R) = 0, in accordance with RD 50-345-82[2]. The fracture surface morphology after mechanical testing was examined using a Tescan Vega-II XMU scanning electron microscope (Carl Zeiss, Czech Republic) and described following the terminology and definitions specified in RD 50-672-88[3].

Results and discussion

During the formation of the VT1-0/VT1-0 welded joint, a narrow weld was obtained with a shape factor (the ratio of penetration depth to weld width) of 2.5 (Fig. 2). Despite the high cooling rates, the grain size in both the fusion zone (FZ) and the heat-affected zone (HAZ) was significantly larger than in the base metal (Table 2). The structure of the FZ corresponds to the as-cast state of titanium: the central region consists of equiaxed polyhedral grains, while the outer regions are composed of larger, elongated grains oriented along the direction of heat removal (Fig. 3, *a*). In the lower portion of the weld, the grains were 1.5—2 times smaller and more equiaxed compared to those in the upper surface area (Fig. 3, *b*).

The microstructure of the as-cast VT1-0 alloy consists of β-transformed grains of about 300 μm, containing parallel α-lamellae 4—10 μm thick, with a length comparable to the size of the prior β-grains. It is known [20; 21], that during the β → α polymorphic transformation, the α-phase grows according to the principle of orientation and dimensional conformity, forming parallel α-lamellae aligned in the same direction. As a result, colonies of α-lamellae form a characteristic intragranular texture within the former β-grains.

At the interface between the heat-affected zone (HAZ) and the base metal, a mixed microstructure was formed, consisting of light-colored polyhedral β-phase grains and α-phase lamellae (Fig. 3, *c*). It should be noted that the α-phase grain size in the HAZ was approximately 1.5—2 times larger than in the base metal (Table 2). Overall, the HAZ material was characterized as partially recrystallized, containing numerous deformed α-phase grains with a high level of residual stresses, which affect crystal orienta-

[1] GOST 6996-66. Welded joints. Methods for determining mechanical properties. Moscow: Standartinform, 2006. (In Russ.).

[2] RD 50-345-82. Methodological guidelines. Calculations and strength tests in mechanical engineering. Methods of cyclic testing of metals. Determination of crack resistance characteristics (fracture toughness) under cyclic loading. Moscow: Publ. Standards, 1983. (In Russ.).

[3] RD 50-672-88. Methodological guidelines. Calculations and strength tests. Classification of types of metal fractures. Moscow: Publ. Standards, 1989. (In Russ.).

Table 2. **Characteristics of the VT1-0/VT1-0 welded joint material**

Таблица 2. Характеристики материала сварного соединения ВТ1-0/ВТ1-0

Specimen	FZ parameters				HAZ parameters				Grain size, μm		
	l, mm	$HV_{0.05}$			*l*, mm	$HV_{0.05}$			Base metal	HAZ	FZ
		max	min	average		max	min	average			
1	1,2	370	210	280	0,75	280	195	230	20	40	300
2	1,2	275	175	230	0,70	275	220	247	20	50	300

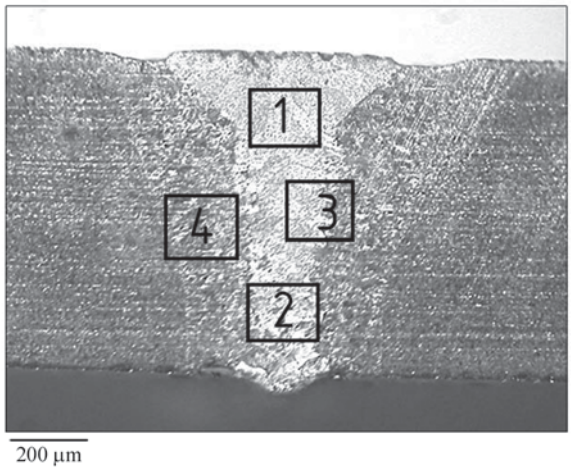

Fig. 2. Macrostructure of the VT1-0/VT1-0 welded joint

Рис. 2. Макроструктура сварного соединения ВТ1-0/ВТ1-0

tion, promote texture formation, and determine the specific features of the structure formation in the weld metal itself (Fig. 3, *d*).

The examination showed that, despite shielding protection against gas absorption, the weld structure contained small micropores about 2—3 μm in size, which can be observed in the micrograph of a local area of the chevron fracture (Fig. 7, *b*). It should be noted that their number is insignificant, and they do not form critical clusters within the microvolumes of the weld metal and, overall, have no effect on the strength characteristics of the welded joint (Table 3). VT1-0, being a single-phase α-alloy, contains a small amount of secondary β-phase, which appears as thin lamellae along the α-grain boundaries. The two-phase structure causes a nonuniform microhardness distribution, where minimum values correspond to the β-phase and maximum to the α-phase [22]. As shown above, the weld metal exhibits a mixed microstructure in which β-phase—enriched regions, upon rapid solidification from the melt, attain high strength. This leads to an overall increase in the average microhardness across the weld width, reaching its maximum in the cast microstructure of the weld metal [23]. At the same time, the refinement of the formed phases contributed to a greater scatter of microhardness values along the measurement line. The averaged microhardness distribution is presented in Fig. 4.

Tensile test results showed that, despite minor internal porosity, the weld metal exhibited high strength (Table 3), significantly exceeding that of the base alloy. The fracture surface morphology after static tension corresponded to ductile failure (Fig. 5, *a*, *b*). The fracture surface of the weld metal contained dimples of varying depth and isolated regions of cellular relief—clusters of small, flat dimples resembling a honeycomb pattern (Fig. 5, *b*), typical for the fracture of cast alloys. This morphology indicates a limited degree of local plastic deformation at failure, but still belongs to the ductile fracture mode, characteristic of plastic materials [20; 24].

During cyclic testing of VT1-0/VT1-0 welded joint specimens at a stress ratio of $\sigma/\sigma_в \geq 0.72$, fracture occurred not along the weld metal but within the base metal. In this case, considerable plastic deformation was observed, accompanied by the formation of a neck during the final loading cycles. This phenomenon is explained by the fact that the VT1-0 alloy exhibits cyclic softening behavior [18].

The fracture surfaces of all specimens displayed characteristic features of fatigue fracture — distinct surface regions differing in morphology, including the crack initiation area, fatigue striations, and ridges representing traces of coalescence of separately initiated neighboring cracks propagating in the same direction, usually from the initiation site. In addition, final fracture zones with features of ductile failure were identified. The fracture surface morphology of VT1-0/VT1-0 welded joint specimens is shown in Fig. 6.

Table 3. **Mechanical test results for VT1-0/VT1-0 welded joint specimens**

Таблица 3. Результаты механических испытаний образцов сварного соединения ВТ1-0/ВТ1-0

Specimen	Material	Tensile test		Fatigue test		
		Fracture location	σ_u, MPa	Number of cycles	σ, MPa	σ/σ_u*
1	Base metal	–	500	Not determined		
2	Weld metal	Weld metal	620	5770	433	0.7
3	Weld metal	Weld metal	660	485856	257	0.4

* Specimens were compared at equal ratios of the maximum cyclic stress (σ) to the ultimate tensile strength (σ_u) determined in tensile tests.

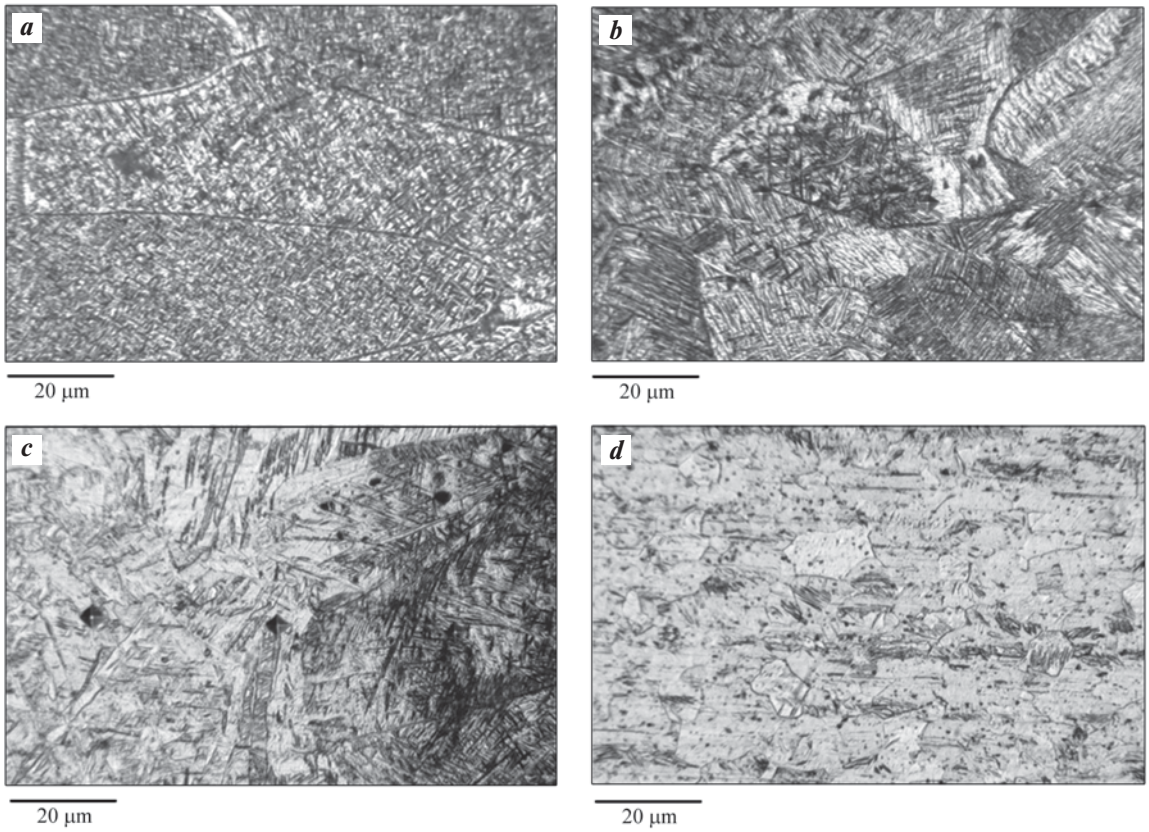

Fig. 3. Microstructure of the VT1-0/VT1-0 welded joint

a – upper part of the fusion zone (area *1* in Fig. 2); ***b*** – root of the fusion zone (area *2* in Fig. 2); ***c*** – boundary between FZ and HAZ (area *3* in Fig. 2); ***d*** – heat-affected zone (area *4* in Fig. 2)

Рис. 3. Микроструктура сварного соединения ВТ1-0/ВТ1-0

a – верхняя часть ЗСШ (зона *1* на рис. 2); ***b*** – корень ЗСШ (зона *2* на рис. 2); ***c*** – граница ЗСШ и ЗТВ (зона *3* на рис. 2); ***d*** – ЗТВ (зона *4* на рис. 2)

Fracture in the crack-initiation regions is brittle and feather-like, propagating along several directions. While the overall direction of fatigue crack growth is preserved, it changes in neighboring grains (Fig. 7, *a*). This behavior is governed by the lamellar α-phase morphology in the weld metal: smooth, polished facets alternate with relief steps that might be mistaken for cleavage, although they are, in fact, the lateral surfaces of α-lamellae.

In the vicinity of micropores, local areas of chevron fracture were observed (arrowed in Fig. 7, *b*). This fea-

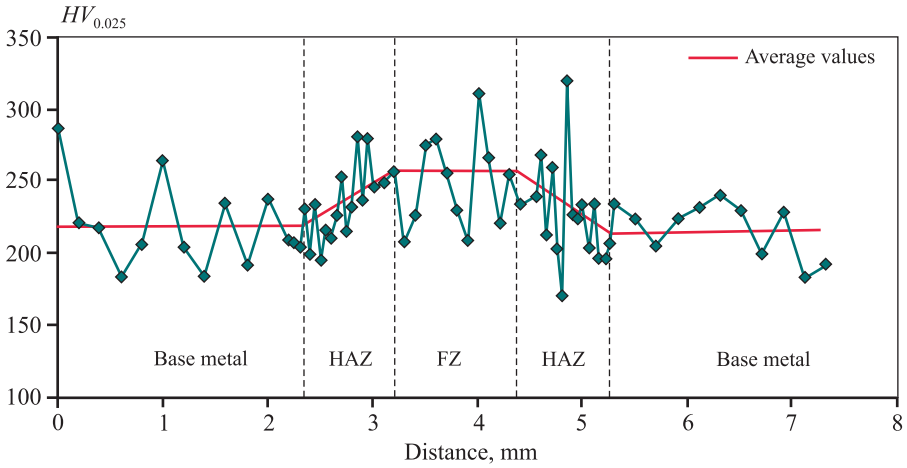

Fig. 4. Variation of microhardness across the width of the VT1-0/VT1-0 welded joint

Рис. 4. Характер изменения микротвердости по ширине сварного соединения ВТ1-0/ВТ1-0

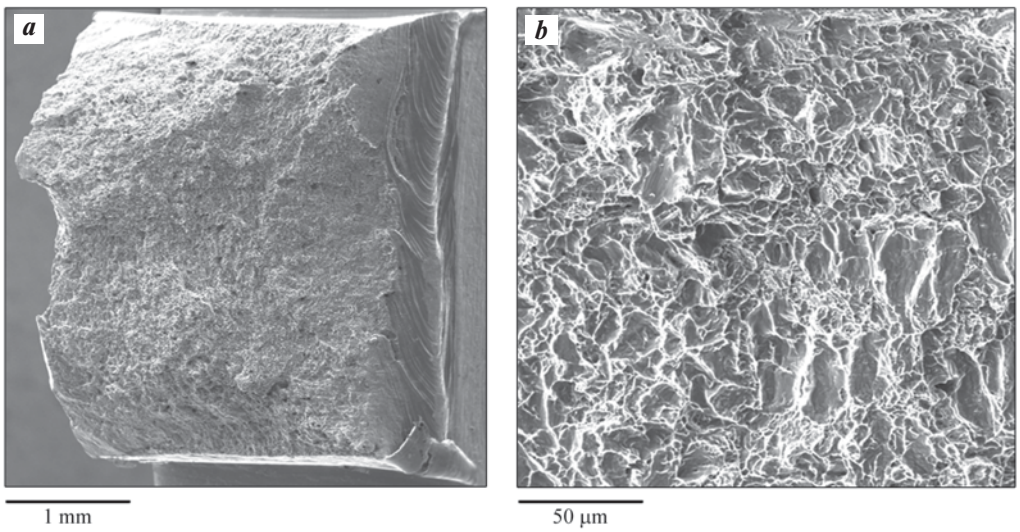

Fig. 5. Macro- (***a***) and micro- (***b***) relief of the fracture surfaces of a VT1-0/VT1-0 welded joint specimen after tensile testing

Рис. 5. Макро- (***a***) и микро- (***b***) рельеф поверхности разрушения образца сварного соединения ВТ1-0/ВТ1-0 после статического растяжения

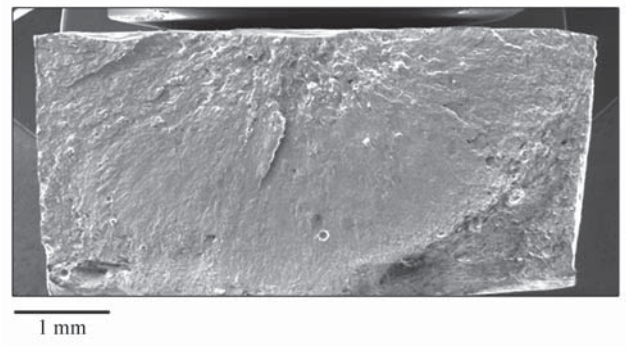

Fig. 6. Macroscopic fracture surface of a VT1-0/VT1-0 welded joint specimen at a maximum cyclic load of 265 MPa

Рис. 6. Макрорельеф поверхности разрушения образца сварного соединения ВТ1-0/ВТ1-0 при максимальной нагрузке цикла 265 МПа

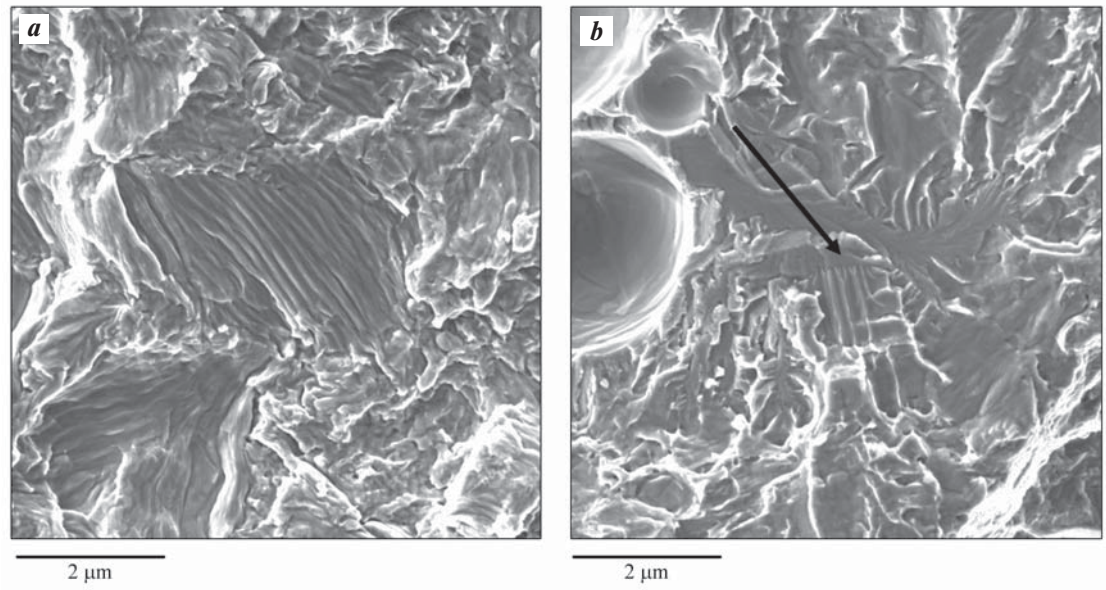

Fig. 7. Macroscopic fracture surface of a VT1-0 alloy specimen
a – change in fatigue crack propagation direction near the initiation site
b – microregion of a chevron fracture near a micropore (indicated by an arrow)

Рис. 7. Микрорельеф поверхности разрушения образца сплава ВТ1-0
a – изменение направления роста усталостной трещины вблизи очага
b – микроучасток шевронного излома вблизи микропоры (отмечен стрелкой)

ture indicates limited plastic deformation and forms under tension with bending in regions of unstable crack growth or during brittle transgranular fatigue fracture. The pores deflect the path of fatigue cracks, which appears as changes in the orientation of fatigue striations. Within initiation zones, isolated areas of ductile fatigue fracture with striations and plateaus, as well as segments of intergranular fatigue crack growth, are present.

Analysis of fracture-surface relief after fatigue tests at different maximum cyclic stresses showed that, at a maximum cyclic stress of 264 MPa, the final rupture zone occupied 35 vol. % of the specimen cross-section. Under these conditions, the area ratio of the fatigue-fracture zone to the final-rupture zone increased to 1.9. In all examined specimens, the final rupture zones exhibited a dimpled fracture with relatively deep dimples, indicating high fracture energy.

As the maximum cyclic stress increased, the fraction of the final rupture zone in the cross-section increased as expected; at a maximum cyclic stress of 425 MPa, these zones occupied 55 vol. %. This finding indicates a substantial contribution of the final rupture zone to the strength of titanium alloy specimens with welded joints under fatigue loading. Since a dimpled fracture corresponds to relatively high fracture energy, the specimens that endured a greater number of cycles were those in which the volume of material involved in fatigue crack growth was about half that of the final rupture zone.

Conclusions

1. Precision narrow-jet air—plasma cutting with PMVR-5.3 torches is suitable for joint preparation, delivering high cut accuracy and surface quality while increasing the absorption coefficient — and, consequently, weld penetration and overall laser-welding efficiency.

2. Continuous-wave CO_2 laser welding of VT1-0/VT1-0 produces a narrow weld whose structure corresponds to the as-cast state of the alloy. The central weld region contains large equiaxed grains that become elongated along the heat-flow direction toward the boundaries and decrease in size toward the root compared with the surface region. The weld microstructure comprises light polyhedral grains and α-phase lamellae; in the HAZ, the α-phase grain size is 1.5—2.0 times larger than in the base metal.

3. Shielding does not completely eliminate fine micropores in the weld metal, which leads to a nonuniform microhardness distribution. Nevertheless, owing to the fine-lamellar α-phase morphology, the average

microhardness in the weld metal is somewhat higher than in the base metal. Tensile tests show that, despite minor porosity, the weld metal exhibits high strength, significantly exceeding that of the base alloy, and the fracture surface morphology corresponds to ductile failure.

4. Under cyclic loading, VT1-0/VT1-0 specimens fracture in the base metal rather than in the weld metal. With increasing maximum cyclic stress, the fraction of the final rupture zone increases, indicating its substantial contribution to the strength of welded titanium alloy specimens under fatigue loading.

5. The combined use of precision narrow-jet air—plasma cutting and continuous-wave CO_2 laser welding enables the fabrication of VT1-0/VT1-0 welded joints with high efficiency and strength comparable to the parent material.

References

1. Aleksandrov A.V., Lednov S.V., Davydkina E.A. State of the affairs in the titanium industry and development prospects. *Tekhnologiya legkikh splavov*. 2021;(2):76—81. (In Russ.).
https://doi.org/10.24412/0321-4664-2021-2-76-81
Александров А.В., Леднов С.В., Давыдкина Е.А. Состояние дел в титановой отрасли и перспективы развития. *Технология легких сплавов*. 2021;(2):76—81. https://doi.org/10.24412/0321-4664-2021-2-76-81
2. Kishawy H.A., Hosseini A. Machining difficult-to-cut materials. Chapter: Titanium and titanium alloys. Springer: Ser. Materials forming, machining and tribology, 2019.
https://doi.org/10.1007/978-3-319-95966-5_3
3. Bubnov V.A., Knyazev A.N. Titanium and its alloys in mechanical engineering. *Bulletin of Kurgan State University*. 2016;(3):92—96. (In Russ.).
Бубнов В.А., Князев А.Н. Титан и его сплавы в машиностроении. *Вестник Курганского государственного университета*. 2016;(3):92—96.
4. Pultsin N.M. Interaction of titanium with gases. Moscow: Metallurgiya, 1969. 213 p. (In Russ.).
Пульцин Н.М. Взаимодействие титана с газами. М.: Металлургия, 1969. 213 с.
5. Ilyin A.A. Mechanism and kinetics of phase and structural transformations in titanium alloys. Moscow: Nauka, 1994. 304 p. (In Russ.).
Ильин А.А. Механизм и кинетика фазовых и структурных превращений в титановых сплавах. М.: Наука, 1994. 304 с.
6. Germain L., Gey N., Humbert M., Vo P., Jahazi M., Bocher Ph. Texture heterogeneities induced by subtransus processing of near α titanium alloys. *Acta Materialia*. 2008;56(15):4298—4308.
7. Groche P., Wohletz S., Brenneis M., Pabst P., Resch F. Joining by forming — A review on joint mechanisms, applications and future trends. *Journal of Materials Processing Technology*. 2014;212(10):1972—1994.
8. Paton B.E., Shelyagin V.D., Akhonin S.V., Topolskii V.F., Khaskin V.Yu., Petrichenko I.K., Bernatskii A.V., Mishchenko R.N., Siora A.V. Laser welding of titanium alloys. *Avtomaticheskaya svarka*. 2009;(10):35—39. (In Russ.).
Патон Б.Е., Шелягин В.Д., Ахонин С.В., Тополь-ский В.Ф., Хаскин В.Ю., Петриченко И.К., Бернацкий А.В., Мищенко Р.Н., Сиора А.В. Лазерная сварка титановых сплавов. *Автоматическая сварка*. 2009;(10):35—39.
9. Sokolov M., Salminen A. Improving laser beam welding efficiency. *Engineering*. 2014;6(09):559—571.
https://doi.org/10.4236/ENG.2014.69057
10. Akman E., Demir A., Canel T., Sınmazçelik T. Laser welding of Ti6Al4V titanium alloys. *Journal of Materials Processing Technology*. 2009;209(8):3705—3713.
https://doi.org/10.1016/j.jmatprotec.2008.08.026
11. Zhang Y., Sun D., Gu X., Li H. A hybrid joint based on two kinds of bonding mechanisms for titanium. *Materials Letters*. 2016;15(185):152—155.
12. Riccardi G., Cantello M. Laser material interactions: Absorption coefficient in welding and surface treatment. *CIRP Annals — Manufacturing Technology*. 1994;1:171—175.
https://doi.org/10.1016/j.optlastec.2012.03.025
13. Sokolov M., Salminen A. Experimental investigation of the influence of edge morphology in high power fiber laser welding. *Physics Procedia*. 2012;39:33—42.
https://doi.org/10.1016/j.phpro.2012.10.0115
14. Covelli L., Jovane F., De Lori L., Tagliaferri V. Laser welding of stainless steel: Influence of the edges morphology. *CIRP Annals — Manufacturing Technology*. 1988;37:545—548.
15. Sokolov M., Salminen A., Somonov V., Kaplan A.F. Laser welding of structural steels: Influence of the edge roughness level. *Optics & Laser Technology*. 2012;44(7):2064—2071.
16. Pykin Yu.A., Anakhov S.V., Matushkin A.V. Plasmatron: Patent 2754817 (RF). 2021. (In Russ.).
Пыкин Ю.А., Анахов С.В., Матушкин А.В. Плазмотрон: Патент 2754817 (РФ). 2021.

17. Anakhov S.V., Guzanov B.N., Matushkin A.V., Michurov N.S. On compliance with regulatory standards for cutting quality in the production of welded joints. *Competency*. 2024;(5):56—62. (In Russ.).
https://doi.org/10.24412/1993-8780-2024-5-56-62
Анахов С.В., Гузанов Б.Н., Матушкин А.В., Мичуров Н.С. О соблюдении регламентных норм на качество резки при производстве сварных соединений. *Компетентность*. 2024;(5):56—62.
https://doi.org/10.24412/1993-8780-2024-5-56-62
18. Ilyin A.A., Kolachev B.A., Polkin I.S. Titanium alloys. Composition, structure, properties. Moscow: VILS–MATI, 2009. 520 p. (In Russ.).
Ильин А.А., Колачев Б.А., Полькин И.С. Титановые сплавы. Состав, структура, свойства: Справочник. М.: ВИЛС—МАТИ, 2009. 520 с.
19. Illarionov A.G., Popov A.A. Technological and operational properties of titanium alloys. Ekaterinburg: Ural University Press, 2014. 137 p. (In Russ.).
Илларионов А.Г., Попов А.А. Технологические и эксплуатационные свойства титановых сплавов. Екатеринбург: Изд-во Уральского университета, 2014. 137 с.
20. Klevtsov G.V., Botvina L.R., Klevtsova N.A., Limar L.V. Fractodiagnostics of destruction of metal materials and structures. Moscow: MISIS, 2007. 264 p. (In Russ.).
Клевцов Г.В., Ботвина Л.Р., Клевцова Н.А., Лимарь Л.В. Фрактодиагностика разрушения металлических материалов и конструкций. Учеб. пос. для вузов. М.: МИСИС, 2007. 264 с.
21. Gnusov S.F., Klimenov V.A., Alkhimov Yu.V., Budnitsky A.D., Orishich A.M., Cherepanov A.N., Afonin Yu.V. Formation of the structure of titanium and corrosion-resistant steel during laser welding. *Welding International*. 2012;(1):17—22.
22. Ivanov M.B., Kolobov Yu.R., Manokhin S.S., Golosov E.V. Investigation of the structural and phase state of medical titanium alloys by modern methods of analytical electron microscopy. *Indusrial laboratory. Diagnostics of materials*. 2012;78(1):43—54. (In Russ.).
Иванов М.Б., Колобов Ю.Р., Манохин С.С., Голосов Е.В. Исследование структурно-фазового состояния медицинских титановых сплавов современными методами аналитической электронной микроскопии. *Заводская лаборатория. Диагностика материалов*. 2012;78(1):43—54.
23. Polkin I.S., Egorova Yu.B., Davydenko L.V. Alloying, phase composition and mechanical properties of titanium alloys. *Tekhnologiya legkikh splavov*. 2022;(2): 4—13. (In Russ.).
https://doi.org/10.24412/0321-4664-2022-2-4-13
Полькин И.С., Егорова Ю.Б., Давыденко Л.В. Легирование, фазовый состав и механические свойства титановых сплавов. *Технология легких сплавов*. 2022;(2):4—13.
https://doi.org/10.24412/0321-4664-2022-2-4-13
24. Alkhimov Yu.V., Gnyusov S.F., Kapranov B.I., Klimenov V.A., Orishich A.M. Investigation of laser-welded titanium and stainless steel specimens using digital radiography methods. *Russian Journal of Nondestructive Testing*. 2012;48(4):238—244.
https://doi.org/10.1134/S106183091204002X

Information about the authors

Sergey V. Anakhov – Dr. Sci. (Eng.), Associate Professor, Head of the Department of mathematical and natural sciences, Russian State Vocational Pedagogical University (RSVPU).
https://orcid.org/0000-0003-1460-6305
E-mail: sergej.anahov@rsvpu.ru

Boris N. Guzanov – Dr. Sci. (Eng.), Professor, Head of the Department of engineering and vocational training in mechanical engineering and metallurgy, RSVPU.
https://orcid.org/0000-0001-5698-0018
E-mail: guzanov_bn@mail.ru

Nikolay S. Michurov – Senior Lecturer, Department of fire safety in construction, Ural Institute of State Fire Service of EMERCOM of Russia.
https://orcid.org/0000-0003-1775-6181
E-mail: n.michurov@ya.ru

Информация об авторах

Сергей Вадимович Анахов – д.т.н., доцент, заведующий кафедрой математических и естественно-научных дисциплин Российского государственного профессионально-педагогического университета (РГППУ).
https://orcid.org/0000-0003-1460-6305
E-mail: sergej.anahov@rsvpu.ru

Борис Николаевич Гузанов – д.т.н., проф., заведующий кафедрой инжиниринга и профессионального обучения в машиностроении и металлургии РГППУ.
https://orcid.org/0000-0001-5698-0018
E-mail: guzanov_bn@mail.ru

Николай Сергеевич Мичуров – ст. преподаватель кафедры пожарной безопасности в строительстве Уральского института ГПС МЧС России.
https://orcid.org/0000-0003-1775-6181
E-mail: n.michurov@ya.ru

Contribution of the authors

S.V. Anakhov – formulation of the research objective and tasks, preparation of the manuscript, and formulation of conclusions.

B.N. Guzanov – scientific supervision, development of the main concept, and revision of the manuscript and conclusions.

N.S. Michurov – preparation and execution of experiments, calculations, and manuscript preparation.

Вклад авторов

С.В. Анахов – постановка цели и задачи исследования, подготовка текста статьи, формулировка выводов.

Б.Н. Гузанов – научное руководство, формирование основной концепции, корректировка текста и выводов.

Н.С. Мичуров – подготовка и проведение экспериментов, осуществление расчетов, подготовка текста статьи.

The article was submitted 11.09.2024, revised 01.10.2024, accepted for publication 06.11.2024

Статья поступила в редакцию 11.09.2024, доработана 01.10.2024, подписана в печать 06.11.2024

UDC 621.762
https://doi.org/10.17073/0021-3438-2025-4-62-76

Research article
Научная статья

Effect of alloying with a second components on the biocompatibility and mechanical properties of Ti–Mo alloys

A.S. Gornakova[1], A. Korneva Surmacz[2], K.M. Novruzov[3], D.G. Shaisultanov[4], N.S. Afonikova[1], B.B. Straumal[1], A.I. Tyurin[5], V.A. Tyurin[5], G.S. Davdian[1,6]

[1] **Osipyan Institute of Solid State Physics of the Russian Academy of Sciences**
2 Akademik Osipyan Str., Chernogolovka, Moscow Region 142432, Russia

[2] **Aleksander Krupkowski Institute of Metallurgy and Materials Science of the Polish Academy of Sciences**
25 Reymonta Str., Krakow 30-059, Poland

[3] **N.N. Blokhin National Medical Research Center of Oncology of the Ministry of Health of the Russia**
24 Kashirskoye Highway, Moscow 115522, Russia

[4] **Saint Petersburg Marine Technical University**
3 Lotsmanskaya Str., Saint Petersburg 190121, Russia

[5] **Tambov State University n.a. G.R. Derzhavin**
33 Internatsionalnaya Str., Tambov 392000, Russia

[6] **National University of Science and Technology "MISIS"**
1 Bld, 4 Leninskiy Prosp., Moscow 119049, Russia

✉ Alena S. Gornakova (alenahas@issp.ac.ru)

Abstract: This paper presents the results of a study on two titanium-based alloys — Ti–10wt.%Mo and Ti–15wt.%Mo — aimed at assessing their potential for use as base materials in implantable medical devices for osteosynthesis. The alloy samples were examined in three conditions: as-fabricated, after annealing at 1000 °C, and after high-pressure torsion. The microstructure of the alloys was analyzed using scanning electron microscopy and *X*-ray diffraction. The Young's modulus, microhardness, and nanohardness values were measured, and the effect of the alloys on the viability and surface adhesion of human multipotent mesenchymal stromal cells during *in vitro* incubation was investigated. Comparative analysis of the obtained results revealed that the annealed Ti–15wt.%Mo alloy sample is the most promising candidate for orthopedic applications, as it exhibits an optimal combination of good biocompatibility, enhanced stimulation of cell adhesion, and relatively low microhardness (283 HV) and Young's modulus (106 GPa).

Keywords: titanium–molybdenum alloys, biocompatibility, cell adhesion, phase transformations, high-pressure torsion, nanoindentation, heat treatment.

Acknowledgements: This study was supported by the Russian Science Foundation, project No. 24-22-00222, https://rscf.ru/project/24-22-00222/

The authors express their sincere gratitude to the Shared-Use Center of the Institute of Solid State Physics, Russian Academy of Sciences (ISSP RAS), for providing access to *X*-ray diffraction and phase analysis facilities.

For citation: Gornakova A.S., Korneva Surmacz A., Novruzov K.M., Shaisultanov D.G., Afonikova N.S., Straumal B.B., Tyurin A.I., Tyurin V.A., Davdian G.S. Effect of alloying with a second components on the biocompatibility and mechanical properties of Ti–Mo alloys. *Izvestiya. Non-Ferrous Metallurgy.* 2025;31(4):62–76. https://doi.org/10.17073/0021-3438-2025-4-62-76

Влияние легирования второй компонентой на биосовместимость и механические свойства сплавов Ti–Mo

А.С. Горнакова[1], А. Корнева Сурмач[2], К.М. Новрузов[3], Д.Г. Шайсултанов[4], Н.С. Афоникова[1], Б.Б. Страумал[1], А.И. Тюрин[5], В.А. Тюрин[5], Г.С. Давдян[1,6]

[1] **Институт физики твердого тела им. Ю.А. Осипьяна Российской академии наук**
Россия, 142432, Московская обл., г. Черноголовка, ул. Академика Осипьяна, 2

[2] **Институт металлургии и материаловедения им. Александра Крупковского Польской академии наук**
Польша, 30-059, Краков, ул. Реймонта, 25

[3] **Национальный медицинский исследовательский центр онкологии им. Н.Н. Блохина Минздрава России**
Россия, 115522, г. Москва, Каширское шоссе, 24

[4] **Санкт-Петербургский государственный морской технический университет**
Россия, 190121, г. Санкт-Петербург, ул. Лоцманская, 3

[5] **Тамбовский государственный университет им. Г.Р. Державина**
Россия, 392000, г. Тамбов, ул. Интернациональная, 33

[6] **Национальный исследовательский технологический университет «МИСИС»**
Россия, 119049, г. Москва, Ленинский пр-т, 4, стр. 1

✉ Алена Сергеевна Горнакова (alenahas@issp.ac.ru)

Аннотация: Представлены результаты исследования двух сплавов на основе титана: Ti–10мас.%Mo и Ti–15мас.%Mo – для оценки перспектив их использования в качестве основы имплантируемых медицинских изделий для остеосинтеза. Образцы сплавов были изучены в трех состояниях: исходном (после изготовления), после отжига при температуре 1000 °C и после кручения под высоким давлением. Была исследована микроструктура сплавов с помощью сканирующий электронной микроскопии и рентгеноструктурного анализа. Были измерены значения модуля Юнга и микро- и нанотвердости сплавов, а также изучено влияние сплавов при инкубации *in vitro* на жизнеспособность и поверхностную адгезию мультипотентных мезенхимальных стромальных клеток человека. Сравнительный анализ характеристик исследованных образцов показал, что наиболее перспективным для использования в качестве основы ортопедических изделий является отожженный образец сплава Ti–15мас.%Mo, который оптимально сочетает хорошую биосовместимость, активную стимуляцию клеточной адгезии и низкие значения микротвердости (283 HV) и модуля Юнга (106 ГПа).

Ключевые слова: сплавы титан–молибден, биосовместимость, клеточная адгезия, фазовые превращения, кручение под высоким давлением, наноиндентирование, термообработка.

Благодарности: Исследование выполнено за счет гранта Российского научного фонда № 24-22-00222, https://rscf.ru/project/24-22-00222/

Выражаем глубокую признательность ЦКП ИФТТ РАН за возможность проведения рентгеноструктурного и фазового анализов.

Для цитирования: Горнакова А.С., Корнева Сурмач А., Новрузов К.М., Шайсултанов Д.Г., Афоникова Н.С., Страумал Б.Б., Тюрин А.И., Тюрин В.А., Давдян Г.С. Влияние легирования второй компонентой на биосовместимость и механические свойства сплавов Ti–Mo. *Известия вузов. Цветная металлургия*. 2025;31(4):62–76. https://doi.org/10.17073/0021-3438-2025-4-62-76

Introduction

Metallic implants play a dominant role as structural biomaterials in reconstructive surgery, particularly in orthopedics, and in recent years have also been applied to non-osseous tissues such as blood vessels. These implants are continuously being modernized and improved, and numerous review papers have been published on the materials currently available [1—4]. Among these, β-titanium alloys occupy a special position as promising biomaterials intended to replace first-generation α-titanium alloys, commercially pure titanium, and the VT6 alloy.

Although titanium alloys have stood the test of time and are now widely used for various orthopedic and dental purposes [1], ongoing research seeks to modify their composition and surface characteristics to develop materials with the most favorable combination of mechanical and chemical properties. Owing to the unique properties of titanium, the elastic modulus of titanium alloys can be tailored to approach that of bone, primarily through alloying with elements that alter the volume fractions of structural phases in the material [2].

The interest in Ti—Mo alloys [5—9] as promising materials for biomedical applications has persisted for more than three decades. Alloying titanium with molybdenum imparts high strength and a low elastic modulus to the material.

The choice of Ti—10wt.%Mo and Ti—15wt.%Mo alloys for this study was guided by the following considerations. First, titanium is characterized by extremely low toxicity to the human body, high corrosion resistance, and resistance to biodegradation, as confirmed by the long-standing clinical use of titanium and its alloys in medicine. Second, molybdenum is a β-phase stabilizing element with low toxicity; its content in the range of 15—20 wt. % can reduce the elastic modulus and align the mechanical properties of the alloy with those of human bone tissue. An important goal of implant—tissue interaction is to prevent corrosion or degradation, bone destruction, physiological changes, or implant instability. Titanium alloys are biologically inert; however, modification of surface morphology (roughness), wettability, and other surface parameters can enhance the adhesion of connective tissue cells, particularly osteogenic cells. Titanium and its alloys spontaneously form a very stable oxide layer that separates the alloy from adjacent tissues and provides excellent corrosion resistance [10].

This study addresses not only the improvement of the mechanical properties of the investigated alloys through various processing methods but also the evaluation of how these treatments affect the biocompatibility of Ti—Mo alloys.

One of the material processing techniques capable of significantly altering both the mechanical properties [11—13] and the microstructure and phase composition [13; 14], of the alloy is severe plastic deformation [15—21]. In this work, one such technique — high-pressure torsion (HPT) — was applied to evaluate the influence of this processing method on the biological activity of the alloys.

The aim of this study is to investigate the effect of alloying element content and processing method (heat treatment and high-pressure torsion) on the mechanical properties and biocompatibility of Ti—10 wt. % Mo and Ti—15 wt. % Mo alloys.

Materials and methods

Ingots of Ti—10wt.%Mo and Ti—15wt.%Mo alloys were produced by vacuum arc melting of the components in a high-purity argon atmosphere using a water-cooled copper mold. The purity of alloying elements was at least 99.9 wt. %. To ensure chemical homogeneity, the ingots were inverted and remelted at least ten times. The melting process was carried out using an Arc-Melting AM200 unit (Bodelshausen, Germany). The resulting ingots, 10 mm in diameter, were cut into discs 0.7 mm thick. The first series of samples was studied in the as-fabricated condition, the second after heat treatment (HT) at 1000 °C for 24 h, and the third after HT followed by high-pressure torsion (HPT). HPT processing was performed at room temperature: five revolutions under a pressure of 7 GPa at a rotation rate of 1 rpm using a computer-controlled Bridgman-type anvil apparatus (W. Klement GmbH, Lang, Austria). After HPT, the sample thickness was 0.35 mm. The microstructure and phase composition of all samples were analyzed. The phase composition, phase fractions, and lattice parameters were determined using *X*-ray diffraction (XRD). Diffraction patterns were recorded on a SmartLab diffractometer (Rigaku Corporation, Japan) with Cu$K_{\alpha 1+\alpha 2}$ radiation (λ = 0.15419 nm). The lattice parameters were calculated using the PowderCell 2.4 software package (PowderCell for Windows, Version 2.4, 08.03.2000, Werner Kraus & Gert Nolze, BAM, Berlin). The microstructure of the samples was examined using a high-resolution scanning electron microscope (SEM) Quanta 3D FEG (Thermo Fisher FEI Company, USA) equipped with an additional FIB ion column and integrated EDAX Trident system.

Nanoindentation of the sample surface was performed using a Hysitron TI 950 TriboIndenter (Bruker, USA) equipped with a Berkovich indenter. Measurements were carried out along the sample diameter (70 ± 10 indents) at a constant loading rate of 40 mN/s. Before testing, the sample surfaces were polished with 1 μm diamond paste. The numerical values of nanohardness (H) and Young's modulus (E) were determined using the Oliver—Pharr method based on characteristic P—h curves [21—23]. Microhardness was measured with an ITV-1-MS tester (LLC Metotest, Russia) equipped with an MC-5.3 camera and LOMO-Microsystems MCview software. The average

microhardness values were obtained from ten indentations under a load of 100 g.

Human multipotent mesenchymal stromal cells (MSCs) obtained from the collection of the N.N. Blokhin National Medical Research Center of Oncology were used as a biological model. The cells were suspended in RPMI-1640 growt.h medium (PanEko, Russia) supplemented with 10 % fetal bovine serum, 1 % penicillin, and 2 mM L-glutamine (PanEko, Russia). The cell concentration was 132000 cells/mL.

The alloy samples were ultrasonically cleaned (Odaservice, Russia) in distilled water at 21 ± 1 °C for 15 min, immersed in 60 % ethanol for 4 h, air-dried under sterile conditions, and then placed individually in the wells of 24-well culture plates (Costar, USA). A 20 μL cell suspension was applied to each sample surface and incubated for 20 min at 37 °C in a 5 % CO_2 atmosphere. For control, an equal volume of cell suspension was placed directly on the well bottom. Then, 2 mL of growt.h medium was added to each well, and incubation continued for 1 and 5 days under the same conditions.

Biocompatibility of the studied alloy samples was assessed by comparing the viability of MSC cultures after 1 day of incubation using the MTT assay. The procedure was performed as described previously [22]. After 4 h of incubation, the supernatant was carefully removed, dimethyl sulfoxide was added to the cell sediment, and the optical density of the resulting solution was measured at 540 nm using a Spark microplate reader (Tecan, Switzerland) against the intact growt.h medium. The alloys were considered biocompatible if their exposure did not result in a statistically significant decrease in cell viability compared with the control.

To evaluate cell adhesion, alloy samples with attached MSCs were treated with Calcein AM solution (Sigma, USA) according to the manufacturer's protocol after 5 days of cultivation. Cells on the sample surfaces were examined using fluorescence microscopy on a LionHeart FX cell imaging system (Perkin Elmer, USA). For quantitative assessment of surface cell adhesion intensity, the alloy samples with adhered cells were transferred to empty wells, and growt.h medium was removed from the control wells. Then, 1 mL of fresh growt.h medium was added to both sample and control wells, and the viability of adhered cells was evaluated using the MTT assay as described above.

Statistical analysis was performed using at least three samples of each alloy type for every parameter. The results for MSC viability and cell adhesion were expressed as mean ± standard deviation based on triplicate measurements. Comparative analysis was carried out using the median criterion, and differences from the control were considered statistically significant at $p < 0.05$.

Results

Microstructure and phase composition of samples in the as-fabricated, annealed, and HPT-processed states

SEM and XRD results were obtained for both investigated alloys in three conditions: as-fabricated (after ingot production), after annealing, and after high-pressure torsion (HPT). The samples in the as-fabricated condition (Fig. 1, *a*, *b*) and after annealing (Fig. 1, *c*, *d*) exhibited coarse-grained polycrystalline structures. It should be noted that the distribution of alloying components was nonuniform (Fig. 1, *a*), and each grain consisted of subgrains with an average size of 100—150 nm.

Significant changes in the microstructure occurred after HPT processing (Fig. 1, *e*, *f*). The grain size could not be determined from the SEM images; however, other structural features, such as shear bands, were clearly visible. On the surface of the Ti—15Mo alloy (Fig. 1, *f*), these bands appear as separate regions, which most likely correspond to differently oriented grains.

Fig. 2 presents the *X*-ray diffraction patterns for both alloys in the three studied states.

Tables 1 and 2 summarize the XRD data, including the phase composition, lattice parameters, and volume fractions of phases in the Ti—10Mo and Ti—15Mo alloys. In all investigated samples, the main phase was the β-Ti phase.

Based on the *X*-ray diffraction analysis, the volume fraction of the β-Ti phase (Fig. 3, *a*) and its lattice parameters (Fig. 3, *b*) were calculated for both alloys in all three conditions. In the as-fabricated and annealed conditions, the samples exhibited coarse-grained structures, and the volume fraction of the β-Ti phase was nearly identical. The lattice parameters of the annealed samples differed significantly from those in the as-fabricated condition due to the enrichment of the β-Ti phase with molybdenum. In the Ti—10wt.%Mo alloy, all molybdenum atoms are incorporated into the β-Ti phase, whereas in the Ti—15wt.%Mo alloy, the excess molybdenum forms a secondary cubic β-Mo phase.

Phase transformations induced by HPT processing altered not only the β-Ti/β-Mo phase ratio but also the

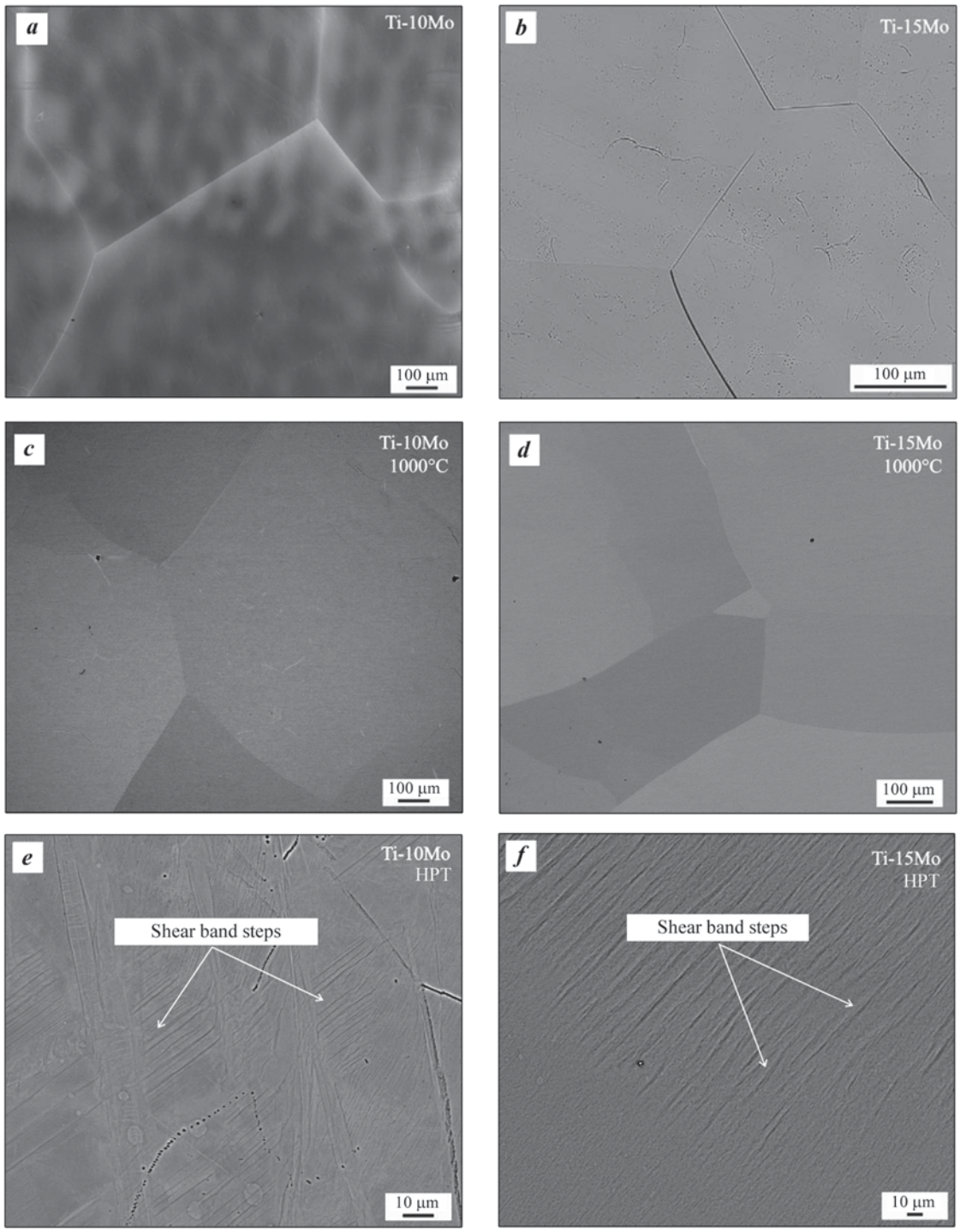

Fig. 1. SEM micrographs of the alloy microstructures

a, ***b*** – as-fabricated; ***c***, ***d*** – after annealing; ***e***, ***f*** – after high-pressure torsion (HPT) processing
a, ***c***, ***e*** – Ti–10Mo alloy; ***b***, ***d***, ***f*** – Ti–15Mo alloy

Рис. 1. СЭМ-изображения микроструктур сплавов

a, ***b*** – в исходном состоянии; ***c***, ***d*** – после отжига, ***e***, ***f*** – после КВД-обработки
a, ***c***, ***e*** – сплав Ti–10Mo; ***b***, ***d***, ***f*** – сплав Ti–15Mo

Table 1. **Phase composition, lattice parameters, and phase fraction for the Ti–10Mo alloy**

Таблица 1. Фазовый состав, параметры решеток и доля фаз для сплава Ti–10Mo

Alloy condition	α			βTi		βMo	
	V, %	*a*, nm	*c*, nm	*V*, %	*a*, nm	*V*, %	*a*, nm
As-fabricated	4	0.2951	0.4688	84	0.3257	12	0.3216
After annealing (1000 °C)	–	–	–	100	0.3275	–	–
After HPT	–	–	–	99.5	0.3259	–	–

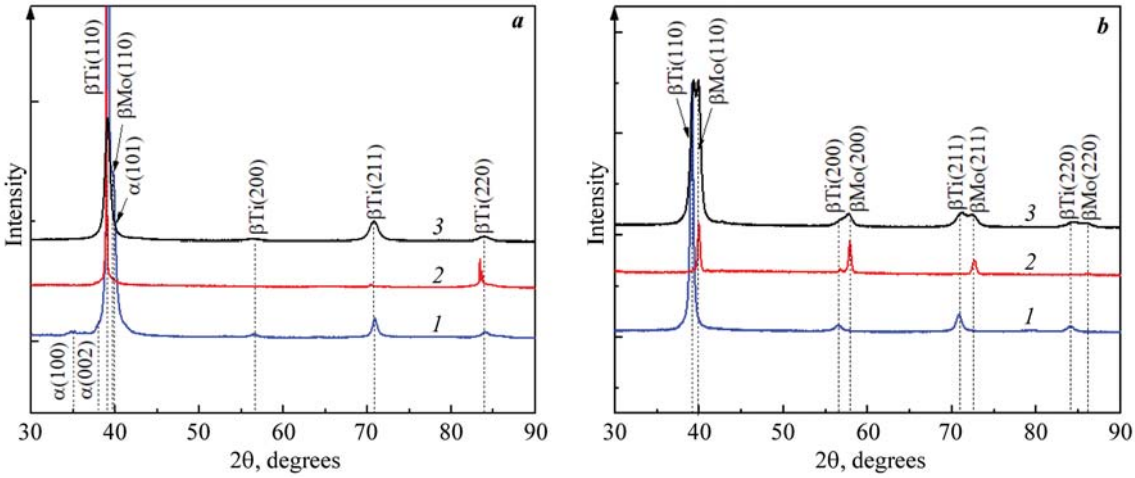

Fig. 2. *X*-ray diffraction patterns of Ti–10Mo and Ti–15Mo alloys in three conditions: as-fabricated (***1***), annealed at $t = 1000$ °C (***2***), and HPT-processed (***3***)
a – Ti–10Mo, ***b*** – Ti–15Mo

Рис. 2. Рентгенограммы образцов сплавов Ti–10Mo и Ti–15Mo в исходном состоянии (***1***), после отжига при $t = 1000$ °C (***2***) и после КВД-обработки (***3***)
a – Ti–10Mo, ***b*** – Ti–15Mo

Table 2. **Phase composition, lattice parameters, and phase fraction for the Ti–15Mo alloy**

Таблица 2. Фазовый состав, параметры решеток и доля фаз для сплава Ti–15Mo

Alloy ondition	βTi		βMo	
	V, %	*a*, nm	*V*, %	*a*, nm
As-fabricated	100	0.3257	–	–
After annealing (1000 °C)	94	0.3246	4	0.3189
After HPT	55	0.3246	45	0.3196

corresponding lattice parameters of the solid-solution phases.

Mechanical properties of the alloys

The microhardness of the studied samples was measured (Fig. 4, *a*), while nanoindentation was used to determine the average values of nanohardness (Fig. 4, *b*) and Young's modulus (Fig. 4, *c*). The dependences of microhardness and nanohardness exhibited similar trends for both alloys. An increase in molybdenum content in the titanium alloy resulted in lower values of these parameters. The microstructure, phase composition, and mechanical properties of the as-fabricated and annealed samples were almost identical. Essentially, annealing at

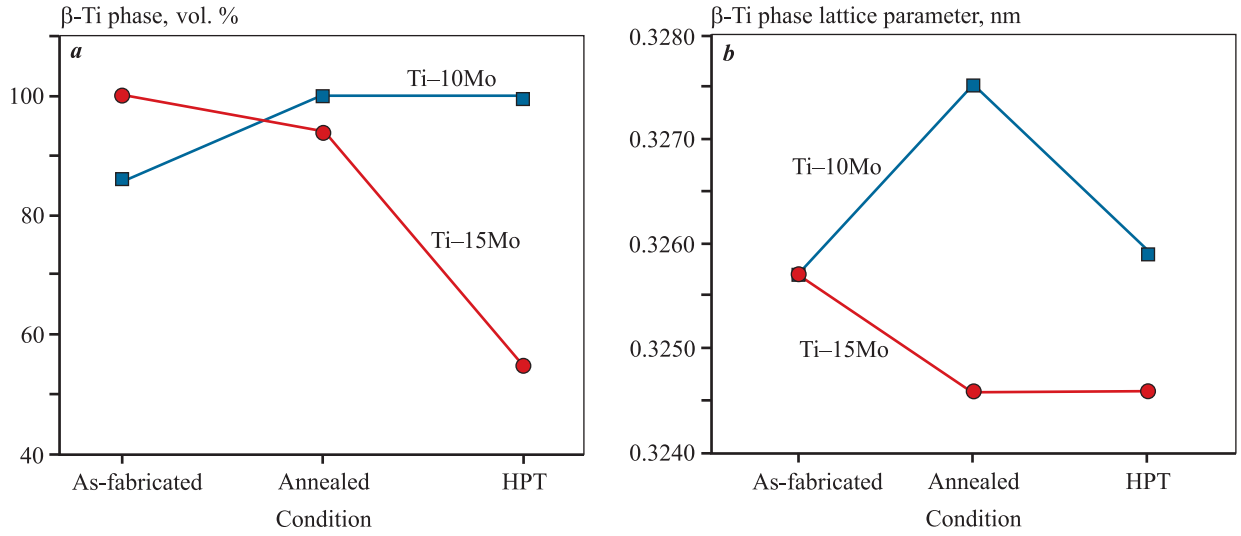

Fig. 3. Volume fraction of the β-Ti phase (***a***) and lattice parameter of the β-Ti phase (***b***) for Ti–10Mo and Ti–15Mo alloys depending on the processing method

Рис. 3. Зависимости объемной доли βTi-фазы (***a***) и параметров решетки βTi-фазы (***b***) для сплавов Ti–10Mo и Ti–15Mo от вида обработки

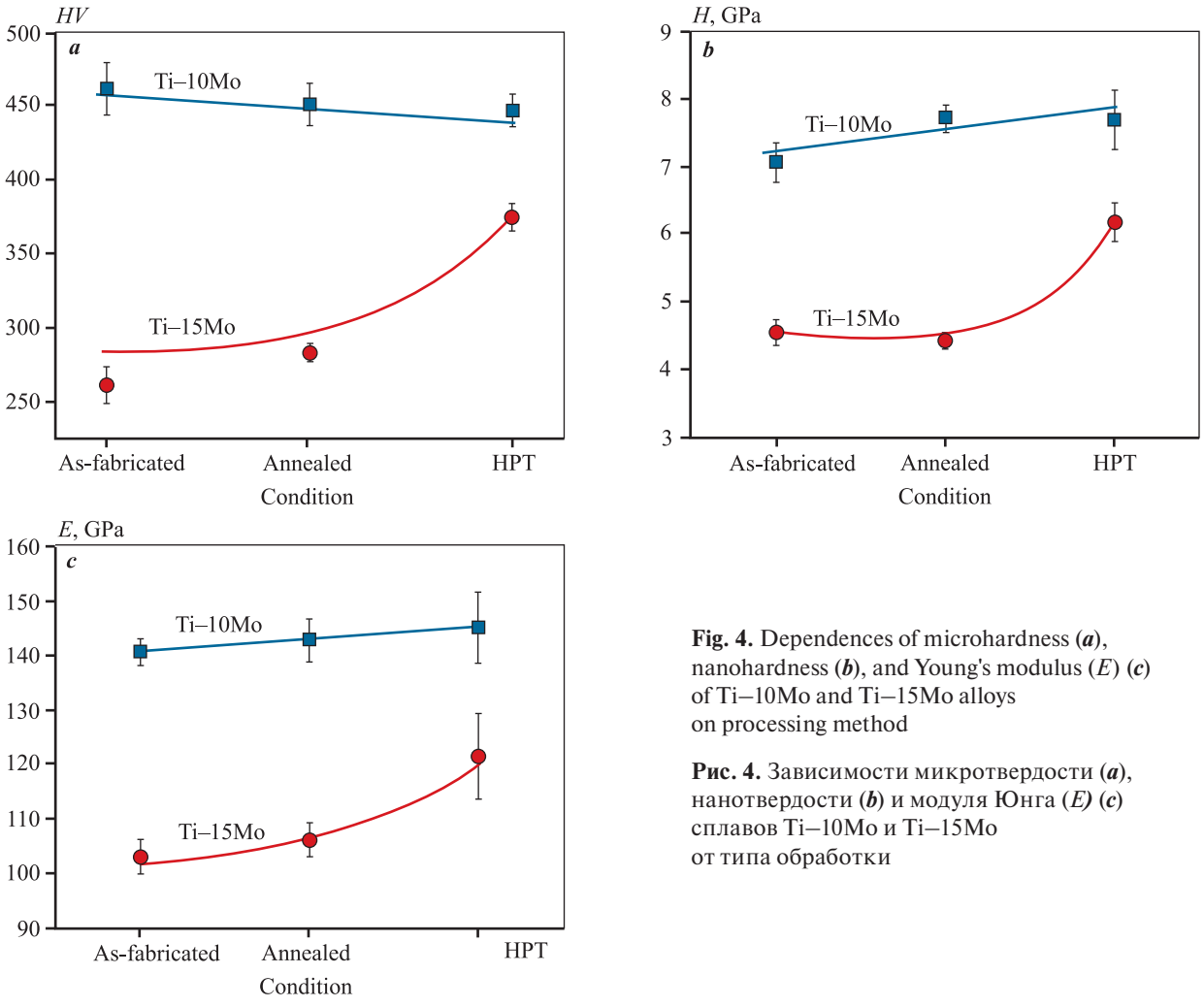

Fig. 4. Dependences of microhardness (***a***), nanohardness (***b***), and Young's modulus (*E*) (***c***) of Ti–10Mo and Ti–15Mo alloys on processing method

Рис. 4. Зависимости микротвердости (***a***), нанотвердости (***b***) и модуля Юнга (*E*) (***c***) сплавов Ti–10Mo и Ti–15Mo от типа обработки

1000 °C served as a homogenization treatment that eliminated chemical and structural inhomogeneities in the samples. It is well known that severe plastic deformation refines the grain size and induces phase transformations in metals and alloys, which consequently alters their mechanical properties. For the Ti—10 Mo alloy, such changes were not observed. It can be assumed that the key factor influencing the mechanical properties of the investigated alloys was the phase transformation induced by HPT processing, specifically the formation of the β-Mo phase in the Ti—15 Mo alloy, which led to changes in the mechanical behavior.

Biocompatibility of the samples and stimulation of cell adhesion

Human multipotent mesenchymal stromal cells (MSCs) were used as a cellular model because, depending on external stimuli, they are capable of differentiating into various connective tissue lineages involved in the formation of bone, cartilage, stroma, muscle, blood vessels, and tendons [23]. These are precisely the types of tissues expected to interact with the developed implants following their placement in osteoreconstructive surgery. To ensure stable osteosynthesis, the metallic implant material must comply with biocompatibility requirements — namely, it should not exert cytotoxic effects upon contact and should promote surface cell adhesion.

Morphologically, MSCs are large polygonal cells measuring approximately 20—50 μm in diameter. They adhere effectively to the matrix surface, maintain viability and proliferative capacity *in vitro*, and are capable of colonizing the surfaces of experimental alloy samples (Fig. 5). Live-cell staining with Calcein AM enables visualization of metabolically active cells through the fluorescence emitted by the cytoplasm of viable cells.

This methodological approach confirmed that the cells adhered to the surfaces of all studied Ti—Mo alloy samples (Fig. 6). The analysis showed that the cells not only adhered actively during co-incubation but also retained their ability to proliferate, forming continuous cell layers on the alloy surfaces. Overall, the degree of cell colonization was comparable among the samples, though cell activity on the surface of the Ti—15Mo alloy was slightly higher than on Ti—10Mo. In contrast, the colonization of the Ti—10Mo surface after HPT processing was somewhat reduced compared to that of the as-fabricated and annealed samples.

The data presented in Fig. 7, *a* indicate that none of the studied samples exhibited statistically significant cytotoxic effects on MSCs. After 24 h of incubation, no

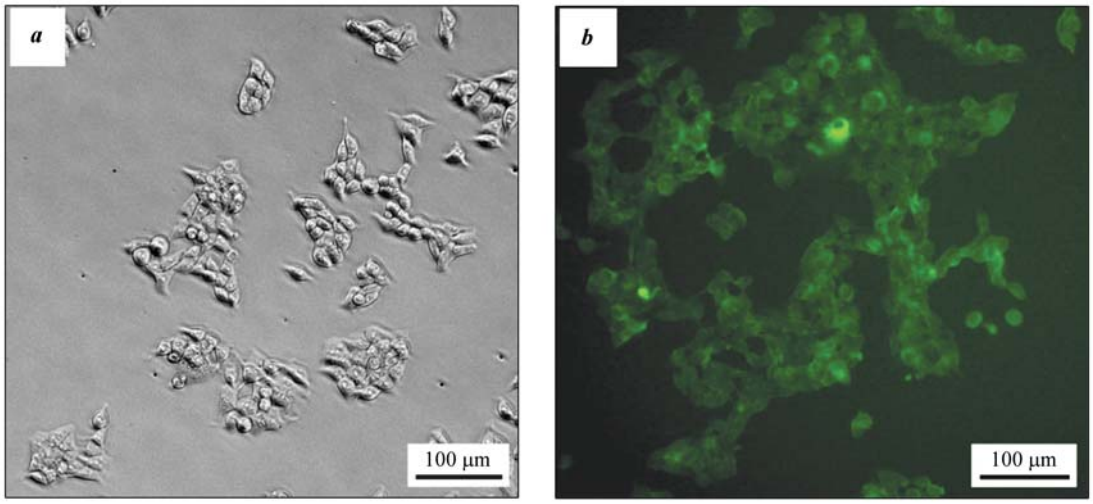

Fig. 5. Morphology, viability, and adhesion potential of MSCs (control) used as a cellular model for evaluating the adhesion properties of the studied alloys

a – phase contrast microscopy, unstained
b – fluorescence microscopy, with phase contrast Calcein AM cell staining

Рис. 5. Морфология, жизнеспособность и адгезионный потенциал ММСК (контроль), использованных в качестве клеточной модели для оценки адгезионных свойств изучаемых сплавов

a – фазово-контрастная микроскопия, без окраски
b – флуоресцентная микроскопия, дополненная использованием фазового контраста, окраска клеток «Calcein AM»

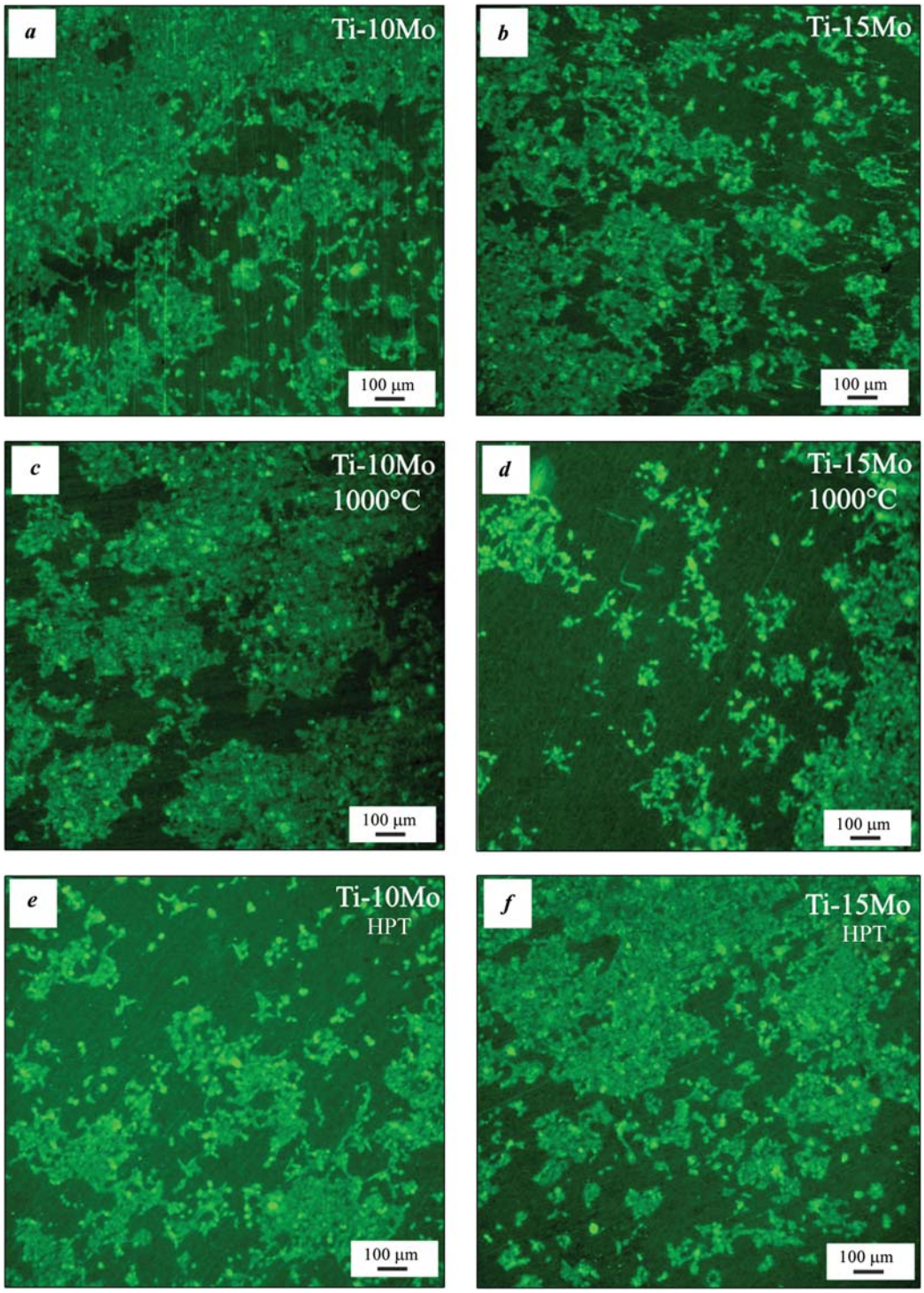

Fig. 6. Colonization and adhesion of MSCs on the surface of Ti–Mo alloy samples

Fluorescence microscopy, Calcein AM staining, green fluorescence
a, ***b*** – as-fabricated; ***c***, ***d*** – after annealing (1000 °C); ***e***, ***f*** – after HPT processing
a, ***c***, ***e*** – Ti–10 Mo alloy; ***b***, ***d***, ***f*** – Ti–15 Mo alloy

Рис. 6. Колонизация и адгезия ММСК на поверхности образцов сплавов на основе Ti–Mo

Флуоресцентная микроскопия. Окраска клеток – «Calcein AM» (зеленая флуоресценция)
a, ***b*** – в исходном состоянии; ***c***, ***d*** – после отжига (1000 °C), ***e***, ***f*** – после КВД-обработки
a, ***c***, ***e*** – сплав Ti–10Mo; ***b***, ***d***, ***f*** – сплав Ti–15Mo

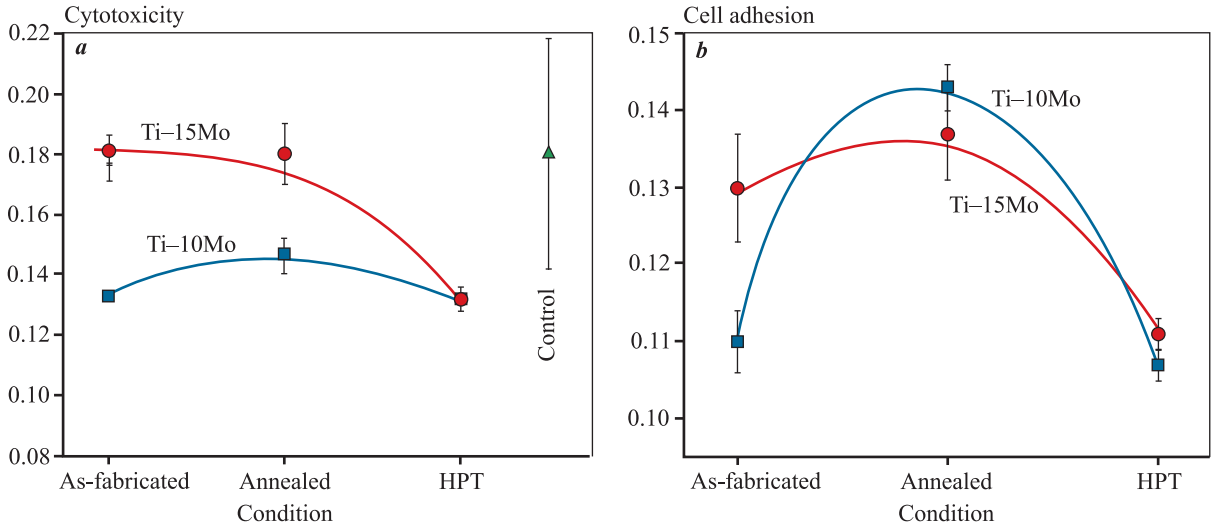

Fig. 7. Dependences of cytotoxicity (***a***) and cell adhesion (***b***) of Ti–10wt.%Mo and Ti–15wt.%Mo alloys on processing method

Рис. 7. Зависимости цитотоксичности (***a***) и клеточной адгезии (***b***) сплавов Ti–10Mo и Ti–15Mo от вида обработки

decrease in cell viability was observed compared to the control ($p > 0.05$), which meets the requirements for biocompatible materials intended for medical applications. However, HPT processing appeared to induce a slight trend toward reduced viability.

Quantitative assessment of cell activity on the alloy surfaces at the end of the observation period demonstrated that the highest activity was observed in annealed samples, while the lowest values corresponded to the HPT-processed samples.

Discussion of the results

Differences in fabrication methods and in the purity of the starting components affect not only the phase composition of the ingots, but also, consequently, the mechanical properties of the alloys. For example, in [5] a series of binary Ti—Mo alloys containing 6—20 wt. % Mo was studied. The ingots were produced by industrial arc melting, and the alloys were examined in the as-cast state without any additional processing. Two alloys — Ti—10wt.%Mo and Ti—15wt.%Mo — consisting solely of the β phase exhibited different mechanical properties. In particular, the bending strength and hardness of the alloy containing 10 wt. % Mo were higher than those of Ti—15wt.%Mo. However, when these data are compared with the results of the present study, differences in the phase composition of the same nominal alloys become apparent, which in turn lead to discrepancies in their mechanical properties.

In [6], Ti—10wt.% Mo and Ti—20wt.%Mo alloys were investigated, and the authors demonstrated that both the mechanical properties and the microstructure are strongly dependent on the processing method (in that case, cold rolling). They concluded that the Ti—Mo alloys under study are more suitable for biomedical applications than conventional metallic biomaterials, as they combine a low yield strength with good ductility, and highlighted Ti—10wt.%Mo as the most promising composition. Although a direct comparison between [6] and the present work is not feasible because of differences in processing and material characteristics, the results of [6] clearly support the view that the processing method has a decisive influence on both the phase composition and the properties of Ti—Mo alloys.

In [7], a series of binary Ti—Mo alloys with 15—18 wt. % Mo was examined. The Ti—17wt.% Mo alloy exhibited low elasticity, high tensile strength, and good ductility, making it a promising candidate for biomedical use.

The Ti—15.05wt.%Mo alloy developed by the group of authors in [8] also demonstrated good potential for orthopedic implant applications, with a hardness of 350 HV and an elastic modulus of 70 GPa.

It is also worth mentioning the study [9], in which nanoindentation was used to measure the hardness and Young's modulus of individual phases. For the

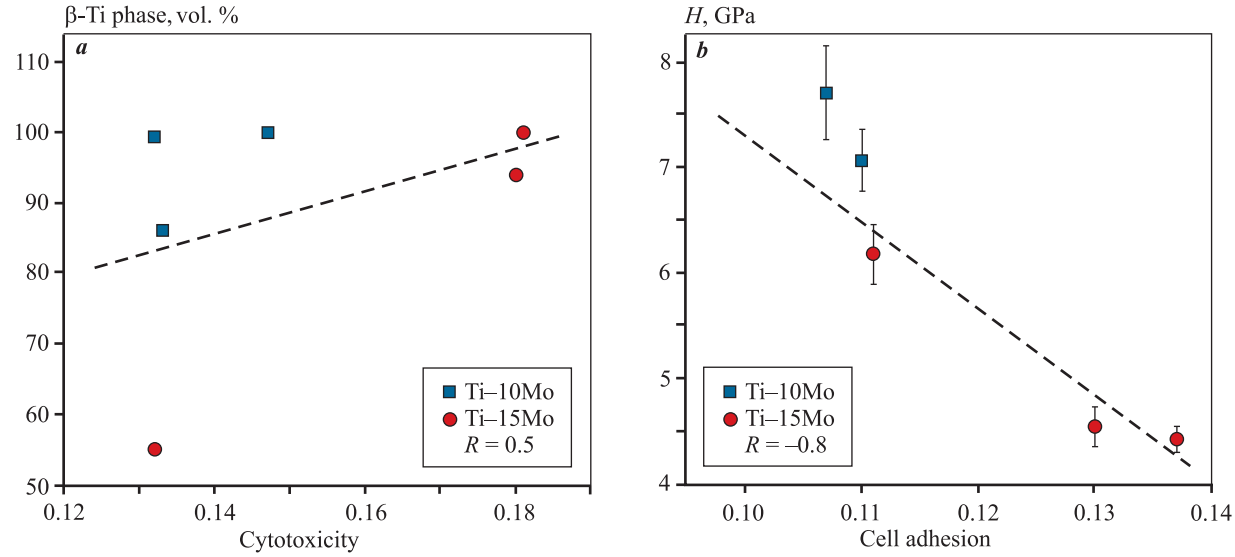

Fig. 8. Dependences of cytotoxicity (***a***) and cell adhesion (***b***) of Ti–10Mo and Ti–15Mo alloys on the volume fraction (***a***) of the β-Ti phase and hardness (***b***)

Рис. 8. Зависимости цитотоксичности (***a***) и клеточной адгезии (***b***) сплавов Ti–10Mo и Ti–15Mo от доли βTi-фазы (***a***) и твердости (***b***)

Ti—12Mo alloy, the difference in hardness between the α and β phases was approximately 35 % (3.96 and 5.97 GPa, respectively). The difference in Young's modulus between the two phases was about 20 % (114 GPa for the β phase and 141.7 GPa for the α phase). The alloys in [9] were produced by spark plasma sintering (SPS) from titanium and molybdenum powders.

Based on current evidence regarding the impact of fabrication and processing on material properties, we focused this study on two alloys, Ti—10wt.%Mo and Ti—15wt.%Mo, which exhibit mechanical characteristics suitable for biomedical use. The present work provides a comprehensive characterization of these alloys, including SEM and XRD analysis, nanoindentation, and biocompatibility assessment.

Evaluation of cell viability during incubation showed that all studied samples can be classified as biocompatible according to this parameter, although the annealed samples were found to be the safest for MSC viability. According to the results of cell adhesion testing, all Ti—Mo alloy samples stimulated MSC adhesion to their surfaces, with the annealed samples exhibiting the most pronounced activity. Considering the osteogenic potential of MSCs, it can be concluded that the Ti—10Mo and Ti—15Mo alloys, after heat treatment at 1000 °C, can be characterized as biocompatible materials with osteoconductive potential, i.e., capable of promoting bone tissue formation on their surface to accelerate implant osseointegration.

A possible correlation between cytotoxicity and cell adhesion and such material parameters as phase composition, hardness, and Young's modulus was analyzed. A positive correlation coefficient ($R = 0.5$) was obtained for the volume fraction of the β-Ti phase with both cytotoxicity (Fig. 8, *a*) and cell adhesion. Negative correlation coefficients (R) were found for hardness (Fig. 8, *b*) and Young's modulus.

Based on the correlation coefficient analysis, it can be proposed that the key factor determining the biocompatibility of Ti—Mo alloys is not their mechanical properties, but rather the phase composition and the type of processing applied to the material.

Conclusion

The experiments performed in this study demonstrated that all investigated Ti—Mo alloy samples can be classified as biocompatible, since, during *in vitro* incubation with non-transformed cells, they did not exert any statistically significant cytotoxic or hemolytic effects. In addition, all samples were found to stimulate surface colonization by cells with osteogenic potential, which suggests that, following intrabony implantation, they may undergo accelerated integration into bone tissue by promoting callus formation in the contact area.

It was shown that HPT processing of the materials reduces both cytotoxicity and cell adhesion parameters

for both Ti—Mo alloys. At the same time, higher levels of cell adhesion and cytotoxicity were recorded for the annealed Ti—Mo alloy samples.

The positive correlation coefficients calculated for cytotoxicity and cell adhesion as a function of the β-Ti phase fraction in both Ti—10wt.%Mo and Ti—15wt.%Mo alloys indicate the predominant influence of phase composition on the biocompatibility of the material.

References

1. Chen Q., Thouas G.A. Metallic implant biomaterials. *Materials Science and Engineering R*. 2015;(87):1—57. http://dx.doi.org/10.1016/j.mser.2014.10.001
2. Kolli R.P., Devaraj A. A review of metastable beta titanium alloys. *Metals*. 2018;8(7):506. http://dx.doi.org/10.3390/met8070506
3. Geetha M., Singh A.K., Asokamani R., Gogia A.K. Ti based biomaterials, the ultimate choice for orthopaedic implants — A review. *Progress in Materials Science*. 2009;54(3):397—425. http://dx.doi.org/10.1016/j.pmatsci.2008.06.004
4. Kaur M., Singh K. Review on titanium and titanium based alloys as biomaterials for orthopaedic applications. *Materials Science and Engineering: C*. 2019;102:844—862. https://doi.org/10.1016/j.msec.2019.04.064
5. Ho W.F., Ju C.P., Chern Lin J.H. Structure and properties of cast binary Ti—Mo alloys. *Biomaterials*. 1999;20(22):2115—2122. http://doi.org/10.1016/S0142-9612(99)00114-3
6. Zhou Y.-L., Luo D.-M. Microstructures and mechanical properties of Ti—Mo alloys cold-rolled and heat treated. *Materials Characterization*. 2011;62(10):931—937. http://doi.org/10.1016/j.matchar.2011.07.010
7. Zhao X., Niinomi M., Nakai M., Hieda J. Beta type Ti—Mo alloys with changeable Young's modulus for spinal fixation applications. *Acta Biomaterialia*. 2012;8(5):1990—1997. http://doi.org/10.1016/j.actbio.2012.02.004
8. Moshokoa N., Raganya L., Obadele B.A., Machaka R., Makhatha M.E. Microstructural and mechanical properties of Ti—Mo alloys designed by the cluster plus glue atom model for biomedical application. *The International Journal of Advanced Manufacturing Technology*. 2020;111:1237—1246. https://doi.org/10.1007/s00170-020-06208-7
9. Asl M.S., Delbari S.A., Azadbeh M., Namini A.S., Mehrabian M., Nguyen V.-H., Le Q.V., Shokouhimehr M., Mohammadi M. Nanoindentational and conventional mechanical properties of spark plasma sintered Ti—Mo alloys. *Journal of Materials Research and Technology*. 2020;9(5):10647—10658. https://doi.org/10.1016/j.jmrt.2020.07.066
10. Verestiuc L., Spataru M.-C., Baltatu M.S., Butnaru M., Solcan C., Sandu A.V., Voiculescu I., Geanta V., Vizureanu P. New Ti—Mo—Si materials for bone prosthesis applications. *Journal of the Mechanical Behavior of Biomedical Materials*. 2021;113:104198. https://doi.org/10.1016/j.jmbbm.2020.104198
11. Edalati K., Ahmed A.Q., Akrami S., Ameyama K., Aptukov V., Asfandiyarov R.N., Ashida M., Astanin V., Bachmaier A., Beloshenko V., Bobruk E.V., Bryła K., Cabrera J.M., Carvalho A.P., Chinh N.Q., Choi I.C., Chulist R., Cubero-Sesin J.M., Davdian G., Demirtas M., Zhu Y.T. Severe plastic deformation for producing superfunctional ultrafine-grained and heterostructured materials: An interdisciplinary review. *Journal of Alloys and Compounds*. 2024;1002:174667. https://doi.org/10.1016/j.jallcom.2024.174667
12. Edalati K., Matsubara E., Horita Z. Processing pure Ti by high-pressure torsion in wide ranges of pressures and strain. *Metallurgical and Materials Transactions A*. 2009;40:2079—2086. http://doi.org/10.1007/s11661-009-9890-5
13. Gornakova A.S., Korneva A., Tyurin A.I., Afonikova N.S., Kilmametov A.R., Straumal B.B. Omega phase formation and mechanical properties of Ti—1.5 wt.% Mo and Ti—15 wt.% Mo alloys after high-pressure torsion. *Processes*. 2023;11(1):221. https://doi.org/10.3390/pr11010221
14. Straumal B.B., Kilmametov A.R., Ivanisenko Yu., Mazilkin A.A., Valiev R.Z., Afonikova N.S., Gornakova A.S., Hahn H. Diffusive and displacive phase transitions in Ti—Fe and Ti—Co alloys under high pressure torsion. *Journal of Alloys and Compounds*. 2018;735:2281—2286. https://doi.org/10.1016/j.jallcom.2017.11.317
15. Valiev R.Z., Islamgaliev R.K., Alexandrov I.V. Bulk nanostructured materials from severe plastic deformation. *Progress in Materials Science*. 2000;45(2):103—189. https://doi.org/10.1016/S0079-6425(99)00007-9
16. Straumal B.B., Kogtenkova O.A., Gornakova A.S., Khorosheva M.A., Straumal P.B., Prokofiev P.A., Bradai D., Kilmametov A.R. Competition between the formation and decomposition of a solid solution in Al—Cu alloys under high-pressure torsion. *JETP Letters*. 2025;121:619—624. https://doi.org/10.1134/S0021364025605822

17. Zhilyaev A.P., Langdon T.G. Using high-pressure torsion for metal processing: Fundamentals and applications. *Progress in Materials Science*. 2008;53(6):893—979. https://doi.org/10.1016/j.pmatsci.2008.03.002
18. Gatina S.A. Phase transformations and mechanical properties of a pseudo-β-alloy Ti–15Mo subjected to intensive plastic deformation: Dis. Cand. Sci (Eng.). Ufa: Ufa State Aviation Technical Univercity, 2016. (In Russ.).
Гатина С.А. Фазовые превращения и механические свойства псевдо-β-сплава Ti–15Mo, подвергнутого интенсивной пластической деформации: Дис. ... канд. техн. наук. Уфа: Уфимский гос. авиационный технический университет, 2016.
19. Korneva A., Straumal B., Kilmametov A., Gondek Ł., Wierzbicka-Miernik A., Litynska-Dobrzynska L., Cios G., Chulist R., Zieba P. Thermal stability and microhardness of metastable ω-phase in the Ti—3.3at.%Co alloy subjected to high pressure torsion. *Journal of Alloys and Compounds*. 2020;834:155132. https://doi.org/10.1016/j.jallcom.2020.155132
20. Korneva A., Straumal B., Kilmametov A., Gornakova A., Wierzbicka-Miernik A., Lityńska-Dobrzyńska L., Chulist R., Gondek Ł., Cios G., Zięba P. Omega phase formation in Ti—3wt.%Nb alloy induced by high-pressure torsion. *Materials*. 2021;14(9):2262. https://doi.org/10.3390/ma14092262
21. Rogachev S.O., Nikulin S.A., Khatkevich V.M., Sundeev R.V., Komissarov A.A. Features of structure formation in layered metallic materials processed by high pressure torsion. *Metallurgical and Materials Transactions A*. 2020;51:1781—1788. https://doi.org/10.1007/s11661-020-05654-y
22. Anisimova N., Kiselevskiy M., Martynenko N., Straumal B., Willumeit-Römer R., Dobatkin S., Estrin Yu. Cytotoxicity of biodegradable magnesium alloy WE43 to tumor cells in vitro: Bioresorbable implants with antitumor activity. *Journal of Biomedical Materials Research. Part B: Applied Biomaterials*. 2020;108(1): 167—173. https://doi.org/10.1002/jbm.b.34375
23. Milanov N.O., Startseva O.I., Istranov A.L., Mel'nikov D.V., Zakharenko A.S. Prospects of clinical application of stem cells of adipose tissue in plastic surgery and regenerative medicine. *Pirogov Russian Journal of Surgery*. 2014;(4):70—76. (In Russ.). https://www.mediasphera.ru/issues/khirurgiya-zhurnal-im-n-i-pirogova/2014/4/downloads/ru/030023-12072014416
Миланов Н.О., Старцева О.И., Истранов А.Л., Мельников Д.В., Захаренко А.С. Перспективы клинического применения стволовых клеток жировой ткани в пластической хирургии и регенеративной медицине. *Хирургия. Журнал им. Н.И. Пирогова*. 2014;(4):70—76.

Information about the authors

Alena S. Gornakova – Cand. Sci. (Phys.-Math.), Senior Researcher, Institute of Solid State Physics of the Russian Academy of Sciences (ISSP RAS).
https://orcid.org/0000-0002-8035-0902
E-mail: alenahas@issp.ac.ru

Anna Korneva Surmacz – Dr. Sci. (Eng.), Associate Professor, Institute of Metallurgy and Materials Science of the Polish Academy of Sciences.
https://orcid.org/0000-0001-7902-0335
E-mail: a.korniewa@imim.pl

Keryam Mursali oglu Novruzov – Laboratory Assistant Researcher, Laboratory of Cellular Immunity, N.N. Blokhin National Medical Research Center of Oncology of the Ministry of Health of the Russia.
https://orcid.org/0000-0002-0773-255X
E-mail: nkeryam@gmail.com

Dmitry G. Shaisultanov – Cand. Sci. (Eng.), Head of the Laboratory, Department of Materials Science and Technology, Saint Petersburg Marine Technical University.
https://orcid.org/0000-0002-3914-7793
E-mail: shaysultanov@bsuedu.ru

Natalia S. Afonikova – Cand. Sci. (Phys.-Math.), Senior Researcher, ISSP RAS.
https://orcid.org/0009-0001-3073-262X
E-mail: natasha@issp.ac.ru

Boris B. Straumal – Dr. Sci. (Phys.-Math.), Head of the Laboratory, Leading Researcher, ISSP RAS.
https://orcid.org/0000-0001-5601-0660
E-mail: straumal@issp.ac.ru

Alexander I. Tyurin – Cand. Sci. (Phys.-Math.), Associate Professor, Senior Researcher, Scientific and Educational Center "Nanomaterials and Nanotechnologies" of the Tambov State University n.a. G.R. Derzhavin.
https://orcid.org/0000-0001-8020-2507
E-mail: tyurinalexander@yandex.ru

Vladimir A. Tyurin – Engineer, Scientific and Educational Center "Nanomaterials and Nanotechnologies" of the Tambov State University n.a. G.R. Derzhavin.
https://orcid.org/0009-0008-5481-4751
E-mail: va068@bk.ru

Grigorii S. Davdian – Postraduate Student of the National University of Science and Technology "MISIS", Junior Researcher of the ISSP RAS.
https://orcid.org/0000-0002-2529-0804
E-mail: faberest@yandex.ru

Информация об авторах

Алена Сергеевна Горнакова – к.ф.-м.н., ст. науч. сотрудник Института физики твердого тела (ИФТТ) РАН.
https://orcid.org/0000-0002-8035-0902
E-mail: alenahas@issp.ac.ru

Анна Корнева Сурмач – д.т.н., доцент Института металлургии и материаловедения Польской академии наук.
https://orcid.org/0000-0001-7902-0335
E-mail: a.korniewa@imim.pl

Керям Мурсали оглы Новрузов – лаборант-исследователь лаборатории клеточного иммунитета Национального медицинского исследовательского центра онкологии им. Н.Н. Блохина Минздрава России.
https://orcid.org/0000-0002-0773-255X
E-mail: nkeryam@gmail.com

Дмитрий Георгиевич Шайсултанов – к.т.н., заведующий лабораторией кафедры материаловедения и технологии материалов Санкт-Петербургского государственного морского технического университета.
https://orcid.org/0000-0002-3914-7793
E-mail: shaysultanov@bsuedu.ru

Наталья Сергеевна Афоникова – к.ф.-м.н., ст. науч. сотрудник ИФТТ РАН.
https://orcid.org/0009-0001-3073-262X
E-mail: natasha@issp.ac.ru

Борис Борисович Страумал – д.ф.-м.н., заведующий лабораторией, гл. науч. сотрудник ИФТТ РАН.
https://orcid.org/0000-0001-5601-0660
E-mail: straumal@issp.ac.ru

Александр Иванович Тюрин – к.ф.-м.н., доцент, ст. науч. сотрудник Научно-образовательного центра «Наноматериалы и нанотехнологии» Тамбовского государственного университета им. Г.Р. Державина (НОЦ «НМиНТ» ТГУ им. Г.Р. Державина).
https://orcid.org/0000-0001-8020-2507
E-mail: tyurinalexander@yandex.ru

Владимир Александрович Тюрин – инженер НОЦ «НМиНТ» ТГУ им. Г.Р. Державина.
https://orcid.org/0009-0008-5481-4751
E-mail: va068@bk.ru

Григорий Сергеевич Давдян – аспирант Национального исследовательского технологического университета «МИСИС»; мл. науч. сотрудник ИФТТ РАН.
https://orcid.org/0000-0002-2529-0804
E-mail: faberest@yandex.ru

Contribution of the authors

A.S. Gornakova – definition of the research objectives, overall supervision of the study, manuscript writing.

A. Korneva Surmacz – scanning electron microscopy (SEM) investigations, participation in data discussion, manuscript writing.

K.M. Novruzov – investigation of cell adhesion on titanium–molybdenum alloys, participation in data discussion.

D.G. Shaysultanov – fabrication of titanium–molybdenum alloy ingots.

N.S. Afonikova – *X*-ray diffraction and phase analyses.

B.B. Straumal – high-pressure torsion processing, discussion of experimental results.

A.I. Tyurin – nanoindentation testing, processing and discussion of experimental data.

V.A. Tyurin – nanoindentation of titanium–molybdenum alloy samples.

G.S. Davdian – microhardness measurements and data processing.

Вклад авторов

А.С. Горнакова – определение цели работы, общее курирование работы, написание статьи.

А. Корнева Сурмач – исследования на сканирующем электронном микроскопе, участие в обсуждении результатов, написание статьи.

К.М. Новрузов – исследование клеточной адгезии сплавов титан–молибден, участие в обсуждении результатов.

Д.Г. Шайсултанов – изготовление слитков титан–молибден.

Н.С. Афоникова – рентгеноструктурный и фазовый анализы.

Б.Б. Страумал – кручение под высоким давлением, обсуждение экспериментальных результатов.

А.И. Тюрин – наноиндентирование, обработка экспериментальных результатов, обсуждение экспериментальных результатов.

В.А. Тюрин – наноидентирование образцов титан–молибден.

Г.С. Давдян – измерения микротвердости, расчеты полученных данных.

The article was submitted 30.05.2025, revised 20.08.2025, accepted for publication 28.08.2025

Статья поступила в редакцию 30.05.2025, доработана 20.08.2025, подписана в печать 28.08.2025